



NKS-411
ISBN 978-87-7893-500-7

Phenomena Threatening Containment
Integrity in Deterministic and
Probabilistic analyses and
integration of PRA
levels 1 and 2

Anna Nieminen¹ (ed.)
Veikko Taivassalo¹
Magnus Strandberg¹
Tero Tyrväinen¹
Ilkka Karanta¹

¹VTT Technical Research Centre of Finland Ltd

October 2018

Abstract

Phenomena threatening the BWR containment integrity were assessed both deterministically and probabilistically. Studies related to establishing a temperature-based dryout criteria for a debris bed were continued evaluating the influence of friction models. Agreement between the VTT and KTH results was improved after implementing the same friction model as in DECOSIM into Fluent. Deterministic steam explosion analysis was performed to study the effect of RPV breaking location on dynamic pressure load on lower drywell wall. The resulting explosions were stronger in comparison to the previous central break cases.

Probabilistic modelling of steam explosions is very challenging because uncertainties related to the phenomenon, especially triggering of explosions, are very high. Currently, it is a good idea to use conservative probabilities in PRA. It could be studied if explosion triggering probabilities could be estimated based on some physical parameters calculated by deterministic software tools, but plenty of development work and analyses are needed before well-justified probabilities can be estimated.

The development of simplified PRA models of a BWR plant was also continued by extending previously developed level 1 and level 2 models were extended and integrated so that it is possible to list most important event tree sequences, initiating events and basic events with regard to radioactive releases.

Key words

Debris bed coolability, Fluent, steam explosions, MC3D, PRA

Phenomena Threatening Containment Integrity in Deterministic and Probabilistic Analyses and Integration of PRA Levels 1 and 2

NKS-R SPARC

(Contract: AFT/NKS-R(17)122/10)

Anna Nieminen¹ (ed.), Veikko Taivassalo¹, Magnus Strandberg¹, Tero Tyrväinen¹, Ilkka Karanta¹

¹VTT Technical Research Centre of Finland Ltd

Table of contents

	Page
1. Introduction	3
2. Particle debris coolability	3
3. Steam explosions in a Nordic BWR plant	4
3.1 Deterministic analyses	4
3.2. Probabilistic approach	5
4. Integration of PRA levels 1 and 2	6
5. Conclusions	6
Acknowledgement	7
Disclaimer	7
References	7

1. Introduction

Ensuring the integrity of the containment during a hypothetical severe accident is extremely important since the containment is the last safety barrier preventing radioactive release to the environment. To assess phenomena threatening the Nordic Boiling Water Reactor (BWR) containment integrity more reliably, long-term debris bed coolability and steam explosions were analysed, and level 2 probabilistic risk assessment (PRA) modelling was studied.

This report is a summary of the three reports included as annexes.

2. Particle debris coolability

Achieving long-term coolability of molten corium is the main objective in the unlikely event of a severe nuclear reactor accident. The Nordic BWRs rely on cooling the corium in the flooded lower drywell of the containment as a cornerstone of the severe accident management strategy. During the discharge of the corium in the deep water pool, the molten material is fragmented into droplets and subsequently solidified into particles, which settle on the floor of the containment, forming a porous debris bed.

The coolability limit for the debris bed is traditionally based on the minimum dryout heat flux. This approach might be overly conservative, since the temperature may remain on an acceptable level even in the dry zone. Instead of the dryout heat flux, it has been proposed that the coolability limit should be based on the increase of the particle temperature (Atkhen & Berthoud, 2006). To analyse this, the behaviour of conical debris beds was previously studied by performing MEWA simulations (Taivassalo & Takasuo, 2017) and comparing to the DECOSIM results by Yakush & Kudinov (2014). The simulation results of the MEWA code were not in fully agreement with the DECOSIM results.

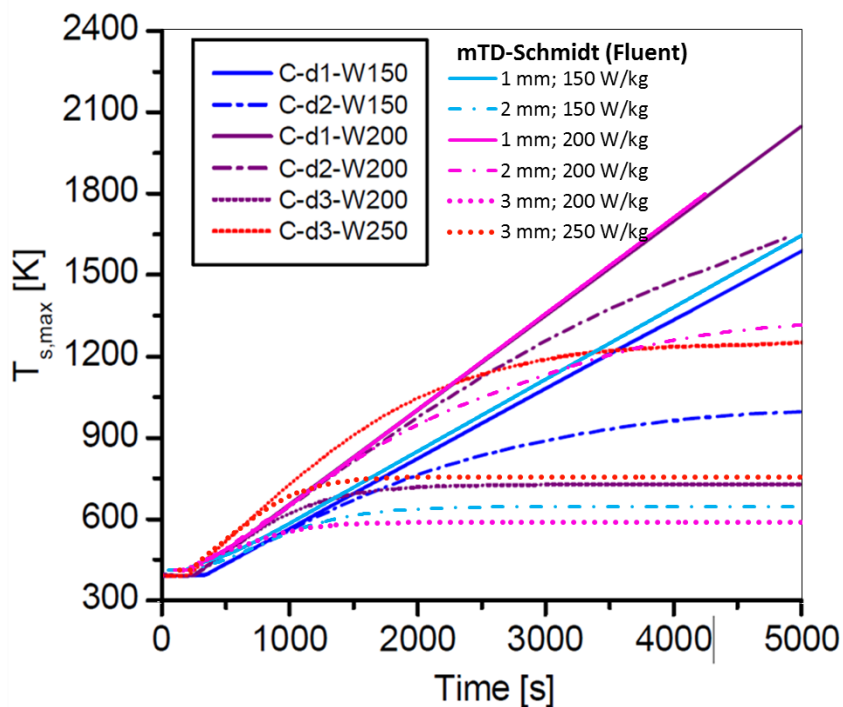


Figure 1. Comparison of the time evolution of the maximum solid particle temperature in the Fluent simulations of this study and in the DECOSIM simulations.

The effect of heat transfer models available in MEWA did not explain the differences compared to the KTH's DECOSIM results and therefore the influence of the friction model in post-dryout conditions was analysed (ANNEX 1). As MEWA does not feature the same friction model as used in DECOSIM, it was added into the Fluent implementation of the debris bed coolability models. The usage of the same friction model improved the agreement. The comparison is in Figure 1. However, the convection and viscous term in the full multiphase flow equations solved by Fluent modify the flow field especially close to the tip of the conical bed hampering quantitative comparisons with the MEWA and DECOSIM results. On the other hand, in case of a conical debris bed, the simplified momentum equations might not predict flows satisfactory enough to be used in quantifying the temperature-based coolability limit.

3. Steam explosions in a Nordic BWR plant

As mentioned previously, the Nordic BWRs rely on cooling the corium in the flooded lower drywell. However, this severe accident management strategy for ensuring the melt coolability ex-vessel possesses a threat for steam explosions. When melt is fragmented to water, it causes a rapid transfer of thermal energy. This leads to a major pressure increase and in certain conditions this may lead to a steam explosion that could lead to early containment failure. Based on current research, it cannot be confirmed in which conditions the explosion is triggered.

3.1 Deterministic analyses

The steam explosion loads in a Nordic BWR containment were previously assessed with the MC3D code studying the sensitivity of the results for some key input parameters (Strandberg, 2016). The results showed that as long as the mixture is triggerable the strength of the resulting explosion does not change notably. The melt drop size that depends on the physical properties of the melt had the strongest effect on the explosion strength. Surprisingly, the melt temperature did not affect the explosion strength.

The effect of Reactor Pressure Vessel (RPV) breaking location on dynamic pressure load on lower drywell wall induced by a steam explosion was also analysed with MC3D (ANNEX 2). Premixing phase of the side-break analyses is illustrated in Figure 2. During the analysis of the results, it became clear that the 3D simulations suffer from stability issues in the explosion part, which caused the simulations to stop before the defined end time. This in turn makes analysing the pressure peaks at the wall difficult as it becomes uncertain if the maximum is reached before the calculations end. However, the resulting explosions were stronger in comparison to the previous 2D central break cases. It should be noticed that these analyses are not fully comparable, due to different nodalisation scheme.

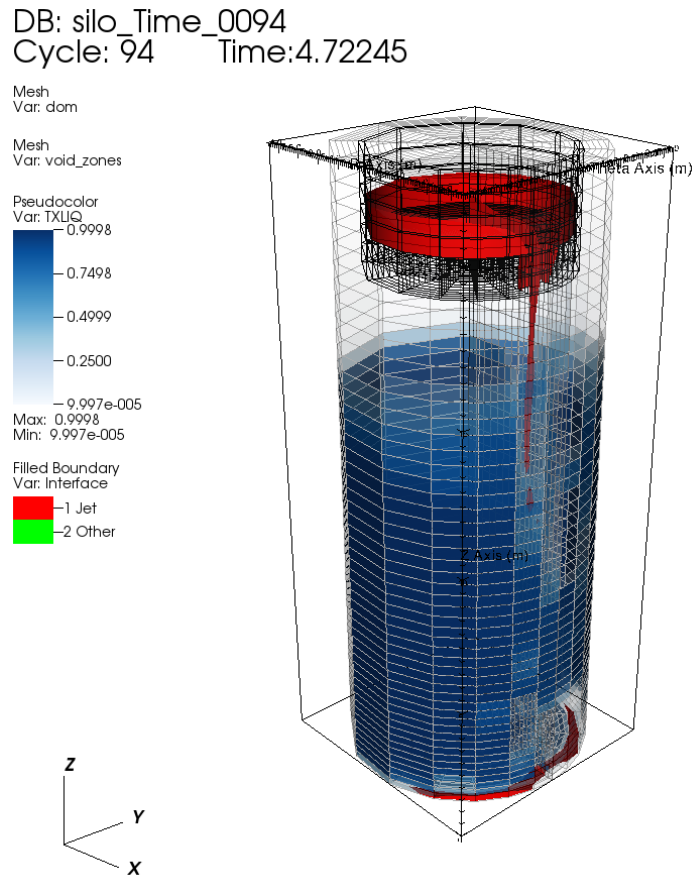


Figure 2. Visualization of the premixing phase when analysing a non-central break case.

3.2 Probabilistic approach

Probabilistic modelling of an ex-vessel steam explosion requires the estimation of the probability that an explosion occurs and the probability that the explosion breaks the containment if it occurs. In previous analyses (Silvonon, 2013) was conservatively assumed that steam explosion is triggered with certainty in high pressure, and with probability of 0.5 in low pressure. An uncertainty distribution was given for the pressure impulse of the explosion. The distribution was varied depending on the pressure (high or low) and on how much core melt was ejected to the lower drywell. The distributions are presented in Figure 3. Uncertainty distribution was also given for the lower drywell strength. The probability of containment failure was calculated based on the distribution of the pressure impulse and the lower drywell strength in each scenario using the load vs. strength approach.

Possibilities to improve probabilistic modelling of steam explosions were analysed in (ANNEX 3). Based on the previous steam explosion studies, it is evident that there is room for improvement. Concerning probabilistic modelling, uncertainties are high for most of the parameters involved. The explosion triggering probabilities are the most questionable parameters in the previous studies. It seems that triggering probabilities cannot be estimated realistically currently because deterministic computer codes are not reliable enough, sensitivity of triggering to parameter changes is great, and uncertainties related to the triggering phenomena are high. Plenty of development work and analyses are needed before well-justified probabilities can be estimated. Currently, it is better to use conservative values in the PRA models.

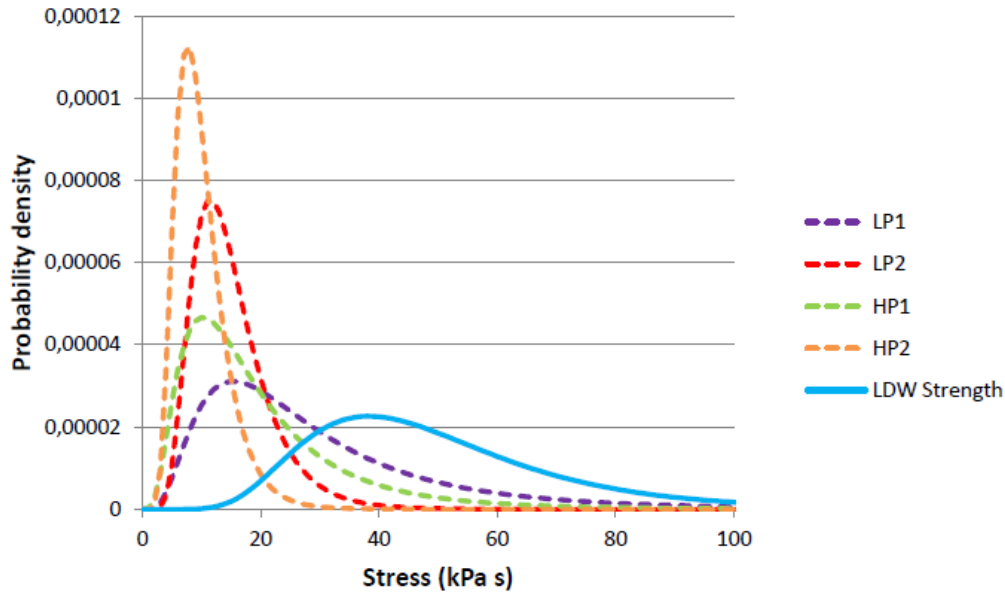


Figure 3. Distributions used to determine whether lower drywell fails due to pressure impulse caused by and ex-vessel steam explosion. (LP = low pressure, HP = high pressure, 1 = large amount of released corium, 2 = small amount of released corium and LDW = lower drywell).

4. Integration of PRA levels 1 and 2

PRA level 2 modelling was also studied in the context of the integration of PRA levels 1 and 2 (ANNEX 3). Previously developed simplified level 1 (Authen et al, 2015) and level 2 (Tyrväinen & Karanta, 2017) models were integrated and extended. The new model contains four level 1 event trees and five level 2 containment event trees (CETs). The level 2 part of the model has been developed using dynamic CETs of FinPSA. A dynamic CET is a simulation model that combines event tree modelling with parametric programming-based modelling. Levels 1 and 2 were integrated so that it is possible to list the contributions of individual event tree sequences, initiating events and basic events with regard to radioactive releases, for example to identify the most important contributors.

A special focus in the study was on the computation of an emergency core cooling system (ECCS) recovery probability based on level 1 results. Component failures causing the unavailability of the ECCS were divided into groups with presumably similar repair times, and Fussell-Vesely importance values were calculated for these groups based on minimal cut sets using a function provided by the programming language of FinPSA level 2; in this way, the computation was automated completely. The total ECCS recovery probability was calculated based on the Fussell-Vesely values and the ECCS recovery probabilities of the component failure groups in each plant damage state (PDS). The resulting recovery probabilities varied significantly between PDSs. However, the main purpose of the study was to demonstrate advanced features in the integration of PRA levels 1 and 2, not to produce realistic results.

5. Conclusions

When comparing VTT's MEWA results on the debris bed post-dryout temperature to KTH's DECOSIM results, a good agreement was achieved while the temperatures continued to increase, but the stabilized temperatures differed notably. The effect of heat transfer models available in MEWA did not explain the differences and therefore the influence of the friction

model in post-dryout conditions was analysed. After implementing the same friction model as used in DECOSIM into Fluent, agreement of the results was improved.

Deterministic steam explosion analysis was performed to study the effect of RPV breaking location on dynamic pressure load on lower drywell wall. Despite the simulations suffered from stability issues, it was found out that the resulting explosions were stronger in comparison to the previous central break cases.

Probabilistic modelling of steam explosions is very challenging because uncertainties related to the phenomenon, especially triggering of explosions, are very high. Pressure impulses of explosions can be calculated quite well using deterministic software tools, but the probability that an explosion occurs in the first place cannot be properly estimated based on current knowledge. Currently, it is a good idea to use conservative probabilities in PRA. It could be studied if explosion triggering probabilities could be estimated based on some physical parameters calculated by deterministic software tools or on the results of suitably designed experiments, but plenty of development work and analyses are needed before well-justified probabilities can be estimated.

The development of simplified PRA models of a BWR plant was also continued. Previously developed level 1 and level 2 models were extended and integrated so that it is possible to list most important event tree sequences, initiating events and basic events with regard to radioactive releases. A special focus was on the computation of emergency core cooling system recovery probability based on level 1 results.

Acknowledgement

This work has been partly funded by the Finnish Nuclear Power Plant Safety Research Programme SAFIR2018.

NKS conveys its gratitude to all organizations and persons who by means of financial support or contributions in kind have made the work presented in this report possible.

Disclaimer

The views expressed in this document remain the responsibility of the author(s) and do not necessarily reflect those of NKS. In particular, neither NKS nor any other organization or body supporting NKS activities can be held responsible for the material presented in this report.

References

Atkhen, K. & Berthoud, G., 2006. SILFIDE experiment: Coolability in a volumetrically heated debris bed. *Nuclear Engineering and Design*, 236, pp. 2126–2134.

Authen, S., Holmberg, J-E., Tyrväinen, T. & Zamani, L. 2015. Guidelines for reliability analysis of digital systems in PSA context – Final Report. Nordic nuclear safety research, NKS-330. 63 p + app. 37 p.

Silvonen, T. 2013. Steam explosion case study using IDPSA methodology. VTT Research Report VTT-R-05974-13. 33 p. + app. 19 p.

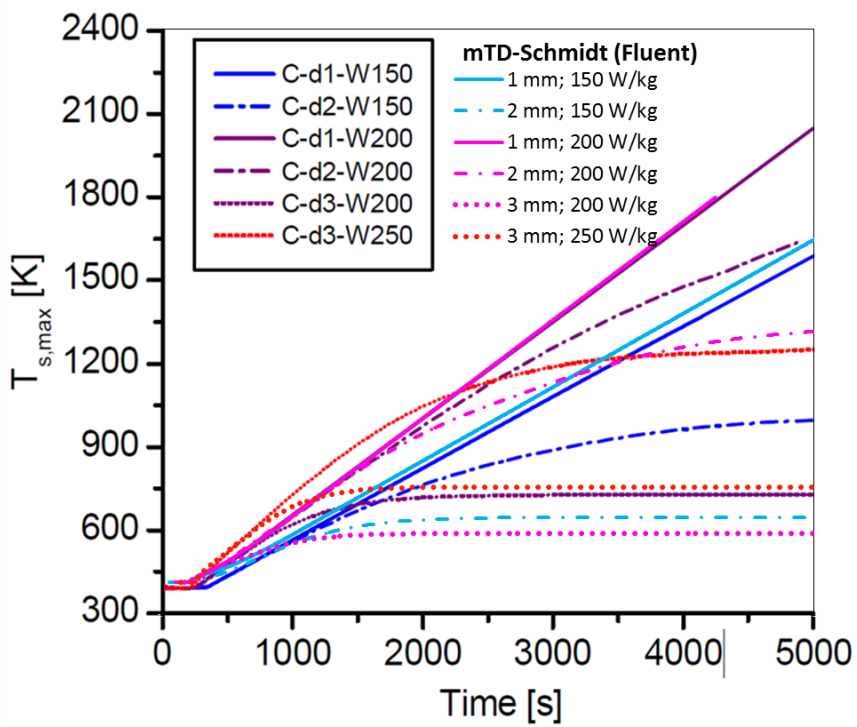
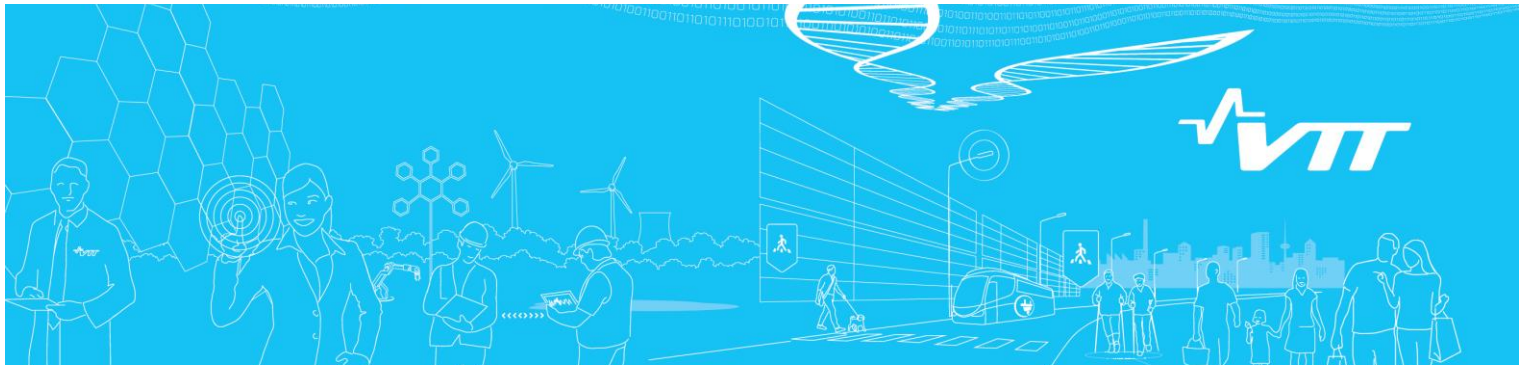
Strandberg, Magnus. Ex-Vessel Steam Explosion Analysis with MC3D. Master's Thesis. 68 p. + app. 15 p.

Taivassalo, V. & Takasuo, E. 2017. Predicting debris bed behaviour in post-dryout conditions VTT Research Report VTT-R-00762-17. 28 p.

Tyrväinen, T. & Karanta, I. 2017. Level 2 PRA studies - Source term characteristics and hydrogen explosions. VTT Research Report VTT-R-00354-17. 19 p. + app. 2 p.

Yakush, S. & Kudinov, P., 2014. A model for prediction of maximum post-dryout temperature in decay-heated debris bed. In 22nd International Conference on Nuclear Engineering. July 7-11, 2014, Prague, Czech Republic.

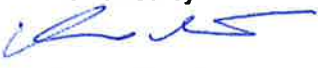
ANNEX 1
**Comparison of friction models for debris beds in
post-dryout conditions**



Comparison of friction models for debris beds in post-dryout conditions

Author: Veikko Taivassalo

Confidentiality: Public

Report's title	
Comparison of friction models for debris beds in post-dryout conditions	
Customer, contact person, address	Order reference
SAFIR2018 Research Programme on Nuclear Power Plant Safety 2015 – 2018	SAFIR 6/2017
Project name	Project number/Short name
Comprehensive Analysis of Severe Accidents	113414/CASA
Author(s)	Pages
Veikko Taivassalo	63/-
Keywords	Report identification code
debris bed, coolability, post-dryout conditions	VTT-R-01003-18
Summary	
<p>Achieving long-term coolability of molten corium is the main objective in the unlikely event of a severe nuclear reactor accident. The Nordic boiling water reactors (BWRs) rely on cooling the corium in the flooded lower drywell. During the discharge of the corium in the flooded drywell, the molten material is fragmented into droplets and subsequently solidified into particles, which settle on the floor of the containment, forming a porous debris bed. The coolability limit based on the minimum dryout heat flux might be overly conservative, since the temperature may remain on an acceptable level even in the dry zone. It has been proposed that the coolability limit should be based on an increase in the particle temperature. Previously (Taivassalo & Takasuo, 2017), the behaviour of two hypothetical conical debris beds was studied by performing MEWA simulations. Especially post-dryout conditions were analysed for a reference reactor debris bed and for conical debris beds studied by Yakush & Kudinov (2014). Different heat transfer models available in MEWA and important in predicting the post-dryout temperature field were tested. As the MEWA results clearly differ from the DECOSIM results of Yakush & Kudinov (2014) in cases that could be considered coolable based on temperature stabilization, the origin of the differences needs to be identified before trying to quantify the temperature-based criterion for coolability of a debris bed.</p> <p>This work concentrates on the influence of the friction model in post-dryout conditions. The MEWA results show that computed bed behaviour can differ for different friction models. As MEWA does not feature the same friction model used in DECOSIM, it was added into the Fluent impelentation (Taksuo et al., 2015) of the debris bed coolability models. After verifying the Fluent impelentation in post-dryout conditions, simulations for the conical beds of Yakush & Kudinov were performed with Fluent. The usage of the same friction model improved the agreement. However, the convection and viscous term in the full multiphase flow equations solved by Fluent modify the flow field especially close to the tip of the conical bed hampering quantitative comparisons with the MEWA and DECOSIM results. On the other hand, in case of a conical debris bed, the simplified momentum equations might not predict flows satisfactory enough to be used in quantifying the temperature-based criterion for coolability.</p>	
Confidentiality	Public
Espoo 25.2.2018	
Written by	Reviewed by
	
Veikko Taivassalo Principal Scientist	Anna Nieminen Research Scientist
Accepted by	
	
Anitta Hämäläinen Research Team Leader	
VTT's contact address	
PO Box 1000, 02044-VTT, Finland	
Distribution (customer and VTT)	
SAFIR2018 Reference Group 2	
<p><i>The use of the name of VTT Technical Research Centre of Finland Ltd in advertising or publishing of a part of this report is only permissible with written authorisation from VTT Technical Research Centre of Finland Ltd.</i></p>	

Contents

Contents.....	2
1. Introduction.....	3
2. Conical particle beds of Yakush & Kudinov.....	5
2.1 Case specifications.....	5
2.2 DECOSIM simulations of Yakush & Kudinov.....	5
2.3 DECOSIM results of Yakush & Kudinov.....	6
3. MEWA simulations.....	9
3.1 Background.....	9
3.2 On the features of the MEWA code.....	9
3.2.1 Conservation equations.....	9
3.2.2 Closure models.....	10
3.3 Computational cases.....	18
3.4 Results.....	20
3.5 Comparison of the MEWA and DECOSIM results.....	27
3.6 Discussion.....	32
4. CFD-based analyses.....	33
4.1 Background.....	33
4.2 CFD-based analysis framework.....	33
4.2.1 Conversation equations.....	33
4.2.2 Schmidt friction model.....	34
4.3 Verification of the Fluent implementation.....	35
4.3.1 Computational cases.....	35
4.3.2 Comparison of the CFD and MEWA results.....	36
4.3.3 Influence of computational parameters.....	45
4.3.4 Discussion.....	47
4.4 Application of the Schmidt model.....	49
4.4.1 Computational cases.....	49
4.4.2 Results.....	50
4.4.3 Comparison of the CFD and DECOSIM results.....	57
4.4.4 Discussion.....	59
5. Conclusion.....	60
References.....	62

1. Introduction

Achieving long-term coolability of molten corium is the main objective in the unlikely event of a severe nuclear reactor accident. The Nordic boiling water reactors (BWRs) rely on cooling the corium in the flooded lower drywell of the containment as a cornerstone of the severe accident management strategy. During the discharge of the corium in the deep water pool (~10 m), the molten material is fragmented into droplets and subsequently solidified into particles, which settle on the floor of the containment, forming a porous debris bed.

The coolability of heap-shaped (conical) and flat-shaped, top-flooded (cylindrical) debris beds was studied in the COOLOCE experiments, in which the dryout power and heat flux were measured (Takasuo, 2016). In the impressive amount of research on the dryout heat flux and debris bed coolability conducted in recent decades, studies on heat transfer after dryout has occurred are almost impossible to find. In the post-dryout conditions, the heating power required for dryout and a local loss of water has been reached and, more often than not, exceeded.

For debris beds of realistic shapes (heaps and cones), the post-dryout conditions are of interest since the particle temperature may stabilize even though a local dry zone has been formed (Atkhen & Berthoud, 2006). The coolability limit based on the minimum dryout heat flux might be overly conservative, since the temperature may remain on an acceptable level even in the dry zone. Instead of the dryout heat flux, it has been proposed that the coolability / non-coolability limit should be based on the increase of the particle temperature (Takasuo, 2015; Yakush & Kudinov, 2014). It should be noted that in the case of a top-flooded bed, local dryout usually leads to a temperature increase above the corium melting temperature and thus the post-dryout coolability is mainly of interest with the heap-shaped debris beds.

Previously (Taivassalo & Takasuo, 2017), the behaviour of two hypothetical conical debris beds was studied by performing MEWA (Bürger et al., 2006; Rahman, 2013) simulations. Coolability and especially conditions after dryout were analysed for the reference reactor debris bed and for conical debris beds studied at KTH by Yakush & Kudinov (2014). For each particle size, 1, 2, and 3 mm, several specific heating powers were used to cover conditions from no-dryout to (or close to) the corium remelting temperature. The MEWA results showed that the temperature-based coolability criterion increases the coolability limit compared to the void-based criterion (the dryout heat flux). In the dryout conditions, after the bed temperature stabilization, i.e., after achieving a steady-state, the bed temperature might locally be considerably higher than the saturation temperature. For 1 mm bed particles, the temperature-based criterion for the coolability of a debris bed would roughly double the coolability limit relative to the dryout-heat-flux-based criterion. The increase in the coolability limit would be larger for larger particles, but a small particle bed is considered more representative for realistic beds of random irregular particles (Chikhi et al., 2014).

However, the simulation results of the MEWA code were not in a full agreement with the DECOSIM results reported by Yakush & Kudinov (2014) (Taivassalo & Takasuo, 2017). In the 1 mm particle cases without temperature stabilization, the codes agree satisfactorily. On the other hand, these cases are not interesting because the maximum particle temperature eventually exceeds the temperatures where zirconium oxidation or even corium remelting begins. In the other conical bed cases studied by Yakush & Kudinov (2014), both the codes predict that the beds are coolable but MEWA and DECOSIM predict different transient behaviours and final steady-state conditions. Accordingly, before trying to quantify the temperature-based coolability criterion, the origin of the significant differences between the MEWA and DECOSIM results need to be identified.

In the previous study (Taivassalo & Takasuo, 2017), the influences of the bed particle size, heating power and porosity were also examined. Different heat transfer models available in MEWA and important in predicting the post-dryout temperature field were tested. Alternative

models for solid-to-gas heat transfer coefficient and for the effective dry-bed thermal conductivity did not change the results meaningfully.

In this work, analysing the origin of the differences in the DECOSIM and MEWA results is continued. The influence of the friction model is studied in the conical beds examined by Yakush & Kudinov (2014). The studied conical beds are introduced in Section 2. Most of the friction models as well as the heat transfer models available in MEWA are introduced in Section 3 with computational results and a comparison with the DECOSIM results of Yakush & Kudinov (2014). Since MEWA does not feature the friction model used in the DECOSIM simulations, it was added in the CFD-based implementation of the debris bed coolability models. Section 4 discusses on the verification of the CFD-code implementation in the post-dryout conditions and on the CFD-code based simulations of the conical beds of Yakush & Kudinov (2014).

2. Conical particle beds of Yakush & Kudinov

2.1 Case specifications

Yakush & Kudinov (2014) studied computationally conical and truncated-cone debris beds. In addition to the bed shape, the other properties of debris beds were also idealised assuming a homogenous porous medium formed by homogenous round particles of one size with constant physical properties and heat production.

This work considers the conical beds of Yakush & Kudinov (2014) and they are characterised in Table 1. The bed geometry is the same in all cases but the diameter of the bed particles is 1, 2 or 3 mm. The heating power varies and powers used for different particle sizes are given in Table 2.

Table 1. Characteristics of the conical debris beds studied at KTH (Yakush & Kudinov,2014).

Height of the debris bed (m)	3
Diameter of the debris bed (m)	6
Diameter of the water pool (m)	9
Height of the water pool (m)	6
Pressure at the top boundary (bar)	3
Porosity of the debris bed (-)	0.4
Diameter of the bed particles (mm)	1, 2, or 3
Density of corium (kg/m^3)	8285
Specific heat capacity of corium (J/kgK)	566
Thermal conductivity of corium (W/Km)	1.9

2.2 DECOSIM simulations of Yakush & Kudinov

The computational domain and mesh used in the DECOSIM simulations of Yakush & Kudinov (2014) are shown in Figure 1. The domain and mesh are axisymmetric respect to the vertical axis of the bed. The mesh consists of 30 x 51 cells. The white line in Figure 1 represents the ideal, conical surface of the bed. It is however unclear which cells around the white line are considered to be inside the bed.

The features of the DECOSIM code are introduced by Yakush & Kudinov (2014). In large, it is similar to the MEWA code discussed in Section 3.2.

Table 2. Conical debris bed cases studied at KTH (Yakush & Kudinov,2014). The computed cases are indicated by the maximum solid temperature.

Specific power (W/kg)	Maximum particle temperature (K)		
	Particle diameter (mm)		
	1	2	3
150	1587*	1008	
200	1699*,**	1837*,***	729
250			1250

* No dryout. Values given for the time of 5000 s.

** Probably given for the time of 4000 s (cf., Figure 3). The correct value is about 2050 K (cf., Figure 2).

*** Probably a typing error in the table of Yakush & Kudinov (2014). The correct value is about 1650 K, cf., Figure 2).

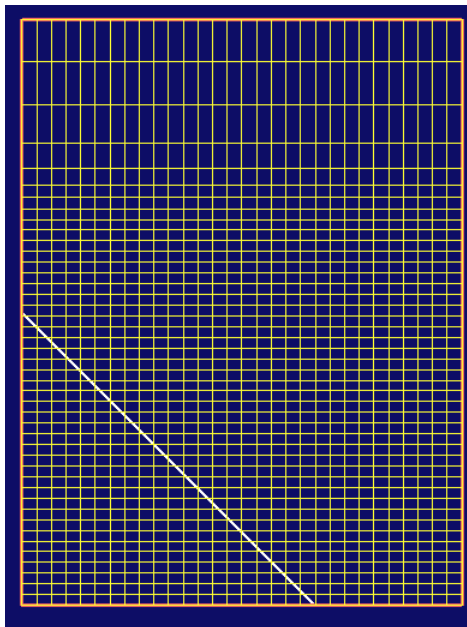


Figure 1. Computational domain, mesh and bed shape (the white line) for the conical debris beds in the study of Yakush & Kudinov (2014).

2.3 DECOSIM results of Yakush & Kudinov

Yakush & Kudinov (2014) report the results of the DECOSIM simulations for the conical debris beds. Some of the results needed in the comparison studies are introduced in following.

Figure 2, Figure 3 and Table 2 summarize the main results of the DECOSIM simulations for the conical debris bed cases defined in Section 2.1 (Yakush & Kudinov, 2014). The maximum particle temperature as a function of time is presented in Figure 2. In the 1 mm particle cases, the maximum particle temperature increases without stabilization as a function of time with an almost constant rate. In the cases of the 3 mm particles, the maximum particle temperature stabilizes or almost stabilizes to heating-power dependent values at least in 5000 s. In the beds of the 2 mm particles, the maximum particle temperature increases first almost with the same rate as in the 1 mm particle cases with the same heating power but later on the temperature increase rate decreases and the steady-state conditions would likely been reached if the simulations had continued further.

Figure 3 shows distributions of the void fraction and temperature of the solid bed particles at the time of 4000 s in the cases of the specific power equal to 200 W/kg (Yakush & Kudinov, 2014). In the 1 and 2 mm particle cases, steady states has not been reached (c.f., Figure 2). The results for the 3 mm particles in Figure 3 are steady-state results but the dry area is very small.

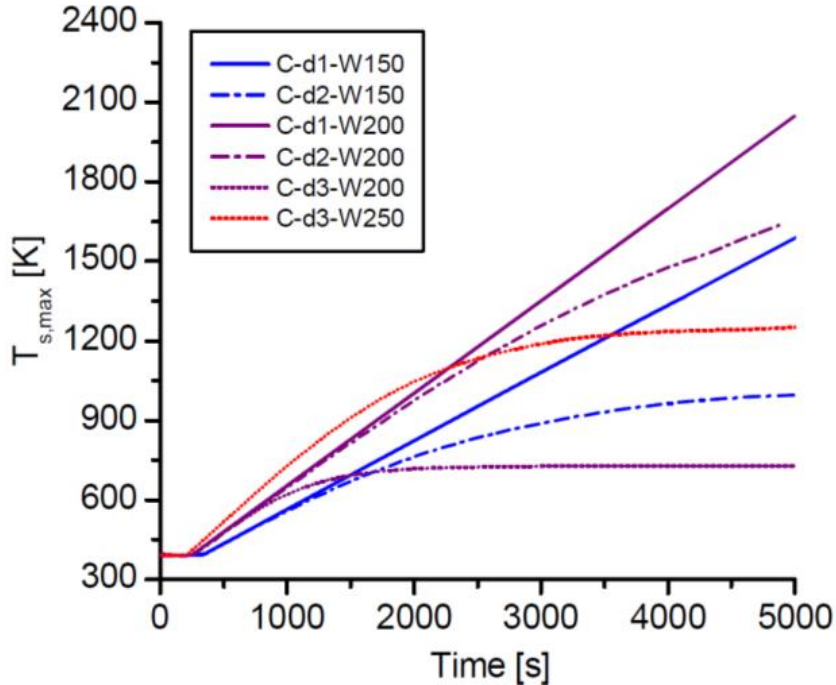


Figure 2. Maximum solid particle temperature as a function of time in the DECOSIM simulations for conical beds (Yakush & Kudinov, 2014). In the legend, the particle diameter in mm is given by the number after “d” and the specific heating power in W/kg by the number after “W”.

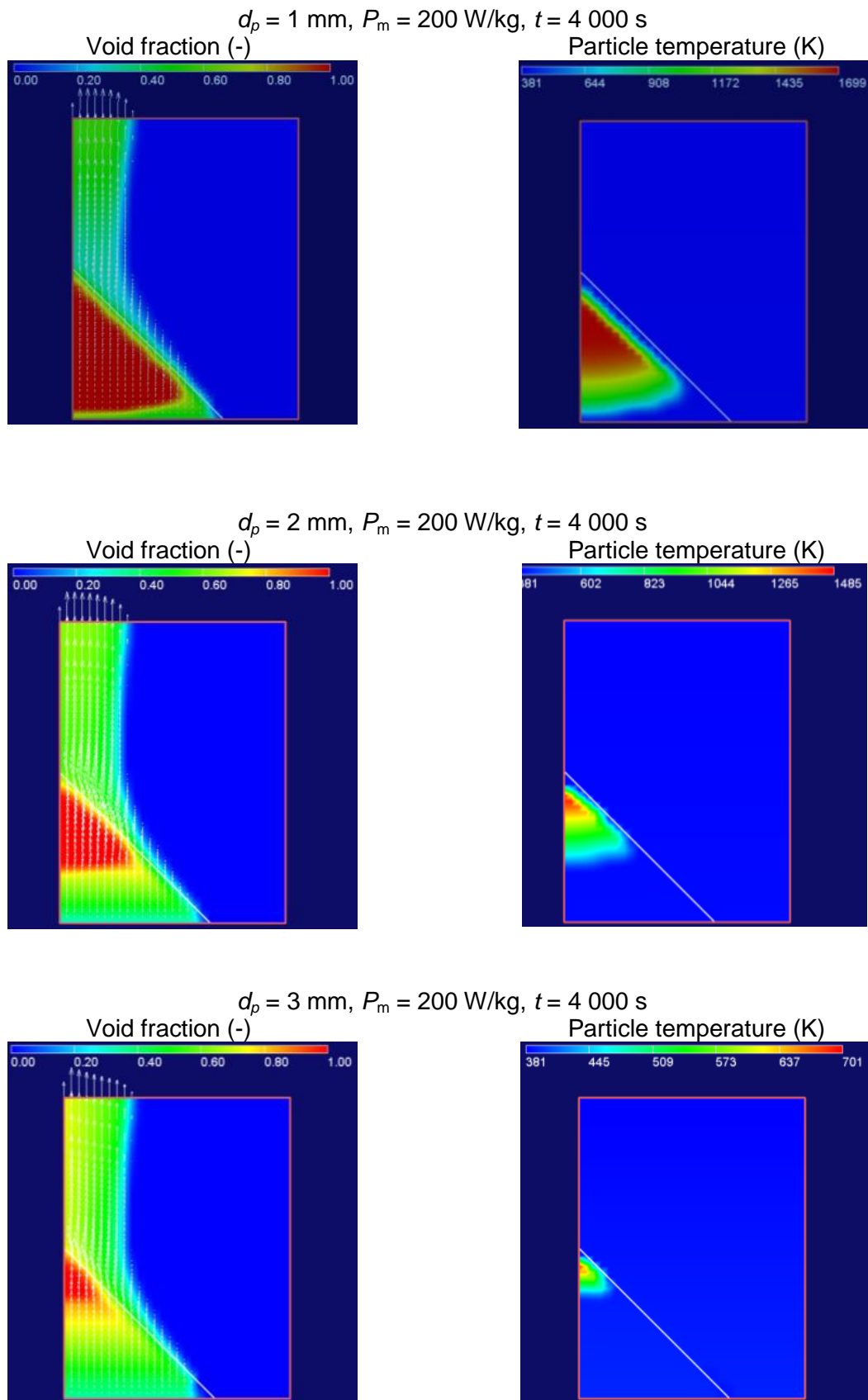


Figure 3. Void fraction (left) and solid particle temperature (right) in the DECOSIM simulations at the time of 4000 s for the conical beds of 1, 2 and 3 mm particles with the specific power equal to 200 W/kg (Yakush & Kudinov, 2014).

3. MEWA simulations

3.1 Background

Previously (Taivassalo & Takasuo, 2017), the behaviour of two types of hypothetical conical debris beds was studied by performing MEWA (Bürger et al., 2006, Rahman, 2013) simulations. Coolability and especially physical conditions after dryout were analysed for a reference reactor debris bed and for the conical debris beds studied at KTH by Yakush & Kudinov (2014) (c.f., Section 2).

The simulation results of the MEWA code were, however, not in a full agreement with the DECOSIM results introduced in Section 2 (Taivassalo & Takasuo, 2017). For the 1 mm particle cases without temperature stabilization, the codes agreed satisfactorily. On the other hand, these cases are not interesting because the maximum particle temperature eventually exceeds the temperatures where zirconium oxidation or even corium remelting begins. In the 3 mm particle cases, both the codes predicted that the beds are coolable but transient behaviours and final steady-state conditions were different. The differences between the codes were largest for the 2 mm particles as in the MEWA simulations steady-state conditions were reached in 5000 s but in the DECOSIM results the maximum particle temperature still increased (Figure 2). Therefore, before trying to quantify the temperature-based coolability criterion, it was considered essential to identify the origin of the significant differences between the MEWA and DECOSIM results.

Previous study (Taivassalo & Takasuo, 2017) examined different heat transfer models. A proper modelling of heat transfer was considered most important in the simulation of the post-dryout conditions. Alternative models available in MEWA for the solid-to-gas heat transfer coefficient and for the effective dry-bed thermal conductivity were tested. Their influence on the post-dryout behaviour of the particle bed could not explain the differences between the DECOSIM and MEWA results. It was thus concluded that coolability can be influenced also by the friction model. Accordingly, the influence of the friction model on the MEWA results will be discussed in this section.

3.2 On the features of the MEWA code

A detailed description of the updated models in the MEWA code is given by Rahman (2013). This report concentrates on the models considered of primary importance in modelling post-dryout conditions in a heated, idealised particle bed. The MEWA version dated 6.3.2014 was used in this study.

The MEWA code was recently validated by Huang and Ma (2018). Interestingly, the results for the Reed friction model were found to be in a good agreement with the experimental results. Unfortunately, it is not documented which version of the MEWA code was used in the validation study.

3.2.1 Conservation equations

A drying debris bed is hydrodynamically a three-phase problem. In most numerical simulations, the solid phase of particles is taken into account applying the porous medium approach and the liquid and gas phases are taken as fluids. In MEWA, debris bed behaviour is computed in two dimensions in Cartesian or cylindrical coordinate systems.

The mass conservation equations solved in MEWA are (Rahman, 2013)

$$\varepsilon \frac{\partial}{\partial t} (\alpha_i \rho_i) + \nabla \cdot (\varepsilon \alpha_i \rho_i \vec{v}_i) = (-1)^{(1+\delta_{ig})} \Gamma \quad (1)$$

where ε is the porosity (-), α_i is the volume fraction of the phase i (for the gas phase: $i=g$, for the liquid phase: $i=l$), ρ_i is the phase density (kg/m^3), \vec{v}_i is phase (pore) velocity (m/s), δ_{ig} is the Kronecker delta (-) and Γ is the mass source term due to evaporation ($\text{kg/m}^3/\text{s}$).

Simplified forms of the momentum equations are solved in MEWA (Equation (31) gives the full momentum equation for multiphase flows). The convective and viscous stress terms are ignored and the momentum equations are written as follows (Rahman, 2013):

$$0 = -\nabla p_i + \rho_i \vec{g} - \vec{F}_{s,i} - (-1)^{(1+\delta_{ig})} \frac{\vec{F}_i}{\alpha_i} \quad (2)$$

where p_i is the pressure of the phase (Pa), g is the gravitational acceleration (m/s^2), $\vec{F}_{s,i}$ is the drag force between the solid particles and a fluid phase i ($\text{kg/m}^2\text{s}^2$) and \vec{F}_i is the interfacial drag force between the fluid phases ($\text{kg/m}^2\text{s}^2$). (The inertial term is missing in Eq. (2) consistent with the MEWA documentation (Bürger et al., 2006, Rahman, 2013). In the MEWA code, the time-dependent term is included.)

The energy conservation equation for the fluid phases is (Rahman, 2013):

$$\varepsilon \frac{\partial}{\partial t} (\alpha_i \rho_i e_i) + \nabla \cdot (\varepsilon \alpha_i \rho_i \vec{v}_i h_i) = \nabla \cdot (\lambda_{i,eff} \nabla T_i) + Q_{s,i} + (-1)^{(1+\delta_{ig})} \Gamma h_{i,sat} \quad (3)$$

where e_i is the specific internal energy of the phase i (J/kg), h_i is the specific internal enthalpy of the phase i (J/kg), $h_{i,sat}$ is the specific enthalpy of the phase i at saturation (J/kg), $\lambda_{i,eff}$ is the effective thermal conductivity of the phase i (W/m·K), T_i is the phase temperature (K) and $Q_{s,i}$ is the heat flux from the solid phase to the fluid phase i (W/m^3). The effective thermal conductivity $\lambda_{i,eff}$ (W/m·K) is calculated from the phase thermal conductivity, $\lambda_{i,eff} = \lambda_i \varepsilon \alpha_i$.

In MEWA, the temperature of the bed particles is computed by solving the energy equation for the solid phase (Rahman, 2013):

$$\frac{\partial}{\partial t} [(1 - \varepsilon) \rho_s e_s] = \nabla \cdot (\lambda_{s,eff} \nabla T_s) + Q_{decay} - Q_{s,sat} - Q_{s,g} - Q_{s,l} \quad (4)$$

where ρ_s is the density of solid particles (kg/m^3), e_s is the specific internal energy of solid particles (J/kg), $\lambda_{s,eff}$ is the effective thermal conductivity of the solid particles (W/m·K) and T_s is the temperature of the solid particles (K). Q_{decay} (W/m^3) represents the internal (decay) heat generation in the solid particles. $Q_{s,sat}$, $Q_{s,g}$ and $Q_{s,l}$ (W/m^3) are the sources of heat due to the boiling at the particle surfaces (*sat*) as well as of the heat transfer rate from the particles to the gas (*g*) and liquid (*l*) phases, respectively. Since the focus of this study is on the post-dryout behaviour, in the conditions of the main interest the solid particles are in contact with the gas phase. Accordingly, boiling and heat transfer from the solid particles directly to the liquid phase are less important.

3.2.2 Closure models

3.2.2.1 Friction force models

A detailed discussion on the friction models of MEWA can be found in Rahman (2013).

In the MEWA code, the drag force between the solid particles and a fluid phase is calculated from the following formulation

$$\vec{F}_{s,i} = \frac{\varepsilon \alpha_i \mu_i}{K K_{r,i}} \vec{v}_i + \frac{\varepsilon^2 \alpha_i^2 \rho_i}{\eta \eta_{r,i}} |\vec{v}_i| \vec{v}_i \quad (5)$$

where the permeability K and passability η describe the capability of a porous medium to transmit fluid. They are expressed according to Ergun (1952) as

$$K = \frac{\varepsilon^3 d_p^2}{150(1-\varepsilon)^2} \quad (6)$$

$$\eta = \frac{\varepsilon^3 d_p}{1.75(1-\varepsilon)} \quad (7)$$

where d_p is the bed particle diameter.

The presence of the other fluid phase in the two-phase flow is taken account in the relative permeability $K_{r,i}$ (-) and relative passability $\eta_{r,i}$ (-) which are functions of the volume fraction

$$K_{r,i} = \alpha_i^n \quad (8)$$

$$\eta_{r,i} = \alpha_i^m \quad (9)$$

Classical friction models

There are several models for the relative permeability and passability. The powers n and m vary and depend on the respective experiments. For the relative permeability, $n = 3$ is typically used. For the relative passability, Lipinski (1982) suggested originally $m = 3$. Reed (1982) proposed $m = 5$ which yields a somewhat increased friction and was later on used also by Lipinski (1984). Later, in the model of Hu and Theofanous (1991), m was increased to 6. These three classical models differ from each other only in the relative passability with no explicit consideration of the gas-liquid drag (i.e., $\vec{F}_i = 0$). As the empirical models aim to describe the total pressure loss, the gas-liquid drag is implicitly included in the models.

Friction model of Tung and Dhir

To take explicitly into account the interfacial drag term \vec{F}_i , Tung and Dhir (1988) developed a detailed model in which the drag coefficients are calculated according to flow regimes. The flow regimes are given in Table 3 and in Figure 4. The upper boundary of bubble flow looks odd and originates to the fact, that Tund & Dhir (1988) considered only large particle cases, in which "pore size is much larger than the bubble diameter".

The bubble diameter is calculated as follows (Rahman, 2013)

$$d_b = 1.35 \sqrt{\frac{\sigma}{g(\rho_l - \rho_g)}} \quad (10)$$

where σ is the surface tension of water. The diameter of droplets is calculated from the same formula.

The relative permeability and passability for the liquid phase are

$$K_{r,l} = \alpha_l^3, \eta_{r,l} = \alpha_l^3 \quad (11)$$

Table 3. Flow regimes in the friction model of Tung and Dhir in the MEWA code (Rahman 2013).

	Flow regime	Void fraction range
Liquid continuous	Low void bubbly	$\alpha_g \leq \alpha_{g,0}; \quad \alpha_{g,0} = \text{MAX} \left[0, \frac{\pi(1-\varepsilon)}{3\varepsilon} \gamma(1+\gamma)(6\beta - 5(1+\gamma)) \right]$ $\gamma = \frac{d_b}{d_p}; \quad = \left[\frac{\sqrt{2}\pi}{6(1-\varepsilon)} \right]^{1/3}$
	High void bubbly	$\alpha_{g,0} < \alpha_g \leq \alpha_{g,1}; \quad \alpha_{g,1} = \text{MIN}[0.3, 0.6(1-\gamma)^2]$
	Transition	$\alpha_{g,1} < \alpha_g \leq \frac{\pi}{6}$
	Slug flow	$\frac{\pi}{6} < \alpha_g \leq 0.6$
Transition	Transition	$0.6 < \alpha_g \leq \frac{\sqrt{2}\pi}{6}$
Gas continuous	Annular flow	$\alpha_g > \frac{\sqrt{2}\pi}{6}$

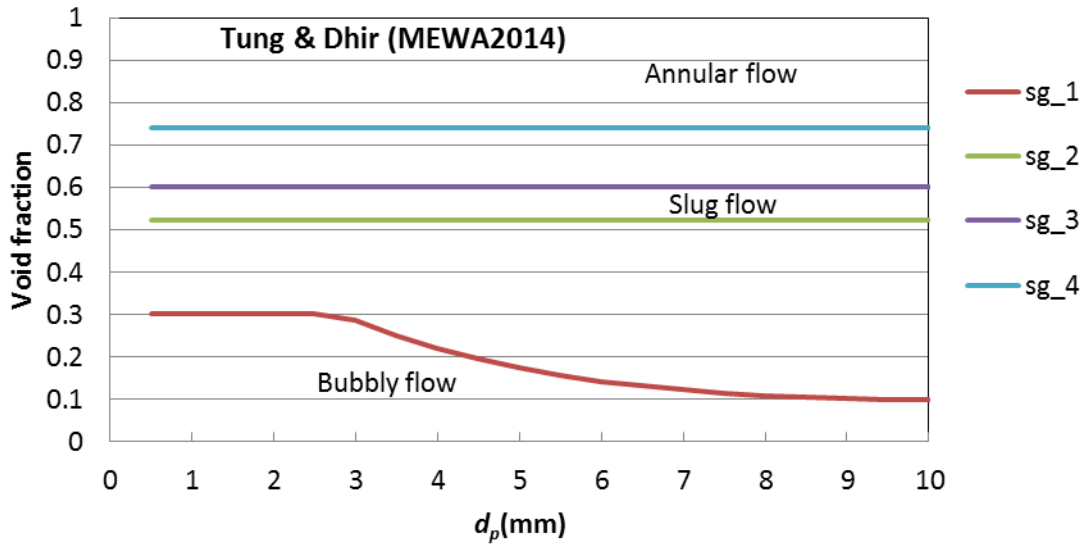


Figure 4. Flow regimes for the Tung and Dhir (Rahman, 2013). (For conditions at the tip of the bed cone.)

In case of the gas phase, the relative permeability and passability are formulated differently for flow regimes of continuous gas and continuous liquid flows. In bubbly and slug flows ($\alpha_g < 0.6$), the relative permeability and passability for the gas phase are as follows

$$K_{r,g} = \alpha_g^3 \left(\frac{1-\varepsilon}{1-\alpha_g\varepsilon} \right)^{\frac{4}{3}}, \quad \eta_{r,g} = \alpha_g^3 \left(\frac{1-\varepsilon}{1-\alpha_g\varepsilon} \right)^{\frac{2}{3}}. \quad (12)$$

In annular flows ($\alpha_g > \frac{\sqrt{2}\pi}{6} \approx 0.74$), the following expressions are applied:

$$K_{r,g} = \alpha_g^2 \left(\frac{1-\varepsilon}{1-\alpha_g\varepsilon} \right)^{\frac{4}{3}}, \quad \eta_{r,g} = \alpha_g^2 \left(\frac{1-\varepsilon}{1-\alpha_g\varepsilon} \right)^{\frac{2}{3}}. \quad (13)$$

In the transition region ($0.6 < \alpha_g < \frac{\sqrt{2}\pi}{6}$), the friction coefficient for the gas phase is interpolated.

The interfacial drag force between the gas and liquid phase determined differently for each flow regimes. The interfacial drag force is calculated from the friction coefficients $K_{g,l}$ given in Table 4 by multiplying with the velocity difference

$$\vec{F}_i = K_{g,l}(\vec{v}_g - \vec{v}_l). \quad (14)$$

Table 4. Drag force between the gas and liquid phases in the model of Tung and Dhir in the MEWA code (Rahman, 2013).

	Flow regime	Void fraction range
Liquid continuous	Low void bubbly	$K_{g,l} = 18 \frac{1+\gamma}{2} \ln\left(1 + \frac{2}{\gamma}\right) \frac{\alpha_g \alpha_l \mu_l}{d_b^2} + 0.34 \left[\frac{1+\gamma}{2} \ln\left(1 + \frac{2}{\gamma}\right) \right]^2 \alpha_g \alpha_l^5 \frac{\alpha_g \rho_g + \alpha_l \rho_l}{d_b} \vec{v}_g - \vec{v}_l $
	High void bubbly	$K_{g,l} = 18 \left[\alpha_{g,0} \frac{1+\gamma}{2} \ln\left(1 + \frac{2}{\gamma}\right) + \alpha_g - \alpha_{g,0} \right] \frac{\alpha_l \mu_l}{d_b^2} + 0.34 \left\{ \alpha_{g,0} \left[\frac{1+\gamma}{2} \ln\left(1 + \frac{2}{\gamma}\right) \right]^2 + \alpha_g - \alpha_{g,0} \right\} \alpha_l^5 \frac{\alpha_g \rho_g + \alpha_l \rho_l}{d_b} \vec{v}_g - \vec{v}_l $
	Transition	Interpolated
	Slug flow	$K_{g,l} = 5.21 \frac{\alpha_l \alpha_g \mu_l}{d_b^2} + 0.92 \alpha_g \alpha_l^5 \frac{\alpha_g \rho_g + \alpha_l \rho_l}{d_b} \vec{v}_g - \vec{v}_l $
Transition	Transition	Interpolated
Gas continuous	Annular flow	$K_{g,l} = \frac{\varepsilon \alpha_l \mu_g}{K \alpha_g^2} \left(\frac{1-\varepsilon}{1-\alpha_g \varepsilon} \right)^{-\frac{4}{3}} + \frac{\varepsilon^2 \alpha_l \rho_g}{\eta \alpha_g} \left(\frac{1-\varepsilon}{1-\alpha_g \varepsilon} \right)^{-\frac{2}{3}} \vec{v}_g - \vec{v}_l $

Modified Tung and Dhir friction model

The Tung and Dhir model is not working satisfactorily in pure top-flooding cases. If particles are small, this is not unexpected since the Tung and Dhir model was not developed for those conditions. Therefore, some modifications have been proposed. A modification was made by Schmidt (2007) but it is not currently used in MEWA. It was however used in the DECOSIM simulations discussed in Section 2. The Schmidt version of the modified Tung and Dhir model was added in the Fluent implementation of the debris bed models and is introduced in Section 4.2.2.

Currently MEWA (the 2014 version) applies a different modification of the model of Tung and Dhir. The flow regimes in the recent MEWA version of the modified Tung and Dhir model are depicted in Figure 5 and Table 5. In the modified Tung and Dhir model of MEWA, the relative

permeability and passability for the friction between the gas phase and solid particles are formulated as follows: In the liquid-continuous regime ($\alpha_g < 0.6$),

$$K_{r,g} = \alpha_g^3, \quad \eta_{r,g} = \alpha_g^3 \quad (15)$$

and in the gas continuous regime ($\alpha_g > \frac{\sqrt{2}\pi}{6} \approx 0.74$),

$$K_{r,g} = \alpha_g^2, \quad \eta_{r,g} = \alpha_g^2. \quad (16)$$

In the transition region ($0.6 < \alpha_g < \frac{\sqrt{2}\pi}{6}$), the friction coefficient for the gas phase is interpolated.

The relative permeability and passability for the liquid phase are

$$K_{r,l} = \alpha_l^2, \quad \eta_{r,l} = \alpha_l^5. \quad (17)$$

The drag force between the gas and liquid phases is formulated as follows

$$K_{g,l} = K_{g,l,TD} \text{MIN} \left[1, \frac{d}{0.012\text{m}} \right] \quad (18)$$

for the bubbly and slug flows and as

$$K_{g,l} = 0.25 K_{g,l,TD} \text{MIN} \left[1, \left(\frac{d}{0.003\text{m}} \right)^3 \right] \quad (19)$$

for the annular flow regime. Here $K_{g,l,TD}$ is the interfacial drag according to the original Tung and Dhir model for the flow regime in question. (In the MEWA codes used, the constant of 0.25 in Eq. (19) is 0.2 and if the porosity is at least 0.8, the interfacial drag force is ignored).

Table 5. Flow regimes in the modified Tung and Dhir model of MEWA (Rahman, 2013).

	Flow regime	Void fraction range
Liquid continuous	Low void bubbly	$\alpha_g \leq \alpha_{g,0}; \quad \alpha_{g,0} = \text{MAX} \left[0., \frac{\pi(1-\varepsilon)}{3\varepsilon} \gamma(1+\gamma)(6\beta - 5(1+\gamma)) \right]$ $\gamma = \frac{d_b}{d_p}; \quad = \left[\frac{\sqrt{2}\pi}{6(1-\varepsilon)} \right]^{1/3}$
	High void bubbly	$\alpha_{g,0} < \alpha_g \leq \alpha_{g,1}; \quad \alpha_{g,1TD} = \text{MIN}[0.3, 0.6(1-\gamma)^2]$ $\alpha_{g,1} = \text{MIN}[\alpha_{g,1TD}, 400000(d_p - d_{p,0})^3 + \alpha_{g,1TD}]; \quad d_{p,0} = 12 \text{ mm}$
	Transition	$\alpha_{g,1} < \alpha_g \leq \text{MIN} \left[\frac{\pi}{6}, 400000(d_p - d_{p,0})^3 + \frac{\pi}{6} \right]$
	Slug flow	$\text{MIN} \left[\frac{\pi}{6}, 400000(d_p - d_{p,0})^3 + \frac{\pi}{6} \right] < \alpha_g$ $\leq \text{MIN}[0.6, 400000(d_p - d_{p,0})^3 + 0.6]$
Transition	Transition	$\text{MIN}[0.6, 400000(d_p - d_{p,0})^3 + 0.6] < \alpha_g$ $\leq \text{MIN} \left[\frac{\sqrt{2}\pi}{6}, 400000(d_p - d_{p,0})^3 + \frac{\sqrt{2}\pi}{6} \right]$
Gas continuous	Annular flow	$\alpha_g > \text{MIN} \left[\frac{\sqrt{2}\pi}{6}, 400000(d_p - d_{p,0})^3 + \frac{\sqrt{2}\pi}{6} \right]$

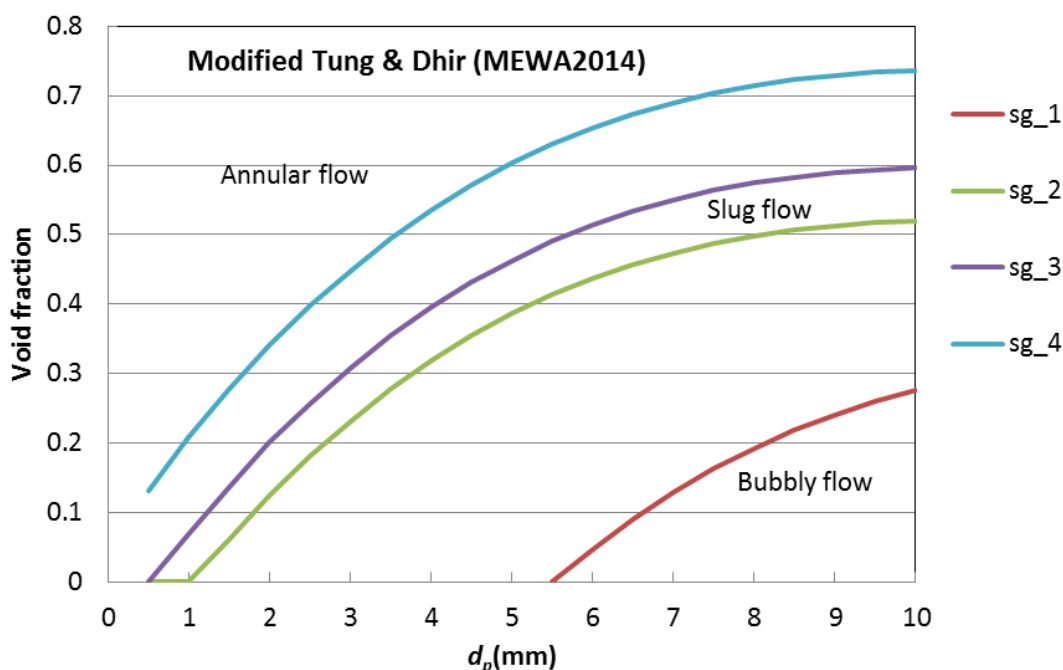


Figure 5. Flow regimes for the modified Tung and Dhir in MEWA (Rahman, 2013). (For conditions at the tip of the bed cone.)

3.2.2.2 Heat transfer

Effective thermal conductivity in a dry bed

The effective thermal conductivity of the solid particles $\lambda_{s,eff}$ in the energy balance equation (Equation (4)) is a bulk property, which describes the ability of multi-component porous medium to conduct heat. It accounts for the combined effects of conduction through the contact points of the solid particles and through the fluid, and possibly radiation across the fluid space and convection in the pores.

In MEWA, there are two alternative basic approaches for calculating the effective thermal conductivity for a dry bed (Taivassalo & Takasuo, 2017):

- (i) The first approach is the conductivity model of Imura (Imura & Takegoshi, 1974) combined with a radiation model. For the radiation model, there are three options: the Yagi (Yagi & Kunii, 1957), Vortmeyer (1978) and Luikov (Luikov et al., 1968) models.
- (ii) The second approach is the Maxwell model for predicting the properties of a heterogeneous medium (Maxwell 1873, p. 365).

The Maxwell model does not include radiative heat transfer, and it is best suited for particles dispersed in a continuous medium (very large porosity). Therefore, the other conduction-radiation combinations can be considered as the primary models for calculating the effective thermal conductivity in packed low-porosity beds. In MEWA, the default model for the effective dry-bed thermal conductivity $\lambda_{s,eff}$ is the Imura conductivity model with the radiation model of Yagi. In this study, the default model was applied.

Heat transfer between particles and gas

In the pre-dryout conditions, the solid particles, liquid and gas are considered to be close to a thermal equilibrium at the saturation temperature. Heat released in the solid particles is mainly used in evaporation. The heat transfer rate from the solid particles to steam becomes important close to dryout and especially after dryout, when the temperature of the solid particle increases.

In MEWA the heat transfer rate from the particles to the gas phase is given by

$$Q_{s,g} = a_{s,g} \kappa_{s,g} (T_s - T_g) \quad (20)$$

where the interfacial area density $a_{s,g}$ is given by

$$a_{s,g} = \frac{6(1 - \varepsilon) (\alpha_g - 0.7)}{d_p \cdot 0.3} \quad (21)$$

if $\alpha_g \geq 0.7$ (continuous gas phase) otherwise $a_{s,g} = 0$. The heat transfer coefficient $\kappa_{s,g}$ (W/m²K) in Eq. (20) is calculated on the basis of the Nusselt number $Nu_{s,g}$ as follows

$$\kappa_{s,g} = \frac{Nu_{s,g} \lambda_g}{D_p} \quad (22)$$

Here λ_g is the thermal conductivity of the gas phase (W/m·K).

There are the following three alternatives in MEWA to define the heat transfer coefficient $\kappa_{s,g}$ for heat transfer from the solid particles to the gas phase. In practice, a user selects a method to determine the Nusselt number $Nu_{s,g}$.

- (i) In the default model, the Nusselt number is calculated from a simple formula

$$Nu_{s,g} = 2 + 0.6 \sqrt{Re_g} \quad (23)$$

In Eq. (23), Re_g is the dimensionless Reynolds number

$$Re_g = \frac{|\vec{v}_g \rho_g D_p|}{\eta_g} \quad (24)$$

where \vec{v}_g is the gas velocity (m/s) and η_g is the gas viscosity (Pa·s).

- (ii) The second option is the model of Gnielinski (Stephan et. al., 2010, p. 743), in which both the laminar and turbulent Nusselt numbers are calculated as follows

$$Nu_{s,g}^{lam} = 0.644 \sqrt{Re_g} \sqrt[3]{Pr_g} \quad (25)$$

$$Nu_{s,g}^{turb} = 0.037 \frac{Re_g^{0.8} Pr_g}{1 + 2.443 Re_g^{-0.1} (Pr_g^{\frac{2}{3}} - 1)} \quad (26)$$

Here Pr_g is the Prandtl number

$$Pr_g = \frac{\eta_g c_{p,g}}{\lambda_g} \quad (27)$$

where $c_{p,g}$ is the specific heat capacity of the gas phase (J/kgK). The heat transfer coefficient is calculated from Eq. (22) using the Nusselt number obtained from the following formula

$$Nu_{s,g} = \left[2 + \sqrt{(Nu_{s,g}^{lam})^2 + (Nu_{s,g}^{turb})^2} \right] \left[1 + \frac{2}{3} (1 - \varepsilon) \right] \quad (28)$$

- (iii) A user defined constant value is the third alternative to determine the Nusselt number.

This default option (i) was used in this study.

Boiling heat transfer

The local boiling rate is obtained by dividing the heat flux rate from the solid with the latent heat of evaporation:

$$\Gamma = \frac{Q_{s,sat}}{\Delta H_{evap}} \quad (29)$$

To calculate the boiling heat transfer coefficient, the Rohsenow correlation (Rohsenow, 1952) is applied for nucleate pool boiling regime and the Lienhard correlation (Lienhard, 1987) for the film boiling regime (with transition zone calculated by an interpolation function).

3.3 Computational cases

The computational domain and mesh with the (ideal) shape of the analysed beds are shown in Figure 6. The domain and mesh are axisymmetric respect to the vertical axis of the beds. The DECOSIM mesh is also presented in Figure 6 for comparison. The MEWA mesh is very similar to the mesh applied in the DECOSIM simulations (Yakush & Kudinov, 2014). In the radial direction, the mesh features 30 15 cm cell columns. Vertically there are 51 cell layers with a varying thickness.

The orange area in the MEWA mesh representation in Figure 6 shows the domain defined as particle bed. In the MEWA computations, the cells with centres located in the orange area are considered to represent the particle bed. The actual shape of the particle beds used in numerical simulations is shown in Figure 7. In the simulations, the bed shape follows approximatively, within the used spatial discretisation, the theoretical conical shape of an ideal bed.

In Figure 7 the cells are coloured according to the porosity. In the MEWA simulations, the porosity must always be less than 0.95. In this work, the porosity was assumed to be 0.9 in the cells representing the pool. In order to reduce the friction forces, the particle diameter in the pool area was set to 10 mm.

The conditions and physical properties were set in the MEWA simulations consistent with the DECOSIM simulations discussed in Section 2. MEWA simulations were performed for the same combinations of the particle size and heating power as the DECOSIM simulations and given in Table 2. The 2014 version of the MEWA code was used in the simulations.

The default models were used for the effective thermal conductivity in a dry bed and for the heat transfer between the particles and the gas. This work concentrates on influences of the model applied for the friction forces. In the following, MEWA results for the friction models of Lipinski, Reed, Tung and Dhir as well as for the MEWA version of the modified Tung and Dhir friction model will be presented.

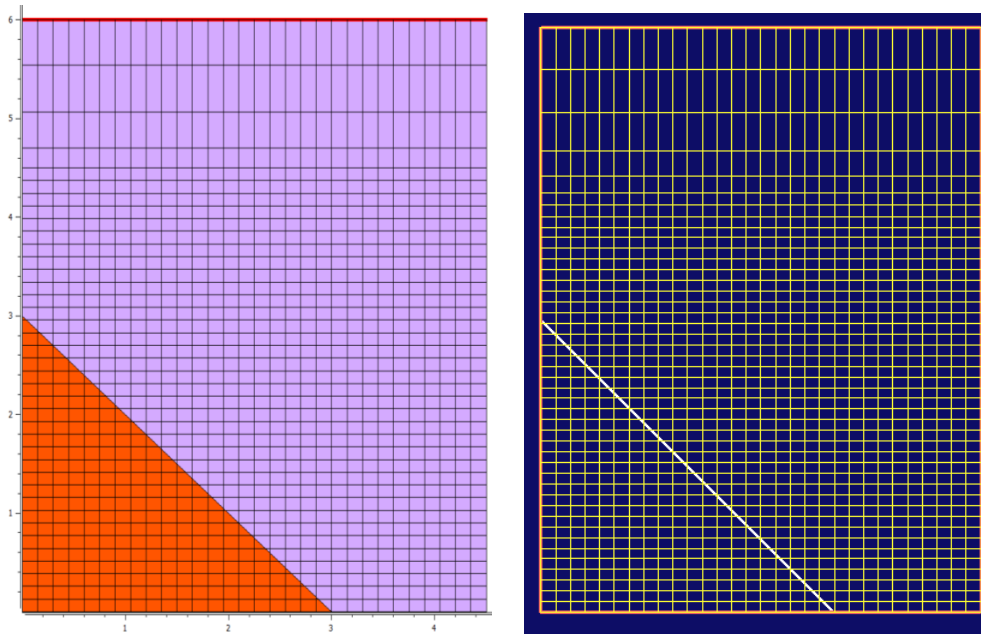


Figure 6. Computational domain, mesh and bed shape for the conical debris beds studied computationally with MEWA in this study (left) and in the DECOSIM simulations of Yakush & Kudinov (2014) (right). The orange area represents the shape of an ideal conical particle bed.

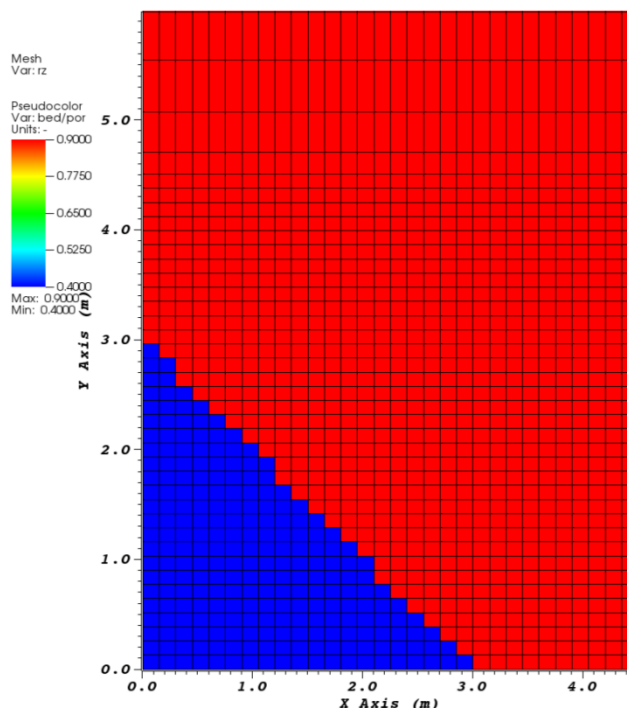


Figure 7. Actual computational shape of the heated particle bed (the blue area) in the MEWA simulation for the conical debris beds studied at KTH (Yakush & Kudinov, 2014). The cells are coloured by the porosity.

3.4 Results

The maximum particle temperature as a function of the time in the simulation case of the 1 mm particle and the specific heating power of 150 W/kg is plotted in Figure 8 for all the four friction models considered. Figure 9 shows distributions of the void fraction and particle temperature at the time of about 4000 s. The corresponding results for the same particle size with the specific heating power of 200 W/kg are presented in Figure 10 and Figure 11.

In case of 1 mm particles, the influence of the friction model is small especially in the particle bed. In the pool, the differences in the calculated friction force lead to different gas velocities and thus to different void fraction values. The maximum particle temperature is almost totally insensitive to the friction model. This is expectable, since because of a large drag force, the gas phase velocity and mass flux are small resulting in a small cooling effect of steam. After dryout the maximum particle temperature increases almost as it would increase without any cooling. The MEWA results indicate that in both the cases high temperature and even the corium melting temperature of 2700 K would finally be achieved in the upper part of the dry zone.

Considering the cases of 2 mm particles, the void fraction and particle temperature in the MEWA simulations are shown in Figure 12, Figure 13, Figure 14 and Figure 15. Differences to the 1 mm results are significant. For the specific heating power of 150 W/kg (Figure 12 and Figure 13), dryout is not achieved with the Tung and Dhir or modified Tung and Dhir friction models. In addition, with the friction model of Lipinski, the dry area is small and the maximum particle temperature stabilizes to a low value of 581 K. When the specific power is 200 W/kg (Figure 14 and Figure 15), dryout is obtained with all the friction models studied and differences in results are reasonable. The maximum particle temperatures stabilize at about 5000 s to values close to each other except in case of the Reed model with which the dry area is somewhat larger and the maximum particle temperature would increase for another 1000 - 2000 s to a value of approximately 300 degrees larger than steady-state values of the other models.

For 3 mm particles with the specific heating power equal to 200 W/kg, the computational results for the void fraction and particle temperature (Figure 16 and Figure 17) are quite similar as in the case of the 2 mm particles and the specific heating power of 150 W/kg (Figure 12 and Figure 13). Even the maximum particle temperature ends up to almost the same values (Figure 12 and Figure 16).

The computed maximum particle temperature as a function of the simulation time for the 3 mm particles with the specific heating power equal to 250 W/kg is plotted in Figure 18 for all the four friction models. With all models, steady states are achieved at about 1000 - 3000 s and the maximum particle temperature stabilizes but to very different values. Figure 19 shows distributions of the void fraction and particle temperature at the time of about 4000 s. With the Tung and Dhir as well as with the modified Tung and Dhir friction models, the dryout zone is small in area.

In summary, the influences of the model applied for the friction force is stronger for large particles than for the small ones. The cooling effect of steam is significant with the large particles and therefore any changes in the friction force influence the cooling efficiency and the particle temperature. For small (1 mm) particles, the steam flow is with all the friction models so small that the cooling effect of the stem flow is not important and the maximum particle temperature increases almost as without cooling.

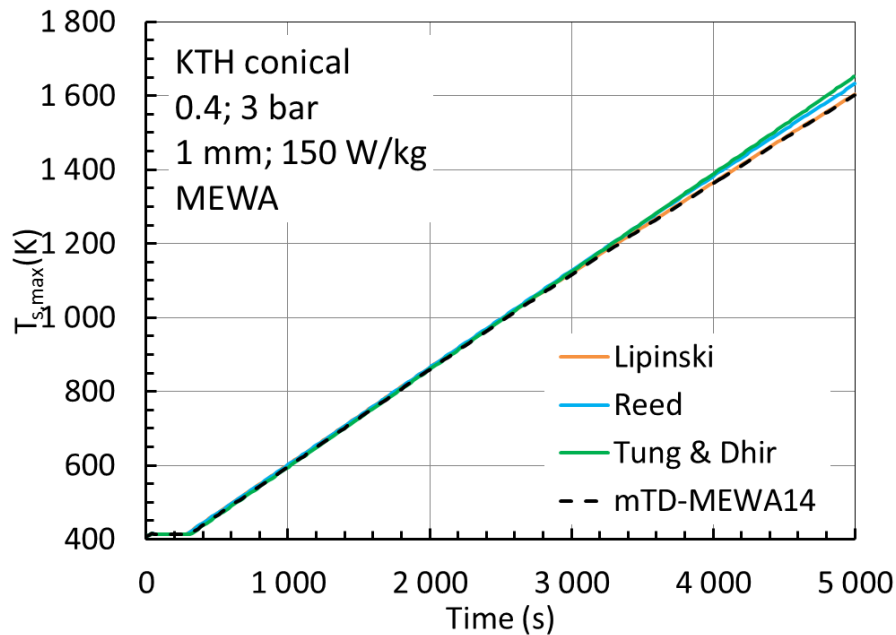


Figure 8. Influence of the friction model (Section 3.2.2.1) on the time evolution of the maximum particle temperature in the MEWA simulations for the conical debris bed of the specific heating power equal to 150 W/kg and the particle diameter equal to 1 mm.

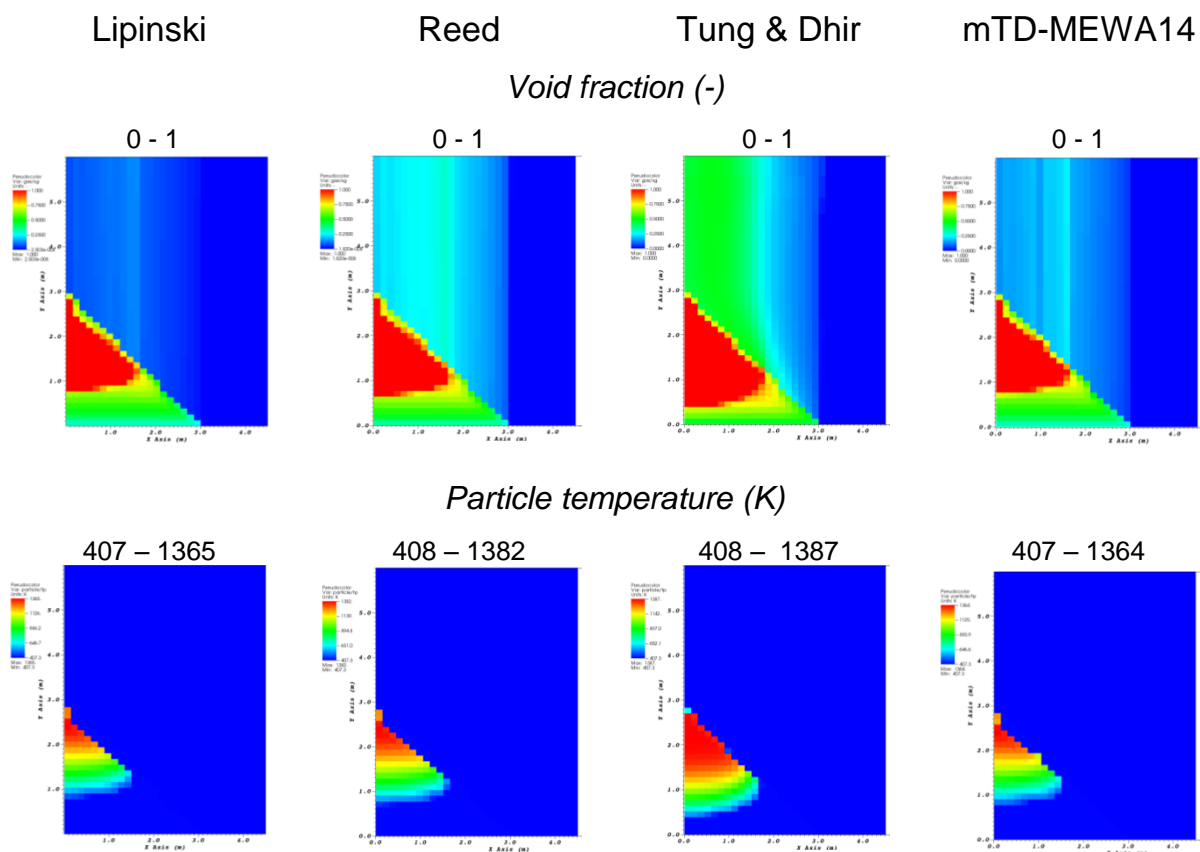


Figure 9. Void fraction (top row) and solid particle temperature (bottom row) 4000 s after the start of heating in the MEWA simulations for the conical debris bed studied of the specific heating power equal to 150 W/kg and the particle diameter equal to 1 mm for (from the left) the Lipinski, Reed, Tung and Dhir friction models as well as for the modified Tung and Dhir friction models. (The temperature contour range varies and the contour-plot specific ranges are given above the contour plots.)

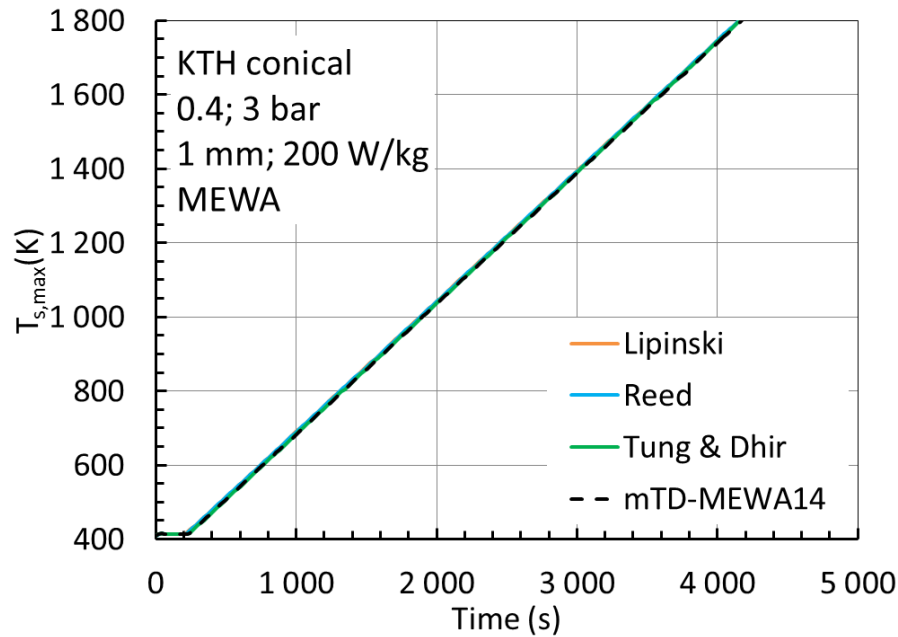


Figure 10. Influence of the friction model (Section 3.2.2.1) on the time evolution of the maximum particle temperature in the MEWA simulations for the conical debris bed of the specific heating power equal to 200 W/kg and the particle diameter equal to 1 mm.

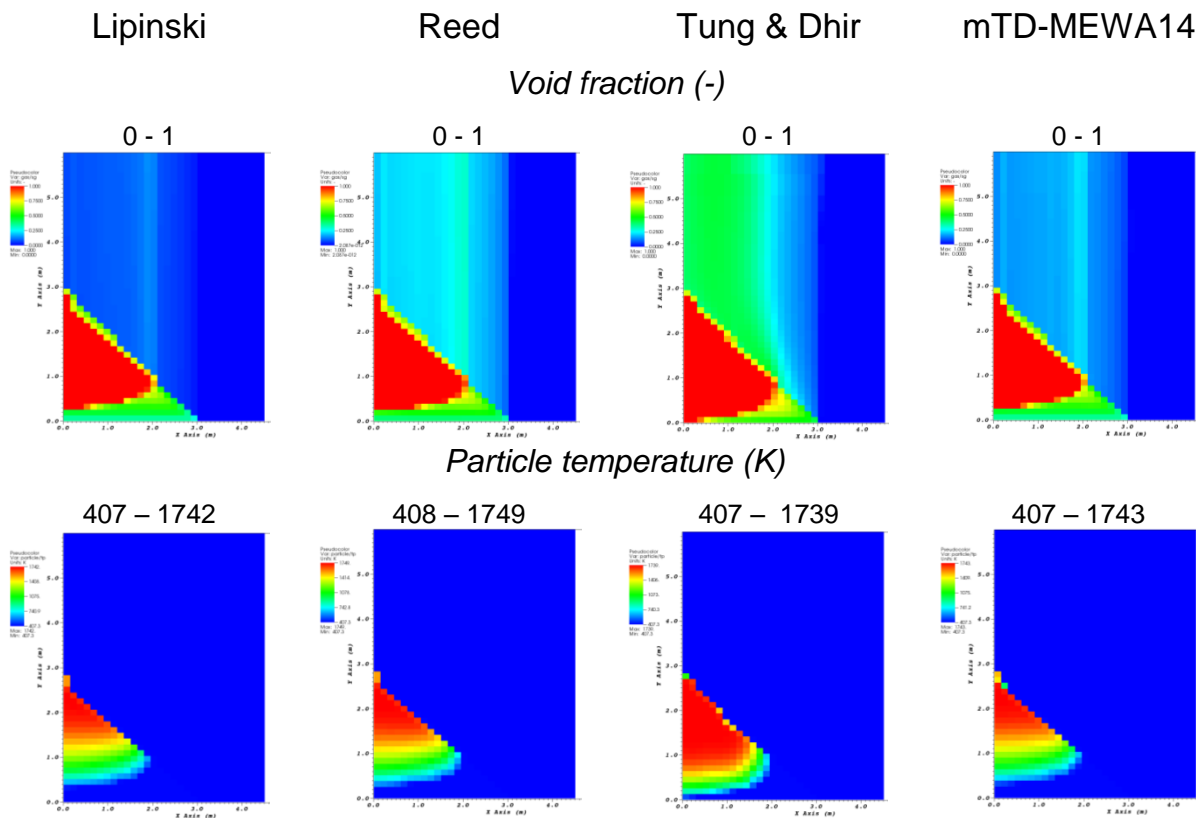


Figure 11. Void fraction (top row) and solid particle temperature (bottom row) 4000 s after the start of heating in the MEWA simulations for the conical debris bed of the specific heating power equal to 200 W/kg and the particle diameter equal to 1 mm for (from the left) the Lipinski, Reed, Tung and Dhir friction models as well as for the modified Tung and Dhir friction models. (The temperature contour range varies and the contour-plot specific ranges are given above the contour plots.)

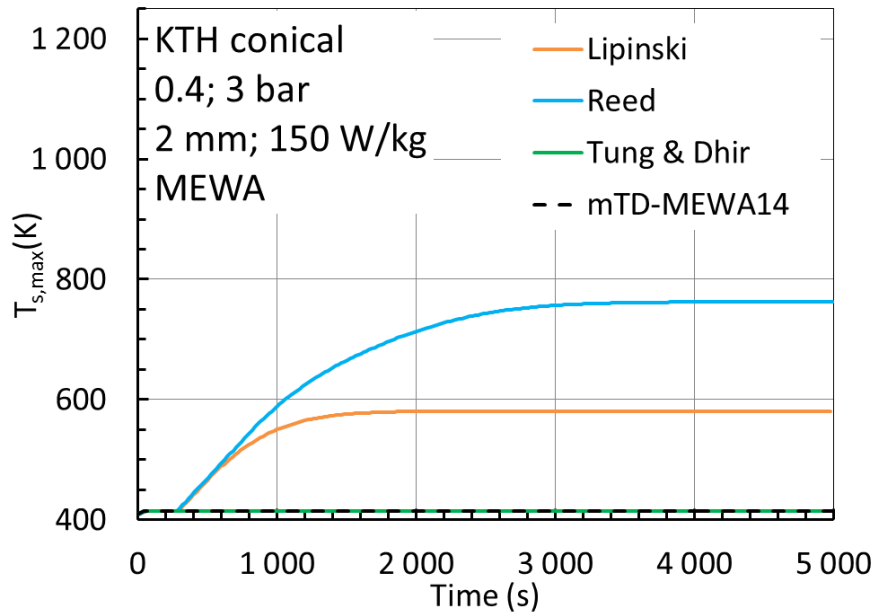


Figure 12. Influence of the friction model (Section 3.2.2.1) on the time evolution of the maximum particle temperature in the MEWA simulations for the conical debris bed of the specific heating power equal to 150 W/kg and the particle diameter equal to 2 mm.

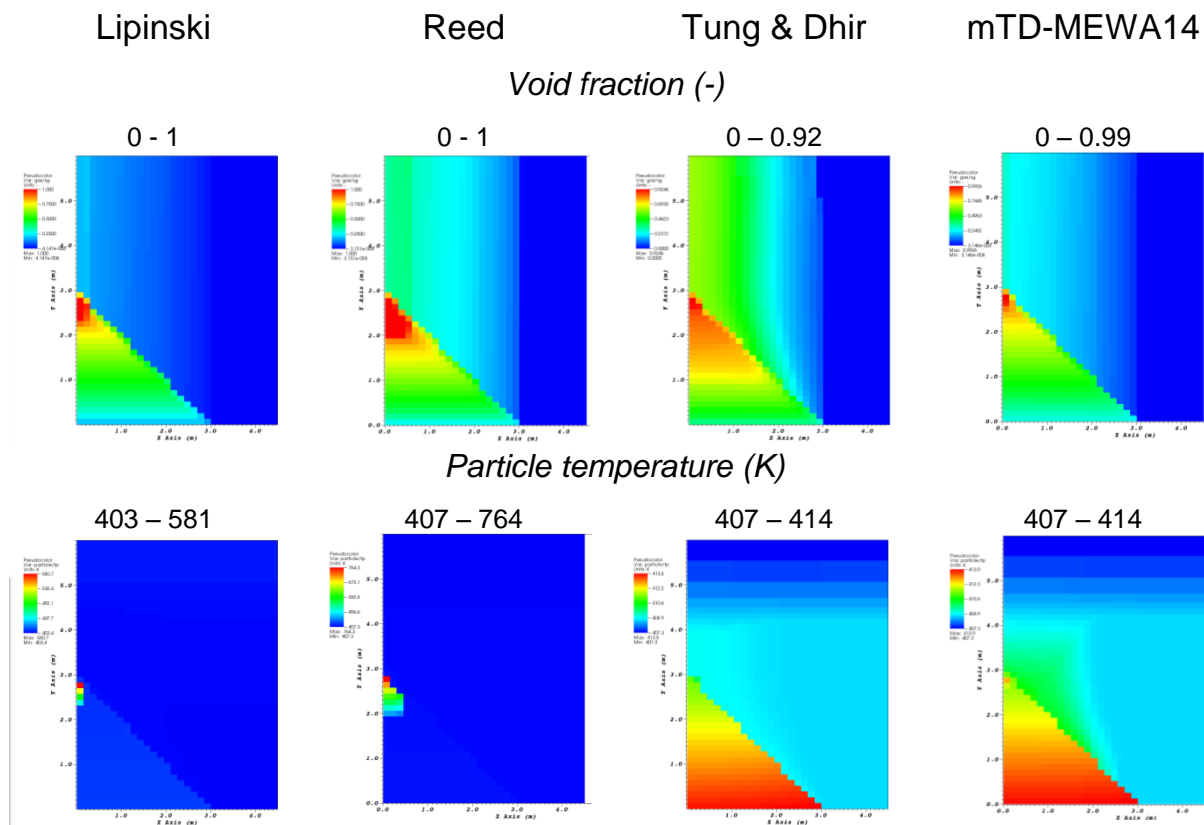


Figure 13. Void fraction (top row) and solid particle temperature (bottom row) 4000 s after the start of heating in the MEWA simulations for the conical debris bed of the specific heating power equal to 150 W/kg and the particle diameter equal to 2 mm for (from the left) the Lipinski, Reed, Tung and Dhir friction models as well as for the modified Tung and Dhir friction models. (The contour range varies and the contour-plot specific ranges are given above the contour plots.)

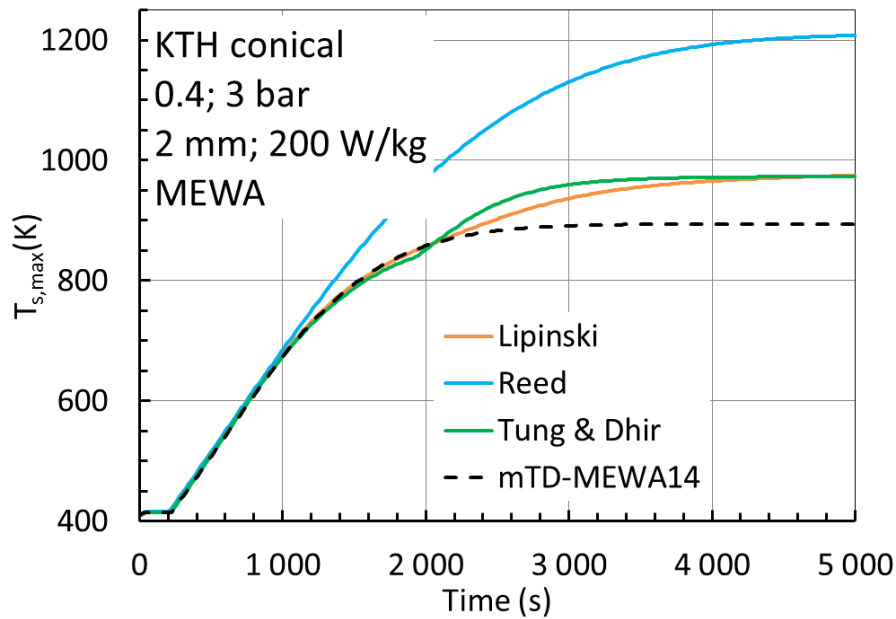


Figure 14. Influence of the friction model (Section 3.2.2.1) on the time evolution of the maximum particle temperature in the MEWA simulations for the conical debris bed of the specific heating power equal to 200 W/kg and the particle diameter equal to 2 mm.

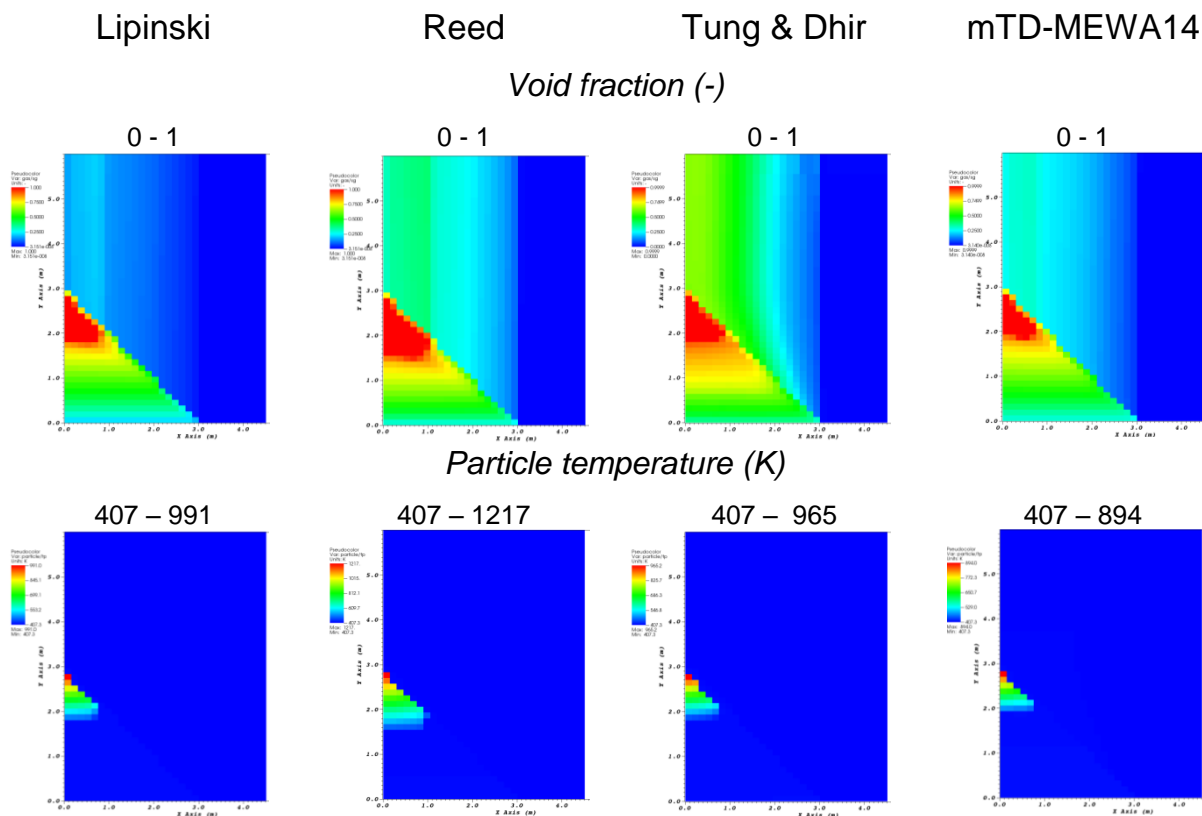


Figure 15. Void fraction (top row) and solid particle temperature (bottom row) 4000 s after the start of heating in the MEWA simulations for the conical debris bed of the specific heating power equal to 200 W/kg and the particle diameter equal to 2 mm for (from the left) the Lipinski, Reed, Tung and Dhir friction models as well as for the modified Tung and Dhir friction models. (The temperature contour range varies and the contour-plot specific ranges are given above the contour plots.)

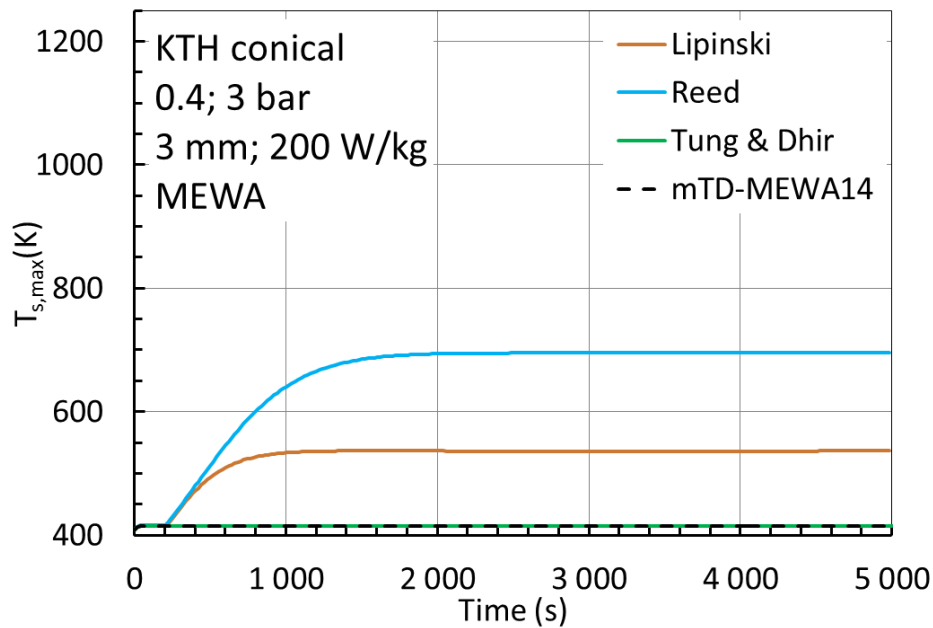


Figure 16. Influence of the friction model (Section 3.2.2.1) on the time evolution of the maximum particle temperature in the MEWA simulations for the conical debris bed of the specific heating power equal to 200 W/kg and the particle diameter equal to 3 mm.

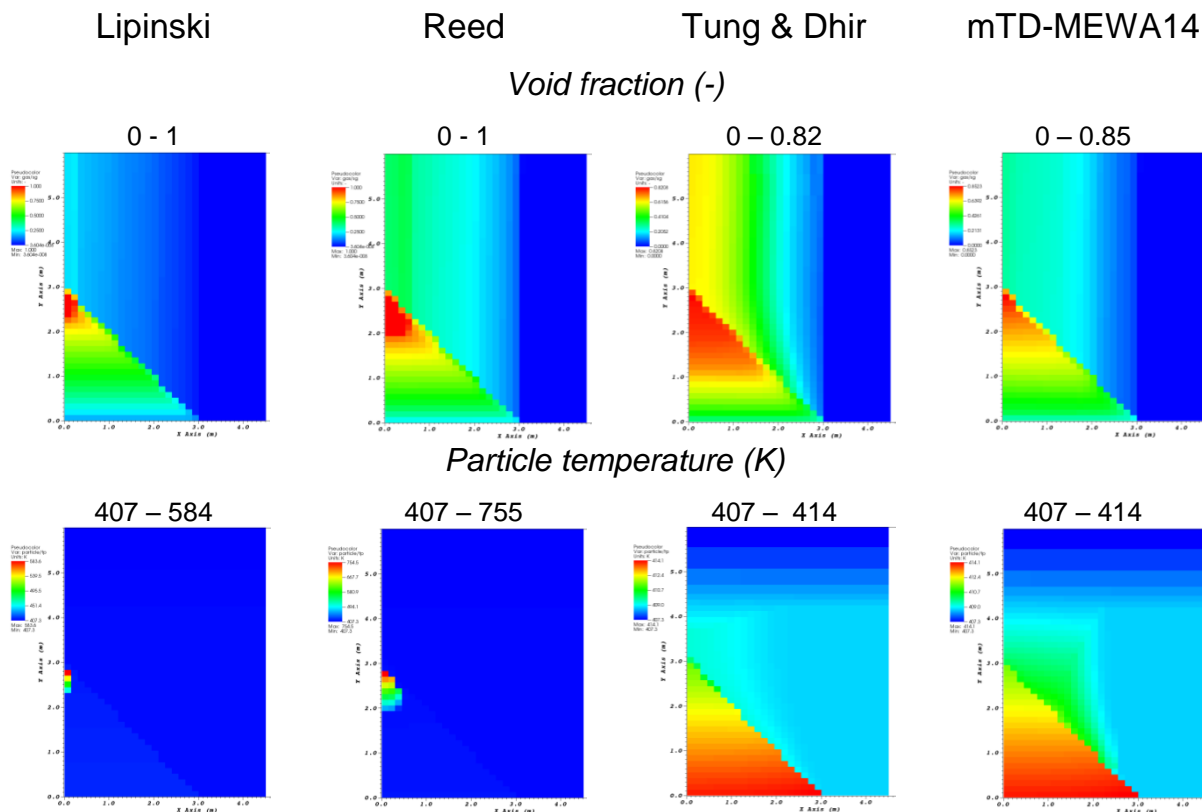


Figure 17. Void fraction (top row) and solid particle temperature (bottom row) 4000 s after the start of heating in the MEWA simulations for the conical debris bed of the specific heating power equal to 200 W/kg and the particle diameter equal to 3 mm for (from the left) the Lipinski, Reed, Tung and Dhir friction models as well as for the modified Tung and Dhir friction models. (The contour range varies and the contour-plot specific ranges are given above the contour plots.)

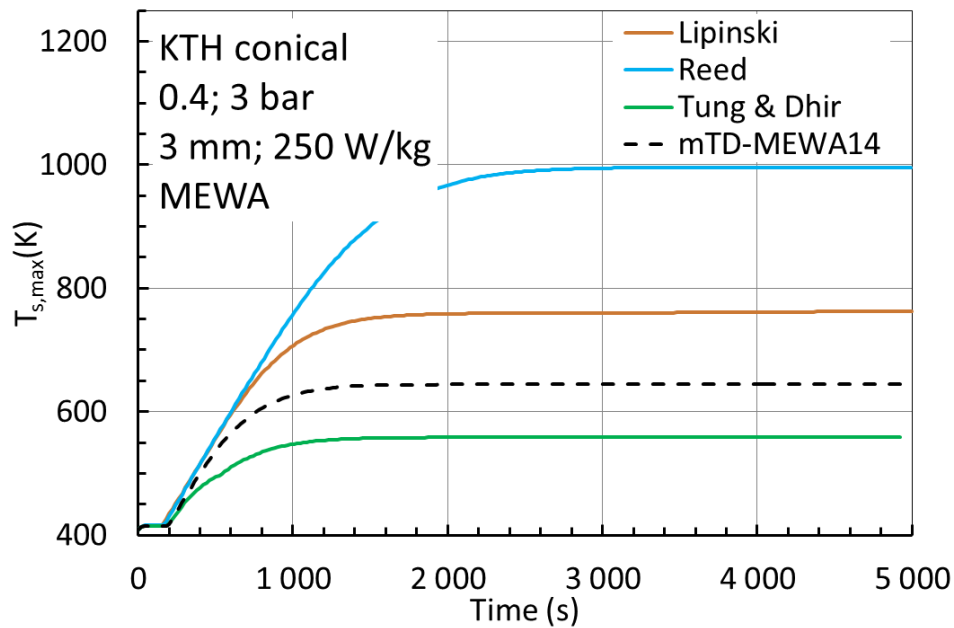


Figure 18. Influence of the friction model (Section 3.2.2.1) on the time evolution of the maximum particle temperature in the MEWA simulations for the conical debris bed of the specific heating power equal to 250 W/kg and the particle diameter equal to 3 mm.

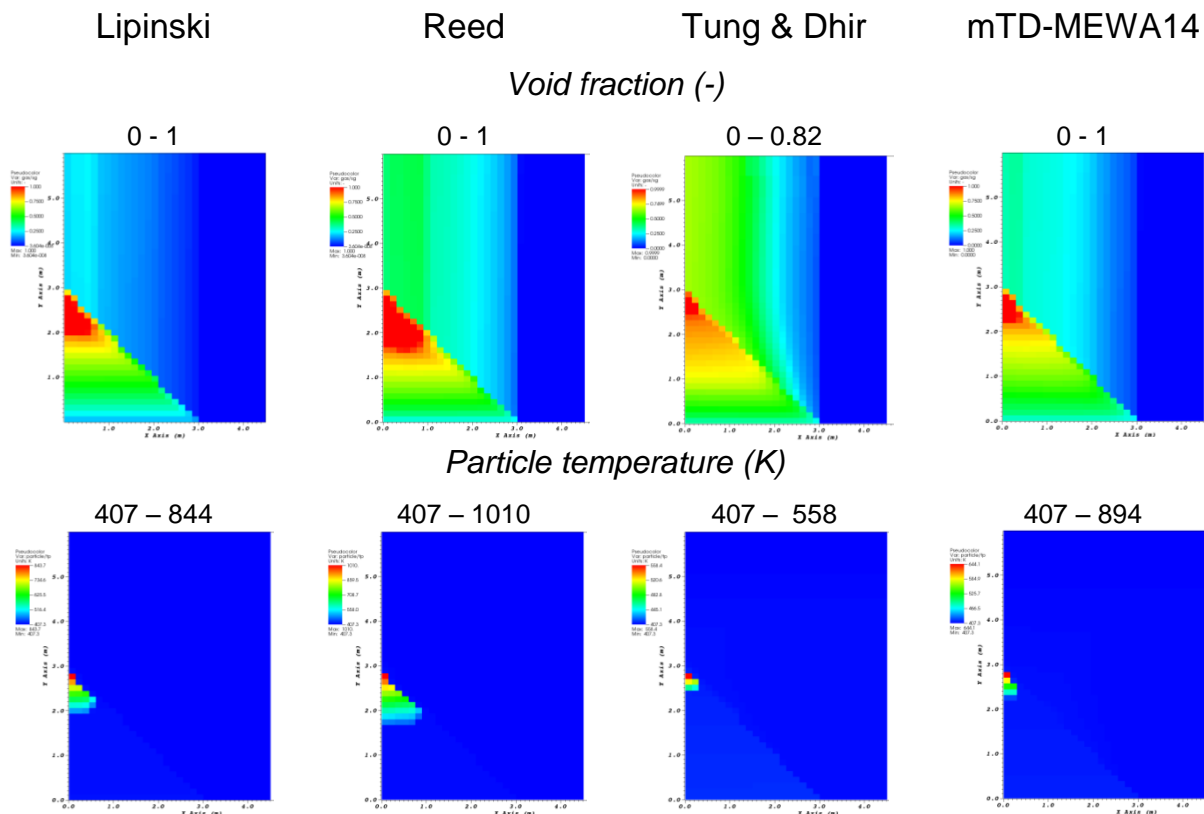


Figure 19. Void fraction (top row) and solid particle temperature (bottom row) 4000 s after the start of heating in the MEWA simulations for the conical debris bed of the specific heating power equal to 250 W/kg and the particle diameter equal to 3 mm for (from the left) the Lipinski, Reed, Tung and Dhir friction models as well as for the modified Tung and Dhir friction models. (The contour range varies and the contour-plot specific ranges are given above the contour plots.)

3.5 Comparison of the MEWA and DECOSIM results

The MEWA and DECOSIM results for the time evolution of the maximum particle temperature are compared in Figure 20. The modified Tung and Dhir friction model of MEWA (the 2014 version) was applied in the MEWA simulations and the Schmidt (2007) version of the modified Tung and Dhir model has been applied by Yakush & Kudinov (2014). Distributions of the void fraction and solid particle temperature at the time of about 4000 s are shown in Figure 21 for those conical bed cases for which contour plots are given in Yakush & Kudinov (2014).

For the 1 mm particles, the agreement is good (a potential reason for the small time shift is discussed below). For larger particles, there are significant differences and as the friction model is important with the 2 and 3 mm particles as discussed above, the differences can likely arise from the differences in the friction models. Steady states are achieved in the MEWA simulations in all large particle cases and the maximum particle temperature stabilises to reasonably low values. With the lowest values of the heating power, dryout does not occur in the MEWA simulations.

The maximum particle temperature in the DECOSIM results is significantly higher for 2 and 3 mm particles than in the MEWA results for the modified Tung and Dhir friction model (Figure 20). On the other hand, since in the MEWA simulations, the highest values were obtained with the Reed model (Figure 12, Figure 14, Figure 16 and Figure 18), the MEWA results for the Reed model are also compared with the DECOSIM results in Figure 22 and Figure 23. The agreement is improved and dryout occurs in all cases. Yet, even with the Reed model, cooling in the MEWA simulations is more efficient than in the DECOSIM simulations leading to lower particle temperatures.

There are, however, some inconsistencies between the MEWA and DECOSIM simulation results. The range for the particle temperature distribution in the DECOSIM results is from 381 K (Figure 21) (this does not mean that the temperature in the coldest bed cells is 381 K). In the MEWA simulations the initial bed temperature is set close to the saturation temperature at the cone tip, about 407 K, and no lower temperature is obtained for the bed area. This might cause the time shift in the results seen in Figure 20 and Figure 22. Furthermore, the saturation temperature seems to be different in the MEWA and DECOSIM simulations. In the MEWA simulations, the saturation temperature is a function of the pressure and thus somewhat larger at the bed bottom (c.f., the particle temperature in Figure 21 for the 3 mm particles). In the DECOSIM results, the saturation temperature is about 387 K (Yakush & Kudinov, 2014, Table 1) and thus close to a value which would be obtained, if the top boundary pressure were 1 bar.

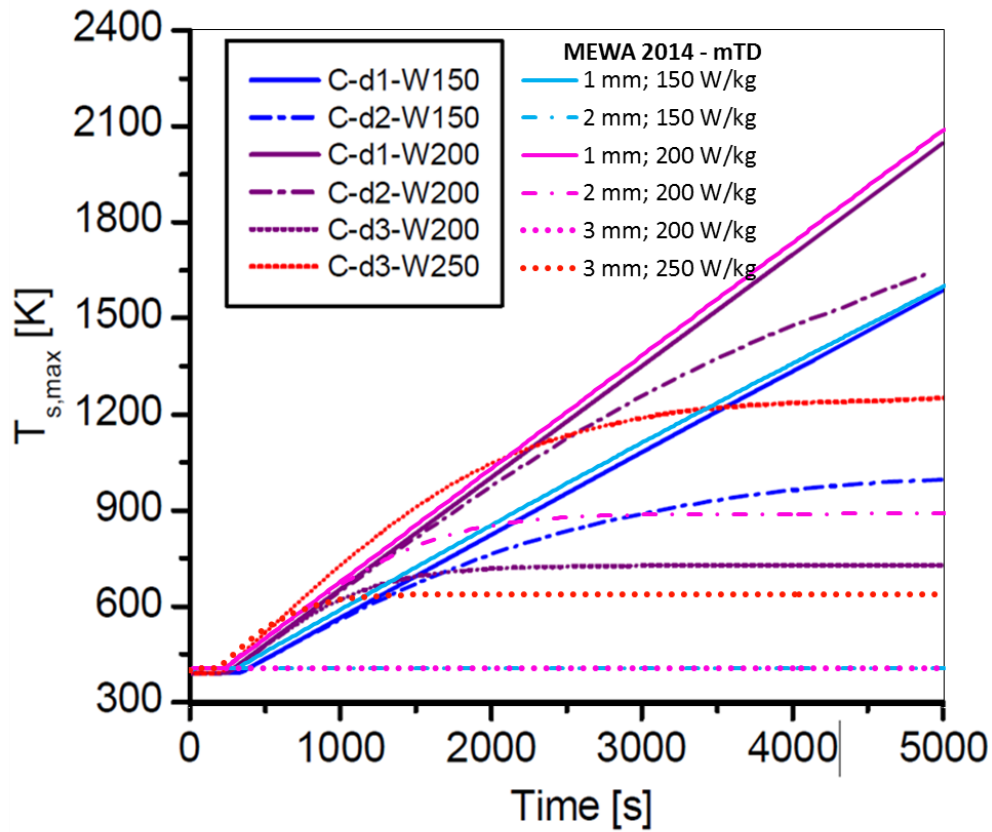


Figure 20. Comparison of the time evolution of the maximum solid particle temperature in the MEWA simulations of this study and in the DECOSIM simulations according to Yakush & Kudinov (2014) (C-d1/2/3-W150/200/250 curves) for the same conical bed cases. The modified Tung and Dhir friction model of MEWA(2014) was applied in the MEWA simulations. The Schmidt (2007) version of the modified Tung and Dhir model has been used by Yakush & Kudinov (2014).

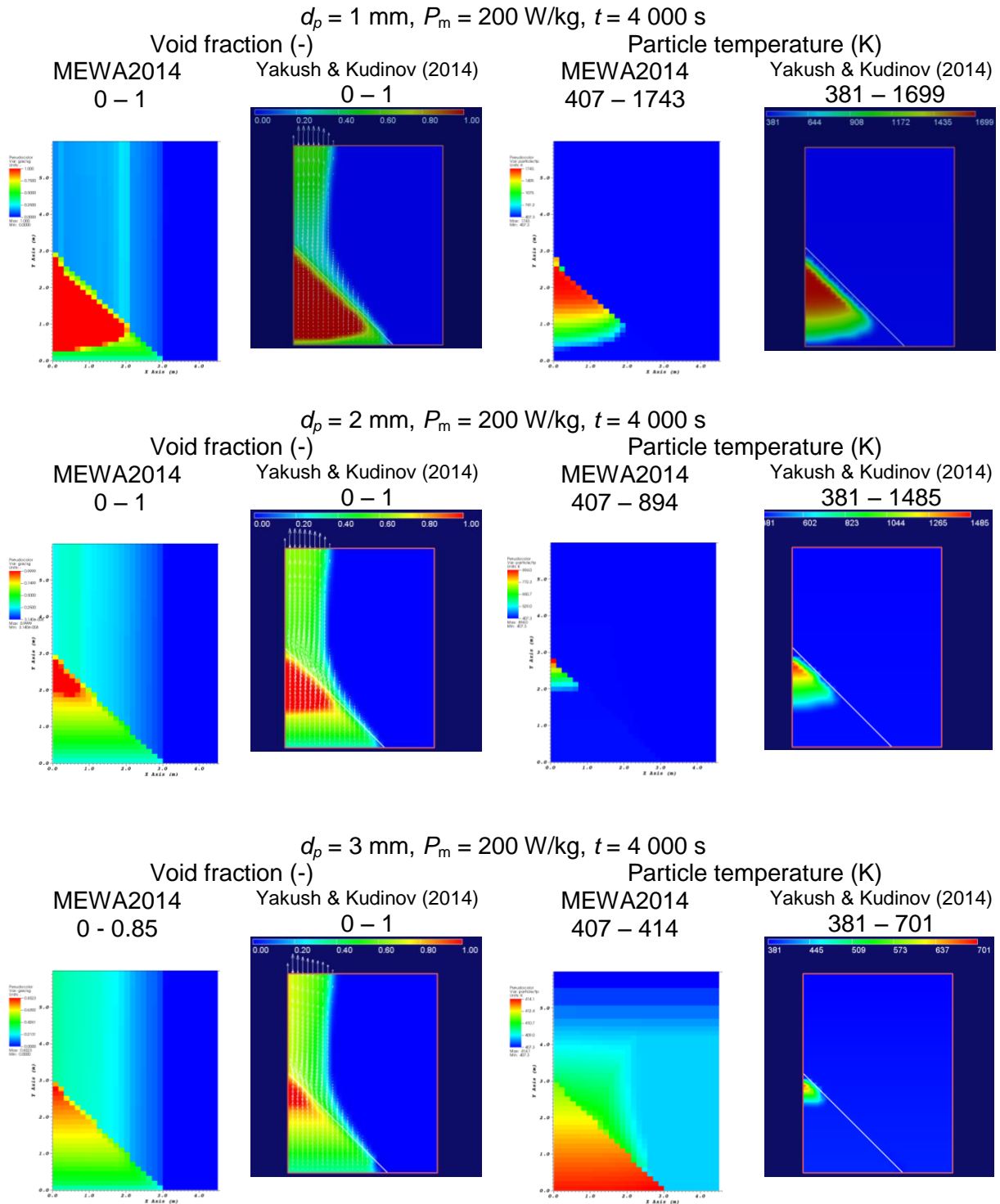


Figure 21. Void fraction (two left columns) and solid particle temperature (two right columns) at the time of 4000 s in the MEWA2014 simulations of this study and in the DECOSIM simulations according to Yakush & Kudinov (2014). The modified Tung and Dhir friction model of MEWA(2014) was applied in the MEWA simulations. The Schmidt (2007) version of the modified Tung and Dhir model was used by Yakush & Kudinov (2014).

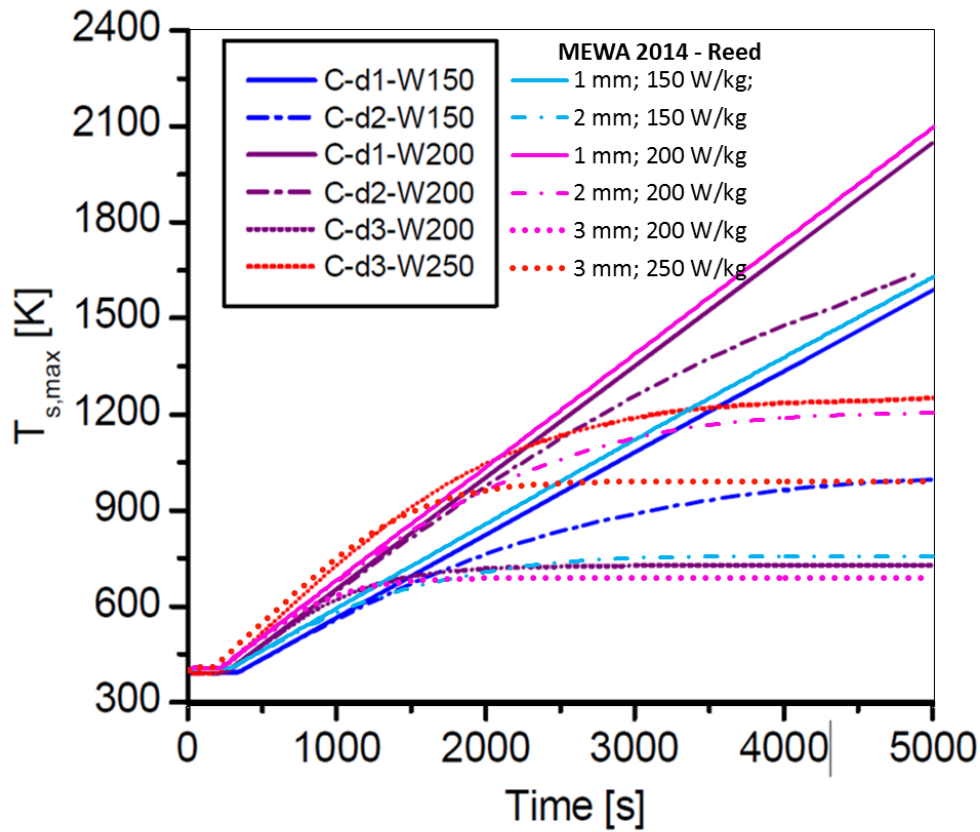


Figure 22. Comparison of the time evolution of the maximum solid particle temperature in the MEWA simulations of this study and in the DECOSIM simulations according to Yakush & Kudinov (2014) (C-d1/2/3-W150/200/250 curves) for the same conical bed cases. The Reed friction model of MEWA(2014) was applied in the MEWA simulations. The Schmidt (2007) version of the modified Tung and Dhir model was used by Yakush & Kudinov (2014).

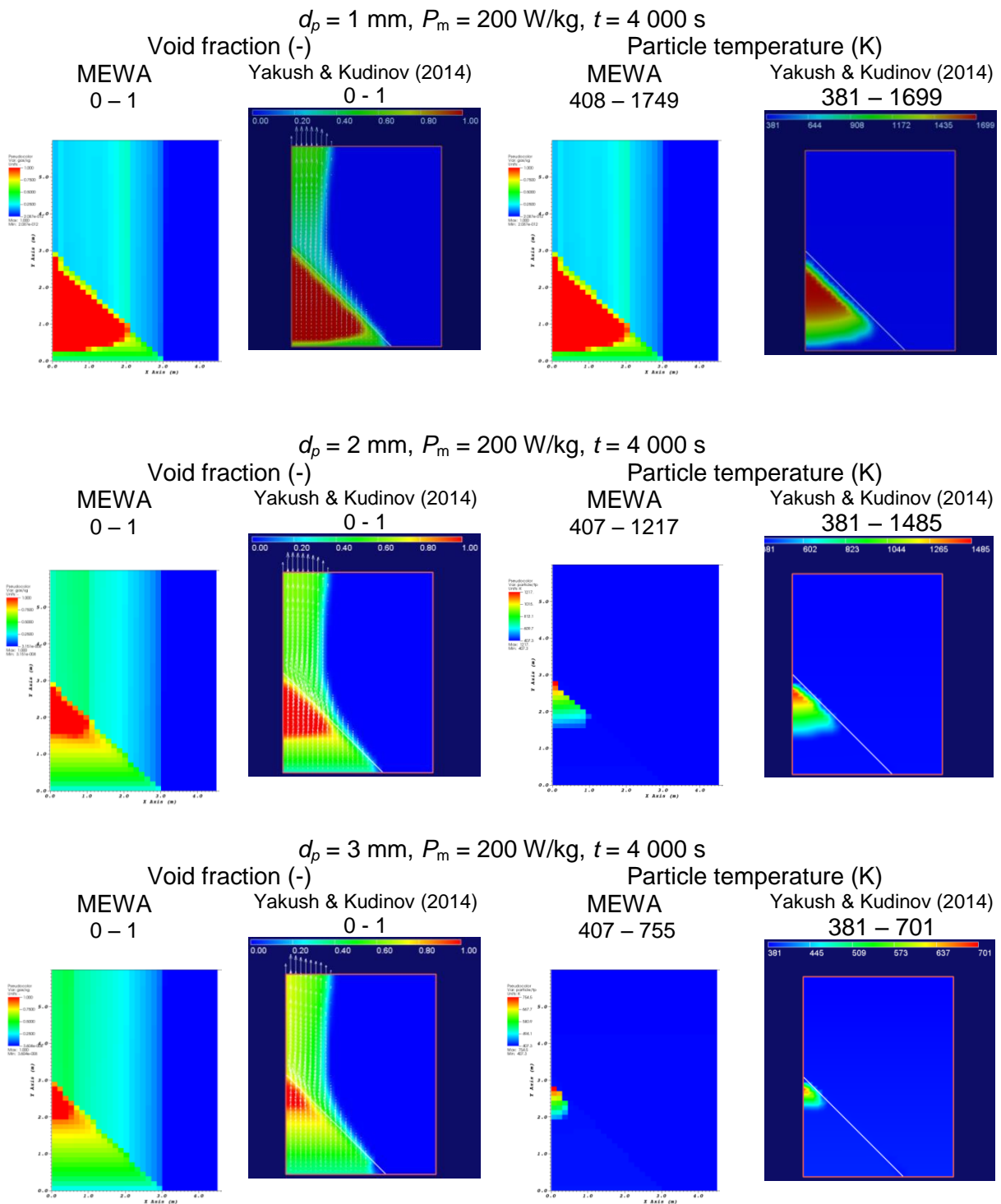


Figure 23. Void fraction (two left columns) and solid particle temperature (two right columns) at the time of 4000 s in the MEWA2014 simulations of this study and in the DECOSIM simulations according to Yakush & Kudinov (2014). The Reed friction model of MEWA(2014) was applied in the MEWA simulations. The Schmidt (2007) version of the modified Tung and Dhir model was used by Yakush & Kudinov (2014).

3.6 Discussion

MEWA simulations were performed for the conical debris bed cases studied at KTH (Yakush & Kudinov, 2014) applying four of the different friction models available in MEWA, the Lipinski, Reed, Tung and Dhir as well as modified Tung and Dhir model. For the 1 mm simulation cases, the influence of cooling is very small after dryout and the maximum particle temperature does not stabilize but increases with a heating-power specific rate. In the cases of 2 and 3 mm particles, the friction model affects strongly the MEWA simulation results. The steady-state conditions are obtained in 1000 – 4000 s except in one case, in which a somewhat longer time is needed. The maximum particle temperature stabilises to values which depend on the particle size, heating power and friction model. For every combination of the particle size and heating power, the highest maximum temperatures are obtained with the Reed friction model. On the other hand, with the Tung and Dhir model and modified Tung and Dhir model, dryout does not occur in all cases. The friction model selection influences also on the area of the dry zone. The computational predictions for the post-dryout conditions are thus influenced significantly by the friction model. Therefore, before trying to quantify a temperature-based coolability criterion, it would be most important to be able to select a friction model which is valid or at least conservative in the post-dryout conditions.

The comparison of the MEWA and DECOSIM results brought out some significant differences in the predictions of the post-dryout conditions. The differences are even largest in those conditions which would be used to determine the temperature-based coolability limit. The MEWA simulation results for any of the friction model models do not agree with the DECOSIM results reported by Yakush & Kudinov (2014). This applies also the modified Tung and Dhir friction model, which is not surprising, since the Schmidt version of the modified Tung and Dhir model (Schmidt, 2007) is very different compared to the present MEWA version of the modified Tung and Dhir model and, on the other hand, the MEWA simulations proved an important role of the friction model.

In some cases, the size of the dry zone and especially its height is only a couple cells because of the coarseness of the mesh (e.g., Figure 16 - Figure 19). Although the stabilized particle temperature is hundreds degrees above the saturation temperature, conclusions must be made with care in these cases.

There are also some other differences between the MEWA and DECOSIM simulations but the influence of the friction model is most likely dominating. Simulations with the same friction model used in the DECOSIM simulations are thus essential.

4. CFD-based analyses

4.1 Background

A CFD-based simulation framework applicable in debris bed coolability studies was developed at VTT (Takasuo et al., 2015). Debris-bed specific models were implemented into Fluent's multiphase flow solver as user defined functions (Ansys 2015a, 2015b, 2015c). The closure models for heat transfer and friction forces are the same as in MEWA (version 2014). The full Eulerian-Eulerian multiphase conservation equations can be solved either in axisymmetric or 3D coordinate systems.

In this study, the Fluent implementation was developed further. As the friction model was found important in predicting the bed behaviour in the post-dryout conditions and MEWA does not feature the Schmidt version (Schmidt, 2007) of the modified Tung and Dhir friction model but it was applied in the DECOSIM simulations at KTH (Yakush & Kudinov, 2014), the Schmidt version was implemented into the CFD-based modelling framework. Since the Fluent implementation has been used and verified mainly for conditions preceding dryout (Takasuo et al., 2015), the Fluent-implemented analysis tool was first verified comparing results with the MEWA results in the post-dryout conditions.

4.2 CFD-based analysis framework

4.2.1 Conversation equations

CFD-based simulation tool developed for computational analyses of the debris bed behaviour is based on solving the multi-dimensional Eulerian-Eulerian conservation equations for the mass, momentum and energy of the gas and liquid phases.

In multiphase flows, the mass conservation equation is

$$\frac{\partial}{\partial t}(\varepsilon\alpha_i\rho_i) + \nabla \cdot (\varepsilon\alpha_i\rho_i\vec{v}_i) = (-1)^{(1+\delta_{ig})}\Gamma \quad (30)$$

The full momentum balance equation in multiphase flows can be written as follows

$$\begin{aligned} \frac{\partial}{\partial t}(\varepsilon\alpha_i\rho_i\vec{v}_i) + \nabla \cdot (\varepsilon\alpha_i\rho_i\vec{v}_i\vec{v}_i) \\ = -\varepsilon\alpha_i\nabla p_i + \varepsilon\alpha_i\rho_i\vec{g} + \nabla \cdot (\varepsilon\alpha_i\vec{\tau}_i) - \vec{F}_{s,i} + (-1)^{(1+\delta_{ig})}\vec{F}_i \end{aligned} \quad (31)$$

The energy conservation equation for the Eulerian fluid phases is

$$\frac{\partial}{\partial t}(\varepsilon\alpha_i\rho_i h_i) + \nabla \cdot (\varepsilon\alpha_i\rho_i\vec{v}_i h_i) = \nabla \cdot (\lambda_{i,eff}\nabla T_i) + Q_{s,i} + (-1)^{(1+\delta_{ig})}\Gamma h_{i,sat} \quad (32)$$

Energy conservation is also used to calculate the temperature of the solid particles from the following equation

$$\frac{\partial}{\partial t}((1-\varepsilon)\rho_s h_s) = \nabla \cdot (\lambda_{s,eff}\nabla T_s) + Q_{s,decay} - Q_{s,sat} - Q_{s,g} - Q_{s,l} \quad (33)$$

The notation is mainly discussed with Equations (1) – (5). $\vec{\tau}_i$ in Equation (31) is the viscous stress. It should be noted that in the multiphase conservation equations formulated as above the velocity and terms including the velocity (e.g., viscous terms) should be interpreted as Favre-averaged (mass-averaged) quantities and the other terms as Reynolds-averaged

(time-averaged) quantities. The conservation equation for the solid particle temperature is implemented as a balance equation for a user defined scalar.

4.2.2 Schmidt friction model

The drag forces between the solid particles and a fluid phase i , $\vec{F}_{s,i}$ in Equation (31), can be written as consistent with the MEWA formulation

$$\vec{F}_{s,i} = \varepsilon \alpha_i \left(\frac{\varepsilon \alpha_i \mu_i}{K K_{r,i}} \vec{v}_i + \frac{\varepsilon^2 \alpha_i^2 \rho_i}{\eta \eta_{r,i}} |\vec{v}_i| \vec{v}_i \right) \quad (34)$$

The modelling of the permeability and passability follows the common formulation applied also in MEWA (Section 3.2.2). The relative permeability K_r and relative passability η_r are modelled as in MEWA applying friction-model dependent correlations. The Lipinski, Reed, Tung & Dhir as well as the MEWA(2014) version of the modified Tung & Dhir friction models were implemented earlier (Takasuo et al., 2015).

The Schmidt version of the modified Tung and Dhir model (Schmidt, 2007), the Schmidt model, was added into the Fluent implementation. The flow regime map for the Schmidt model is shown in Figure 24. In the range of 1 – 3 mm particles, the flow is mostly either annular or in the transition from slug flow to annular flow. There are thus significant differences compared to the Tung and Dhir model and the modified Tung and Dhir model in MEWA (Figure 4). For the relative permeability and relative passability, the formulas of the Tung and Dhir model are used as such for the bubbly and slug flows as well as for the annular flows (Equations (12) and (13)). However, Schmidt (2007) does not consider the transition region between the slug flow and annular flow regimes. In this work, the same interpolation formula as with other models is applied.

In addition, Schmidt (2007) modified the interfacial drag term \vec{F}_i to increase the capability of the model to predict dryout heat flux in both the top and bottom flooding conditions. In the annular flow regime, the interfacial drag force \vec{F}_i is calculated from the following formula

$$\vec{F}_i = \left[\frac{\varepsilon \alpha_l \mu_g}{K K_{r,g}} \vec{v}_r + \frac{\varepsilon^2 \alpha_l \alpha_g \rho_g}{\eta \eta_{r,g}} |\vec{v}_l| \vec{v}_l \right] \alpha_l^2 \cdot \text{MIN} \left[1, \left(\frac{d_p}{0.006\text{m}} \right)^2 \right] \quad (35)$$

In the other flow regimes, the formulations of the Tung and Dhir model in Table 4 are applied.

The bubble diameter is calculated as follows (Schmidt, 2007)

$$d_b = \text{MIN} \left(1.35 \sqrt{\frac{\sigma}{g(\rho_l - \rho_g)}}, 0.41 d_p \right), \quad (36)$$

where σ is the surface tension of water. The diameter of droplets is assumed to be the same as indicated by Schmidt (2007).

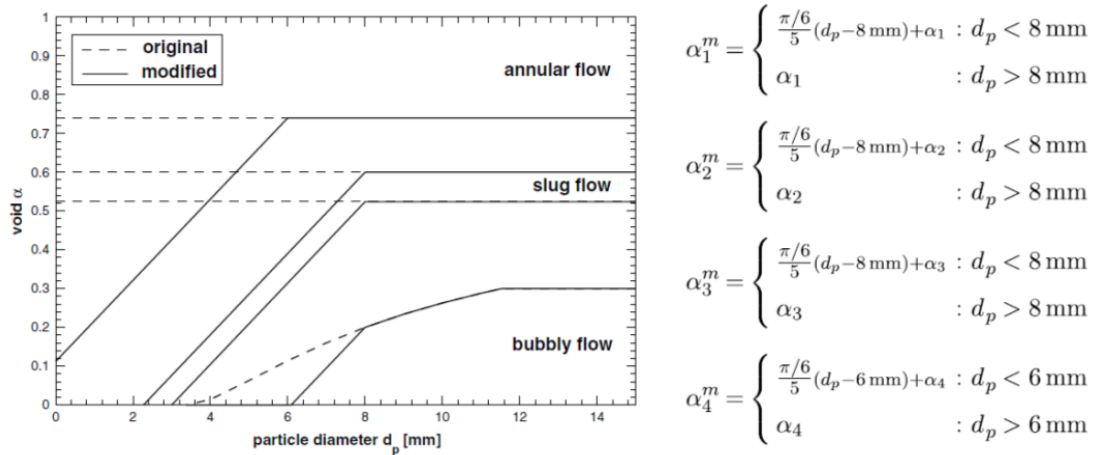


Figure 24. Flow regime map in the Schmidt version of the modified Tung and Dhir model (Schmidt, 2007).

4.3 Verification of the Fluent implementation

In the verification study, the cases computed with MEWA and introduced in Section 3 for the conical particle beds studied at KTH (Yakush & Kudinov, 2014) were recomputed with the CFD-based modelling framework. However, the 1 mm particle case with the high specific power of 200 W/kg was omitted because of a small influence of cooling (Figure 10). In this case, the result of the Fluent implementation would presumably agree with the MEWA results in that case.

4.3.1 Computational cases

Figure 25 shows the computational domain, mesh and actual shape of the particle bed and compares to those used in the MEWA simulations discussed in Section 3. The cells assigned to represent the particle bed define the actual shape of the bed studied computationally. The computational domains, meshes and actual particle bed shapes are identical to those in the MEWA simulations.

Problems are expected to arise from the fact that the mesh is too coarse to be used in CFD simulations. There should be at least several cells for each step on the bed surface. Furthermore, the mesh density close to the tip of the cone is too coarse to reproduce correctly the complicated contracting (and likely swirling) flow field. In Fluent simulations, a body-fitted mesh with a perfect representation of the shape of the conical bed could have been used (as was done in Takasuo et al., 2015). However, the same spatial discretization and actual computational bed shape as used in the MEWA simulations was chosen from comparison point of view. The influence of the mesh density was studied in the study on the influence of computational parameters in Section 4.3.3.

The same properties and models are used as in the MEWA simulations in Section 3. Computations were performed with the Lipinski, Reed as well as Tung and Dhir friction models. A constant time step of 5 ms was used.

Especially in multiphase CFD simulations, numerical parameters potentially effect on results. The numerical parameters were primarily chosen to obtain the same numerical accuracy as in the MEWA simulations. Following numerical parameter were used in the base simulation setup: pressure-based solver, phase-coupled SIMPLE, gradient calculation: Green-Gauss cell-based, spatial discretization scheme: first-order upwind, transient formation: first-order implicit. Influence of the numerical parameters was studied and is discussed in Section 4.3.3.

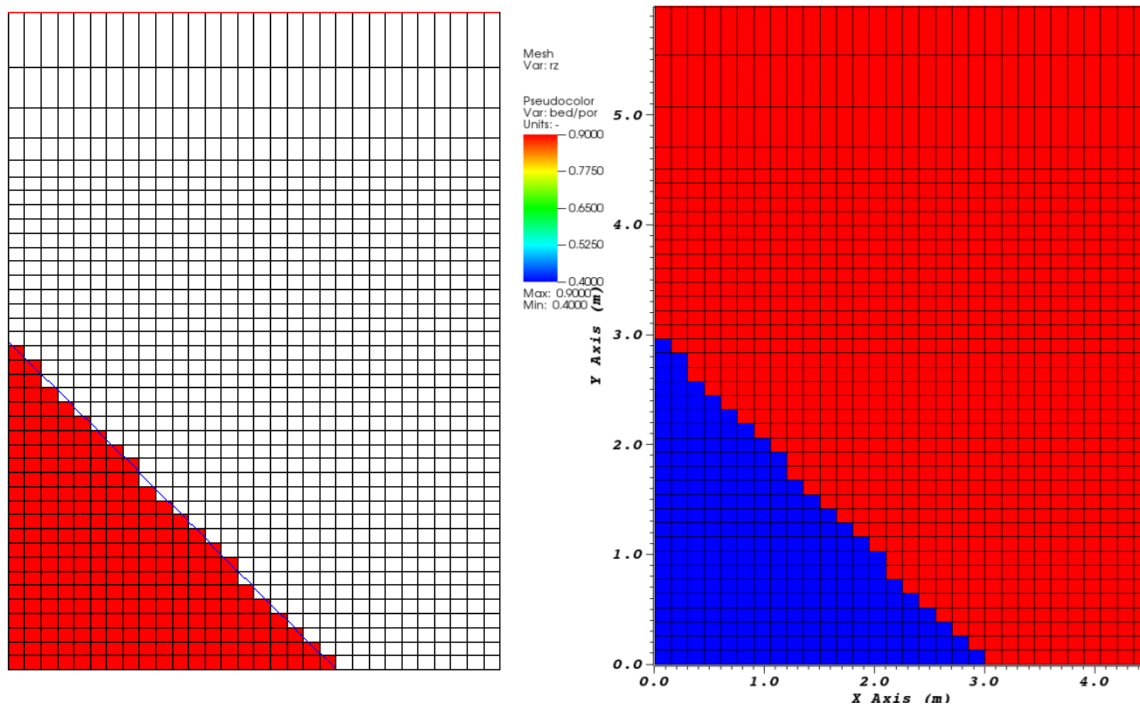


Figure 25. Computational domain, mesh and actual bed shape for the conical particle beds in the Fluent (left) and MEWA (right) simulations. In the left-hand-side plot, the blue line shows the theoretical shape of the conical bed of KTH (Table 1) and the red cells represent the bed in simulations. In the right-hand-side plot, the cells are coloured by the porosity (c.f., Section 3.3).

4.3.2 Comparison of the CFD and MEWA results

The time evolution of the maximum solid particle temperature in the Fluent simulations for the Lipinski friction model is plotted and compared to the MEWA results in Figure 26. The “no cooling” lines indicate how the particles would heat up without any cooling.

In the 1 mm case, the agreement is good. Figure 27 compares distributions of the void fraction and solid particle temperature at the time of about 4000 s to corresponding results in the MEWA simulations. The contour plots are similar except in the bed tip area. Because of the convection and viscous force terms included in the Fluent simulations, in the area of the vertical two-cell step in the bed surface shape close to the bed tip (Figure 25), water penetrates horizontally into the porous bed reducing the height of the dry zone. This does not influence the maximum particle temperature in Figure 26 because fully developed steady-state conditions are not reached and particle temperature is still increasing lower in the bed.

The vertical two-cell step induced penetration of the water flow into the bed close to the bed tip influences also the results for 2 and 3 mm particles shown in Figure 28 and Figure 29. Steady-state conditions are obtained in the Fluent simulations as well as in the MEWA simulations (Figure 26) but the maximum particle temperatures in the Fluent simulations stabilize to lower values than in the MEWA simulations. Differences in the flow patterns and resulting relatively large differences in the area of the dry zone and especially its height can be understood to lead to smaller maximum bed particle temperatures in the Fluent simulations (Figure 26). The significant differences in the 2 mm particle case with the specific power of 200 W/kg (Figure 26 and Figure 28) are also increased by the flow penetration due to another two-cell step lower on the bed surface (Figure 25).

Figure 30, Figure 31, Figure 32 and Figure 33 compare the results of the Fluent-based simulation model to those of MEWA for the Reed friction model. The maximum particle

temperatures especially in steady states are higher but otherwise the distributions, differences and reasons of the differences are mainly similar as in case of the Lipinski model.

The Fluent-implementation results for the Tung and Dhir model are shown and compared to the corresponding MEWA results in Figure 34, Figure 35, Figure 36 and Figure 37. The 1 mm particle results are close to each other consistently with the other friction models. For larger particles, the differences are smaller than with the other friction models. The interfacial force modifies the water flow field and decreases the water penetration into the bed. However, the area of the dry zone is in most cases so small that quantitative comparisons of the maximum particle temperature are questionable. Only for the 2 mm particles with the specific heating power of 200 W/kg, the dry zone is reasonably high (Figure 36).

The influence of the friction model on the time evolution of the maximum particle temperature in the MEWA simulations and on the other hand in the Fluent simulations is compared in Figure 38. The friction model affects qualitatively similarly in both the simulation tools.

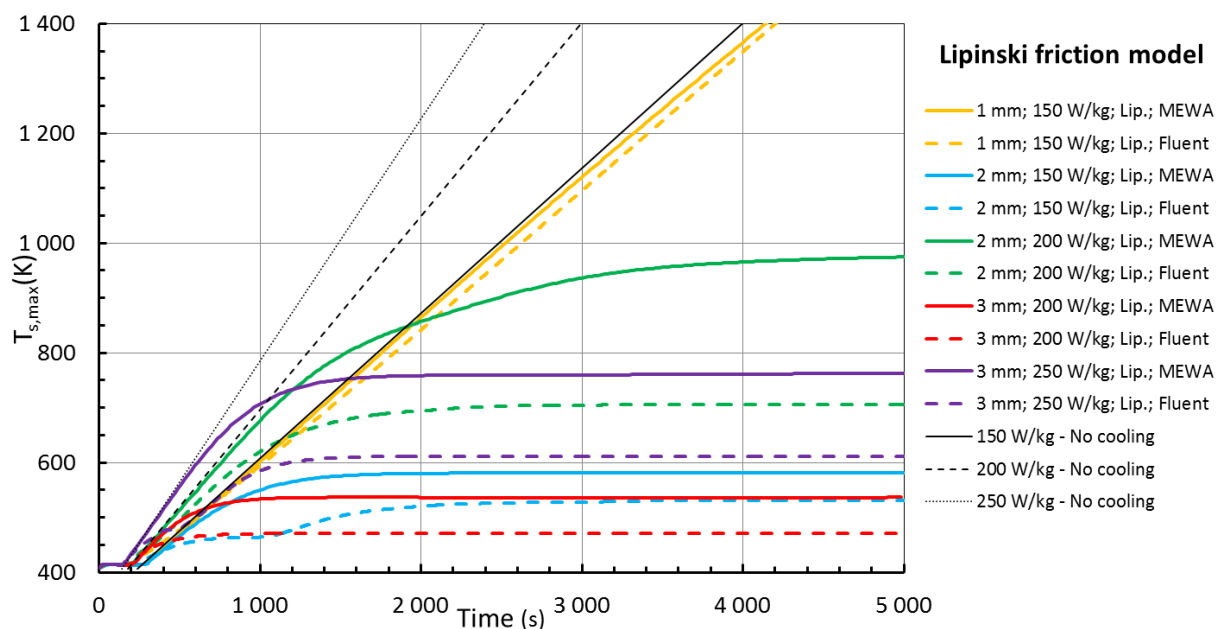


Figure 26. Comparison of the time evolution of the maximum solid particle temperature in the Fluent and MEWA simulations for conical beds studied by Yakush & Kudinov (2014). The Lipinski friction model was applied. The “no cooling” lines for the particle temperature without any cooling.

$$d_p = 1 \text{ mm}, P_m = 150 \text{ W/kg}, t = 4000 \text{ s}$$

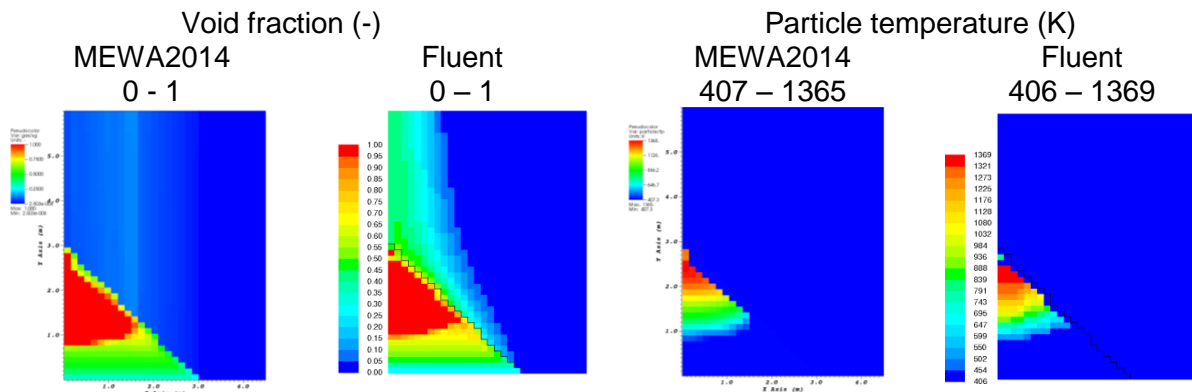
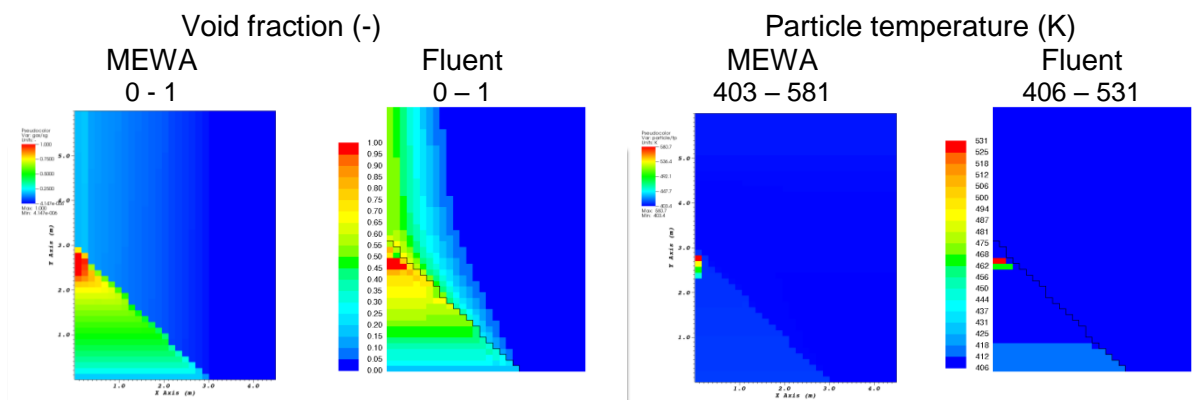


Figure 27. Void fraction (two left columns) and solid particle temperature (two right columns) at the time of 4000 s in the MEWA and Fluent simulations for the conical bed of the 1 mm particles and 150 W/kg specific power studied by Yakush & Kudinov (2014). The Lipinski friction model was applied.

$$d_p = 2 \text{ mm}, P_m = 150 \text{ W/kg}, t = 4000 \text{ s}$$



$$d_p = 2 \text{ mm}, P_m = 200 \text{ W/kg}, t = 4000 \text{ s}$$

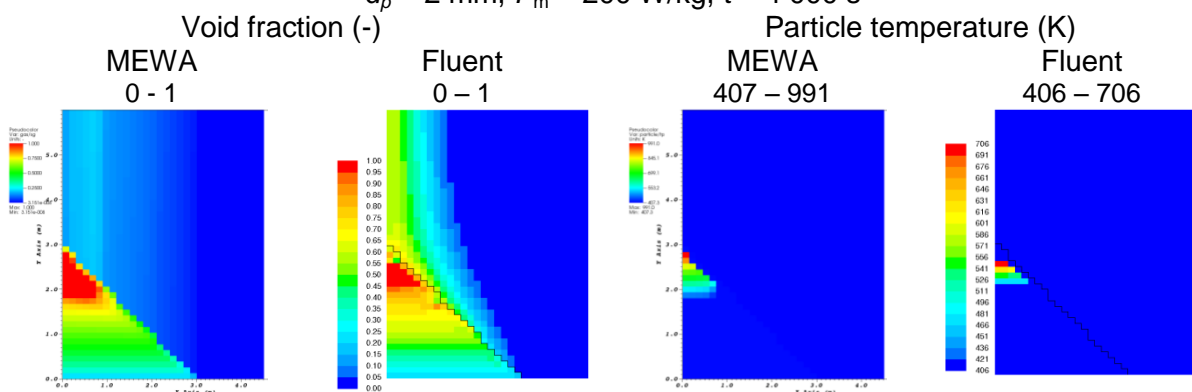
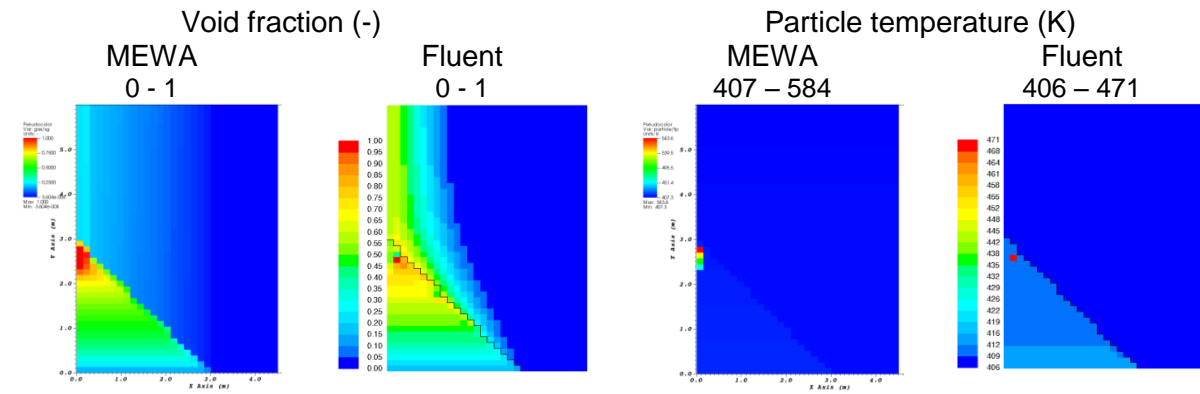


Figure 28. Void fraction (two left columns) and solid particle temperature (two right columns) at the time of 4000 s in the MEWA and Fluent simulations for the conical beds of the 2 mm particles and specific power equal to 150 and 200 W/kg studied by Yakush & Kudinov (2014). The Lipinski friction model was applied.

$$d_p = 3 \text{ mm}, P_m = 200 \text{ W/kg}, t = 4000 \text{ s}$$



$$d_p = 3 \text{ mm}, P_m = 250 \text{ W/kg}, t = 4000 \text{ s}$$

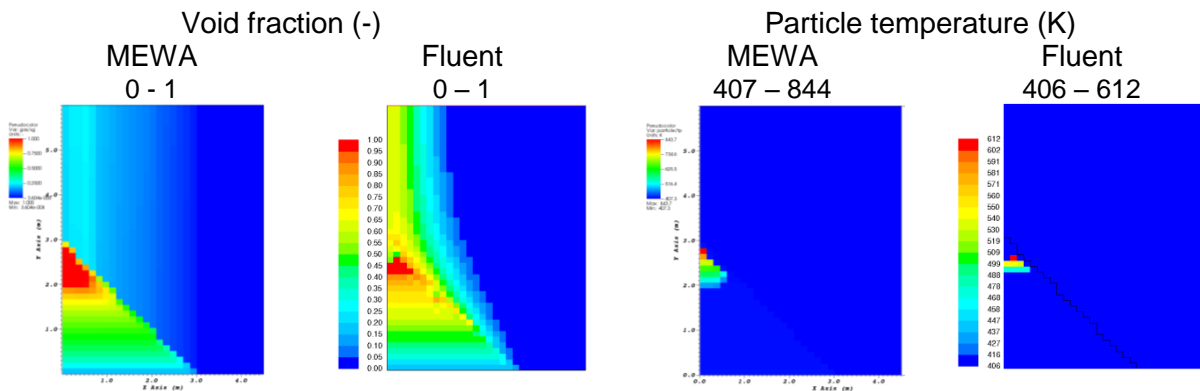


Figure 29. Void fraction (two left columns) and solid particle temperature (two right columns) at the time of 4000 s in the MEWA and Fluent simulations for the conical beds of the 3 mm particles and specific power equal to 200 and 250 W/kg studied by Yakush & Kudinov (2014) The Lipinski friction model was applied.

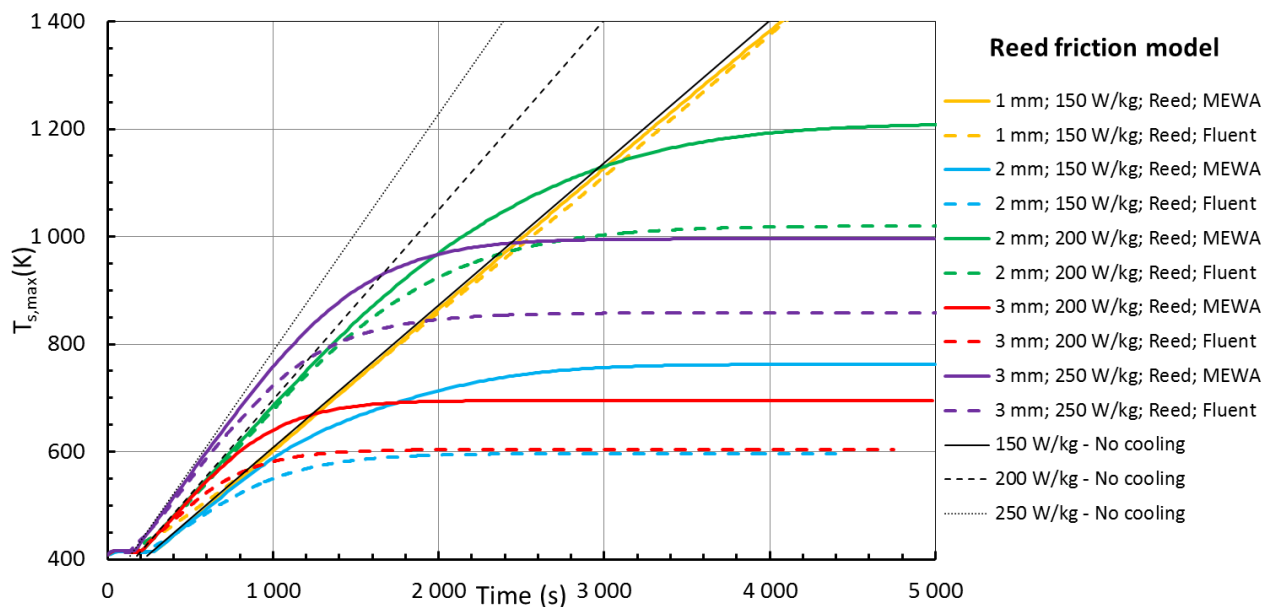


Figure 30. Comparison of the time evolution of the maximum solid particle temperature in the Fluent and MEWA simulations for conical beds studied by Yakush & Kudinov (2014). The Reed friction model was applied. The “no cooling” lines for the particle temperature without any cooling.

$$d_p = 1 \text{ mm}, P_m = 150 \text{ W/kg}, t = 4000 \text{ s}$$

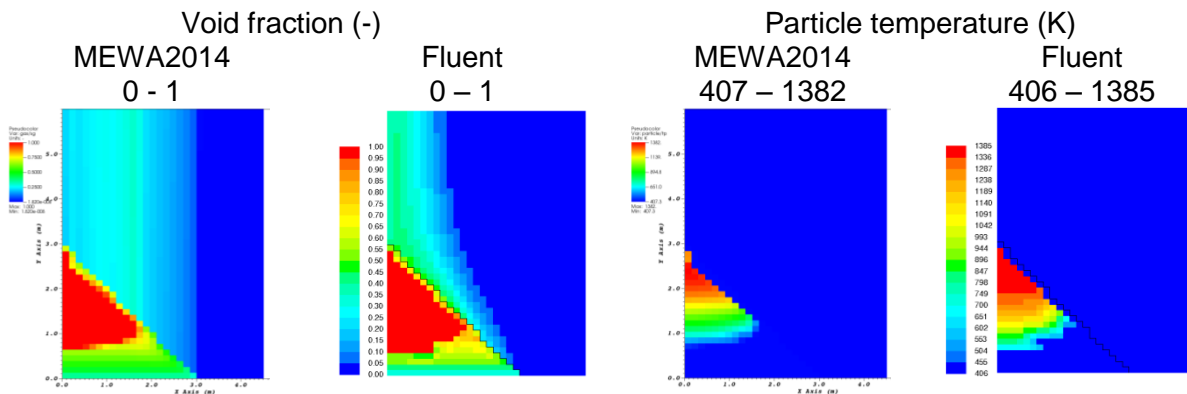
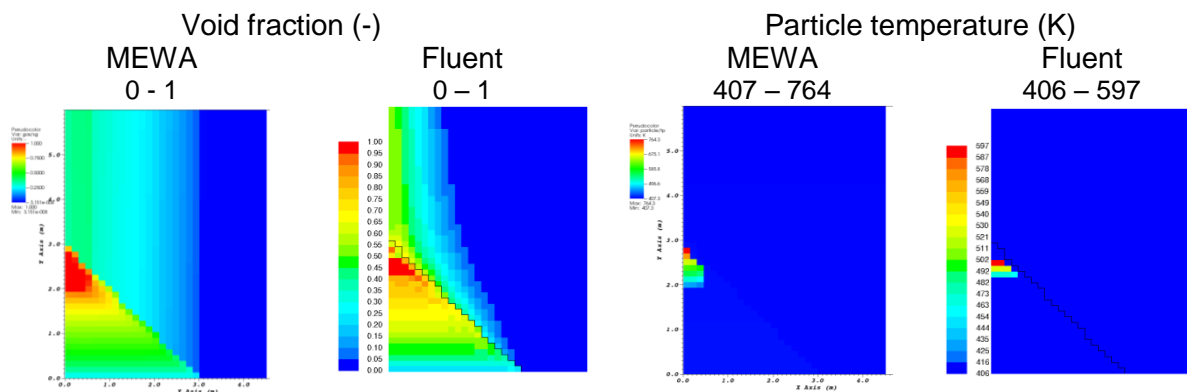


Figure 31. Void fraction (two left columns) and solid particle temperature (two right columns) at the time of 4000 s in the MEWA and Fluent simulations for the conical bed of the 1 mm particles and 150 W/kg specific power studied by Yakush & Kudinov (2014). The Reed friction model was applied.

$$d_p = 2 \text{ mm}, P_m = 150 \text{ W/kg}, t = 4000 \text{ s}$$



$$d_p = 2 \text{ mm}, P_m = 200 \text{ W/kg}, t = 4000 \text{ s}$$

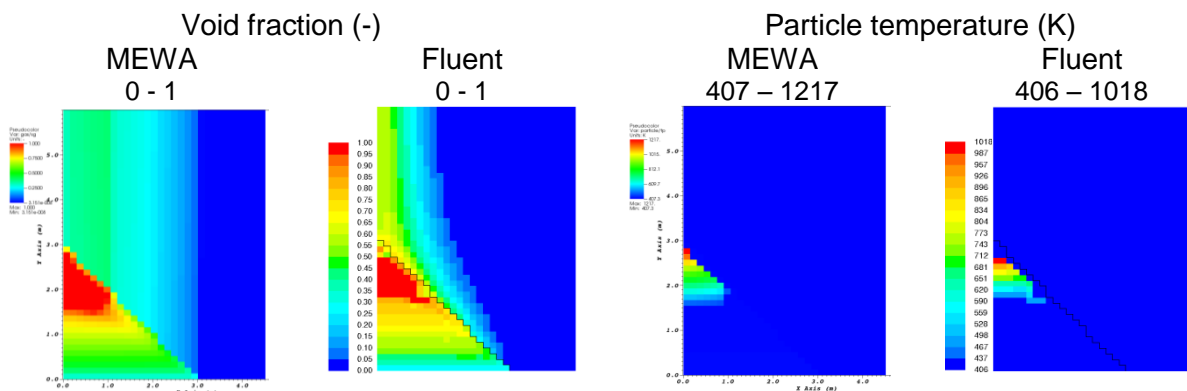


Figure 32. Void fraction (two left columns) and solid particle temperature (two right columns) at the time of 4000 s in the MEWA and Fluent simulations for the conical beds of the 2 mm particles and specific power equal to 150 and 200 W/kg studied by Yakush & Kudinov (2014). The Reed friction model was applied.

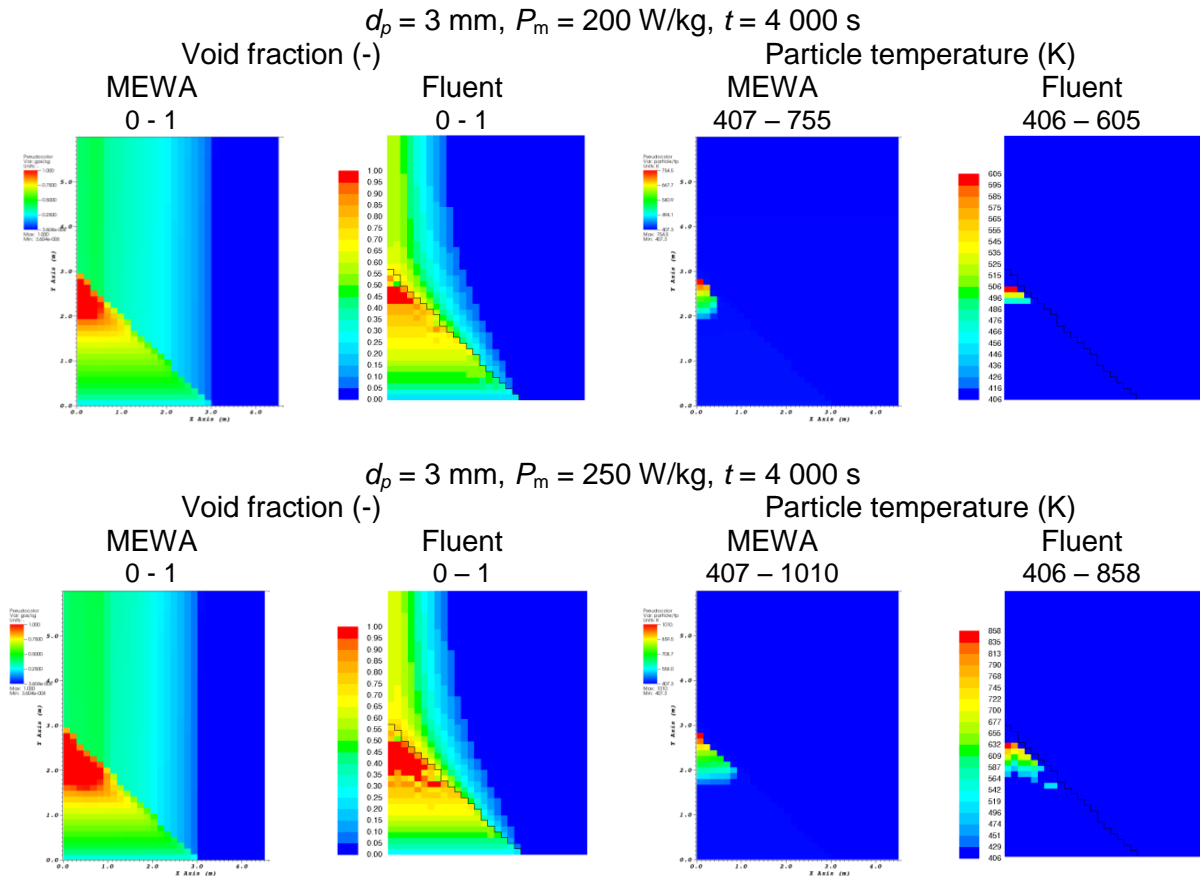


Figure 33. Void fraction (two left columns) and solid particle temperature (two right columns) at the time of 4000 s in the MEWA and Fluent simulations for the conical beds of the 3 mm particles and specific power equal to 200 and 250 W/kg studied by Yakush & Kudinov (2014). The Reed friction model was applied.

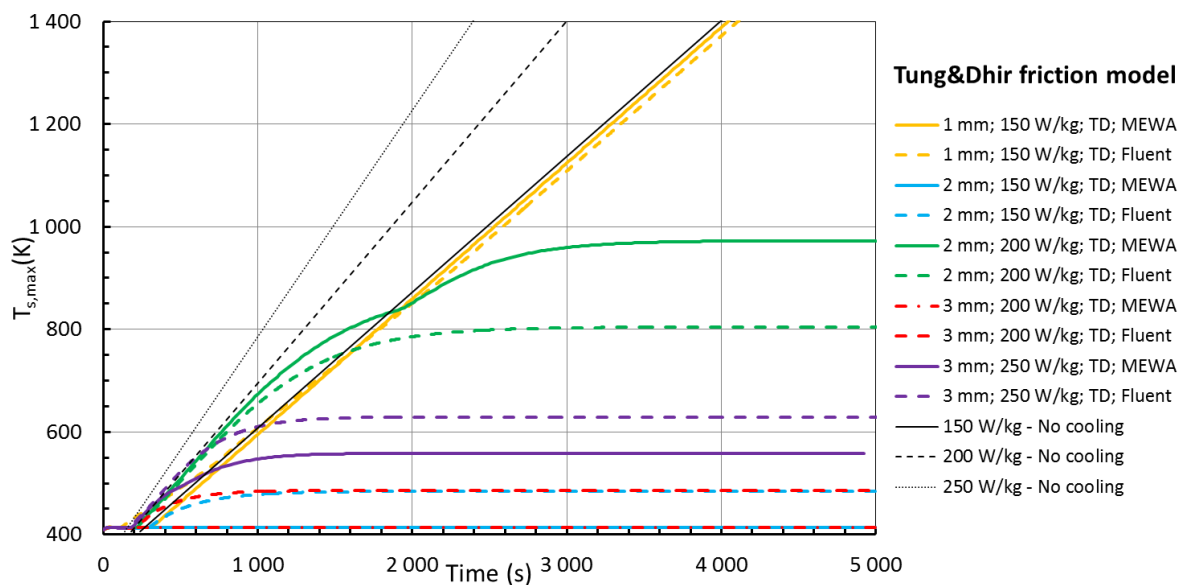


Figure 34. Comparison of the time evolution of the maximum solid particle temperature in the Fluent and MEWA simulations for conical beds studied by Yakush & Kudinov (2014). The Tung and Dhir friction model of MEWA2014 was applied. The “no cooling” lines for the particle temperature without any cooling.

$$d_p = 1 \text{ mm}, P_m = 150 \text{ W/kg}, t = 4000 \text{ s}$$

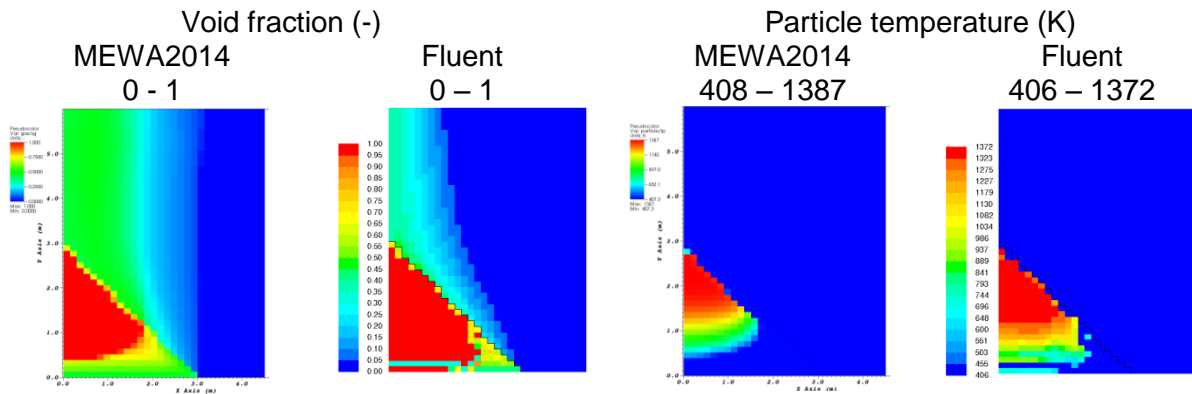
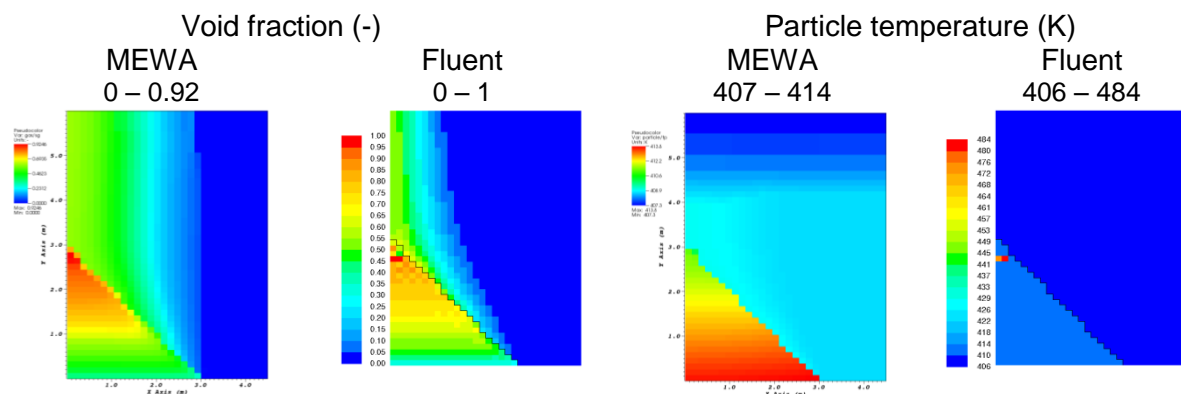


Figure 35. Void fraction (two left columns) and solid particle temperature (two right columns) at the time of 4000 s in the MEWA and Fluent simulations for the conical bed of the 1 mm particles and 150 W/kg specific power studied by Yakush & Kudinov (2014). The Tung and Dhir friction model was applied.

$$d_p = 2 \text{ mm}, P_m = 150 \text{ W/kg}, t = 4000 \text{ s}$$



$$d_p = 2 \text{ mm}, P_m = 200 \text{ W/kg}, t = 4000 \text{ s}$$

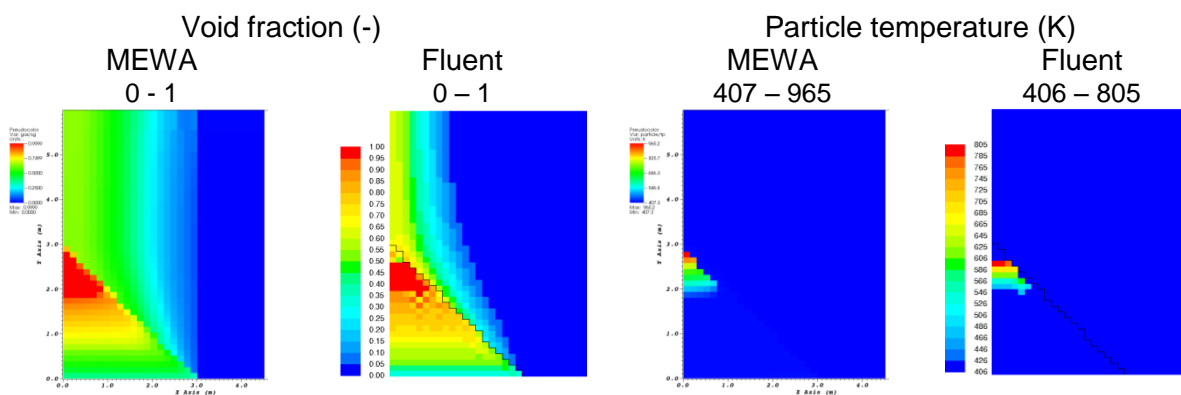
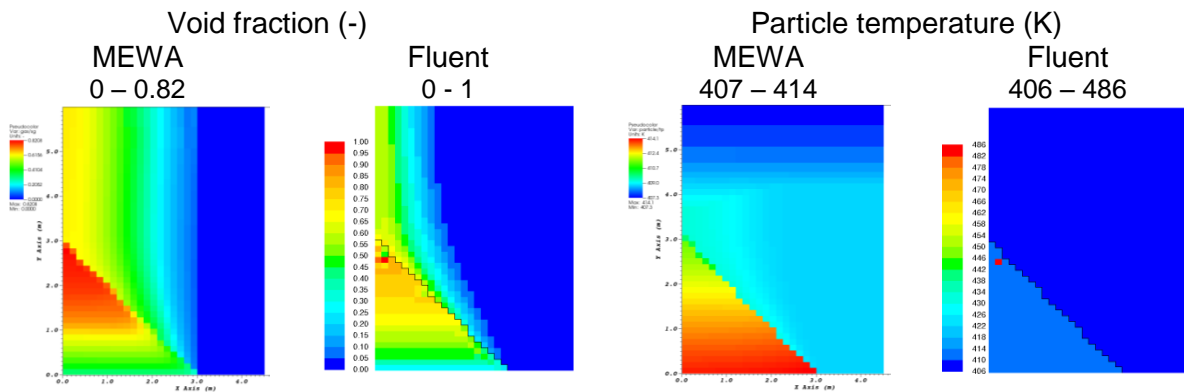


Figure 36. Void fraction (two left columns) and solid particle temperature (two right columns) at the time of 4000 s in the MEWA and Fluent simulations for the conical beds of the 2 mm particles and specific power equal to 150 and 200 W/kg studied by Yakush & Kudinov (2014). The Tung and Dhir friction model was applied.

$$d_p = 3 \text{ mm}, P_m = 200 \text{ W/kg}, t = 4000 \text{ s}$$



$$d_p = 3 \text{ mm}, P_m = 250 \text{ W/kg}, t = 4000 \text{ s}$$

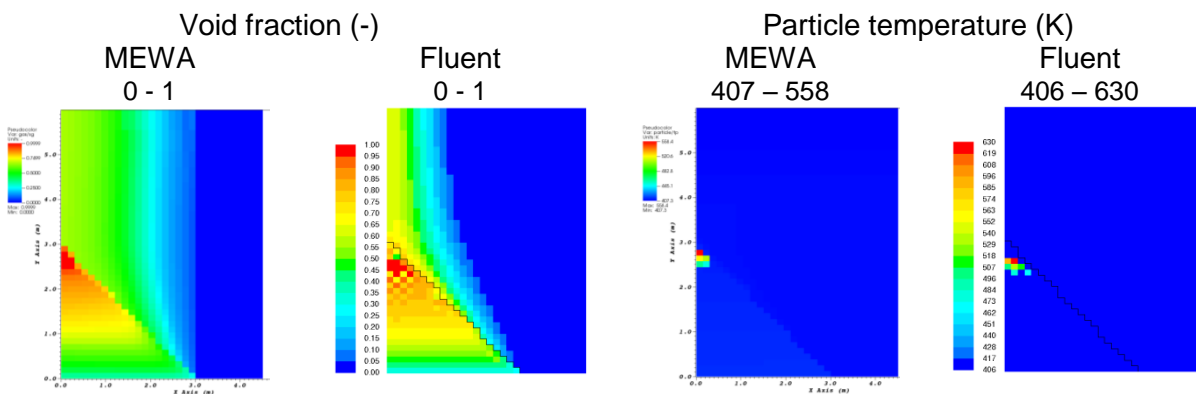


Figure 37. Void fraction (two left columns) and solid particle temperature (two right columns) at the time of 4000 s in the MEWA and Fluent simulations for the conical beds of the 3 mm particles and specific power equal to 200 and 250 W/kg studied by Yakush & Kudinov (2014). The Tung and Dhir friction model was applied.

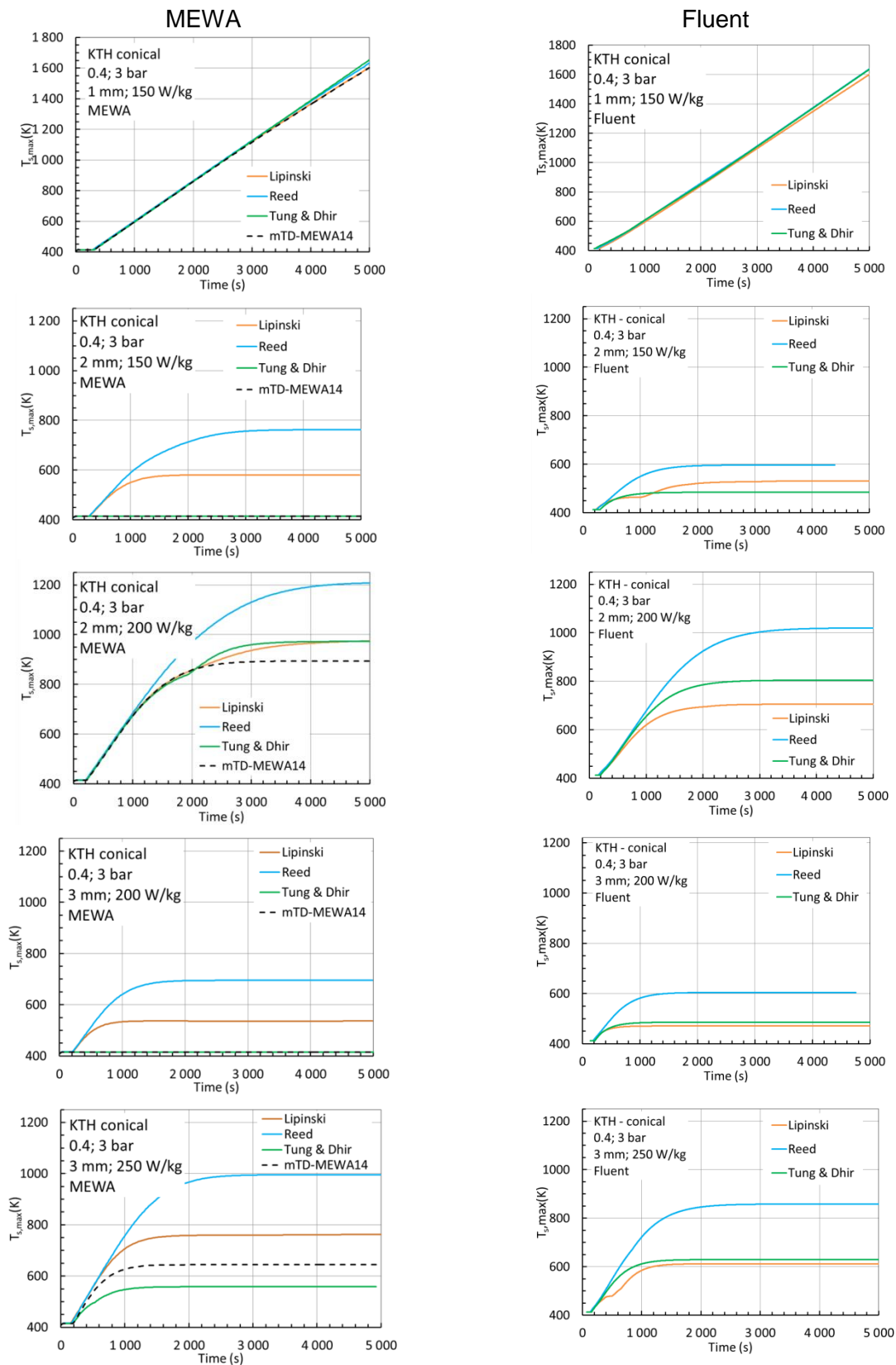


Figure 38. Comparison of the time evolution of the maximum solid particle temperature in the MEWA (left) and Fluent (right) simulations for the conical beds studied by Yakush & Kudinov (2014). mTD-MEWA14 means the modified Tung and Dhir friction model in the MEWA version 2014.

4.3.3 Influence of computational parameters

Influence of some computational parameters including the spatial discretization on the bed behaviour in post-dryout conditions in the Fluent simulations was examined for the case of 3 mm particles and the specific power equal to 250 W/kg. The Reed friction model was applied. The base-case results are thus presented in Figure 30 and Figure 33.

4.3.3.1 Time step

The influence of the time step might be significant especially in the multiphase simulations. A too long time step can ruin the numerical accuracy.

The effect of the time step in the Fluent simulations was examined by reducing the time step from the base-case value of 5 ms to 1 ms. The computed time evolutions of the maximum solid particle temperature for the both time steps are compared in Figure 39. The difference is large and decreasing the time step actually increases the deviation from the MEWA result in Figure 30. On the other hand, differences in the distributions of the void fraction and particle temperature are not that dramatic as shown in Figure 40. The influence of the time step on the contours plots is actually small but not insignificant. The reduced size and especially height of the dry area lead to a smaller maximum particle temperature in the steady state.

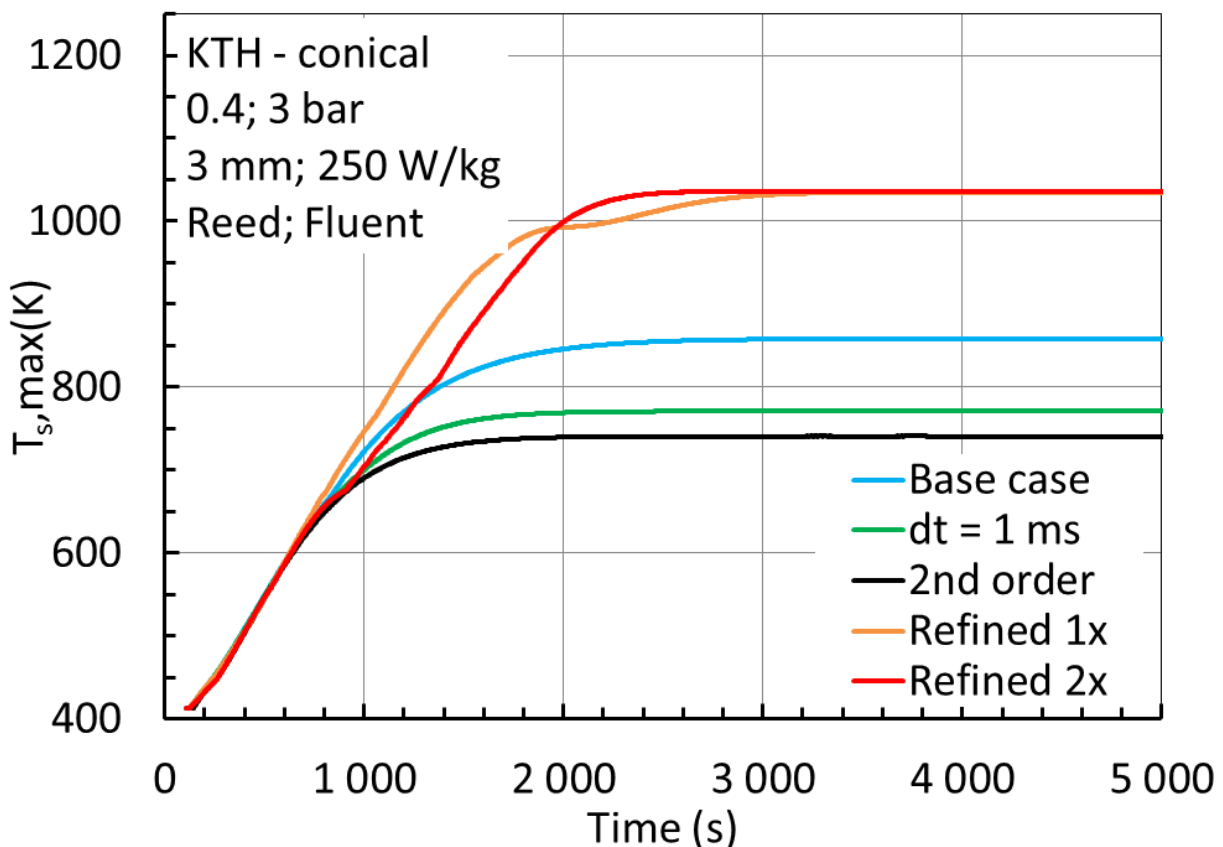


Figure 39. Influence of the time step, spatial discretization scheme and mesh density on the evolution of the maximum solid particle temperature in the Fluent simulations for the conical bed of the 3 mm particles and specific power equal to 250 W/kg. The Reed friction model was applied. Base case: $dt = 5$ ms, 1st order upwind and the original mesh in Figure 42. $dt = 1$ ms: as the base case, but the once refined mesh in in Figure 42. 2nd order: as the base case, but 2nd order upwind for momentum eq. Refined 1x: as the base case, but the once refined mesh in Figure 42. Refined 2x: as the base case, but the twice refined mesh in Figure 42.

Fluent, $d_p = 3$ mm, $P_m = 250$ W/kg, $t = 4\ 000$ s

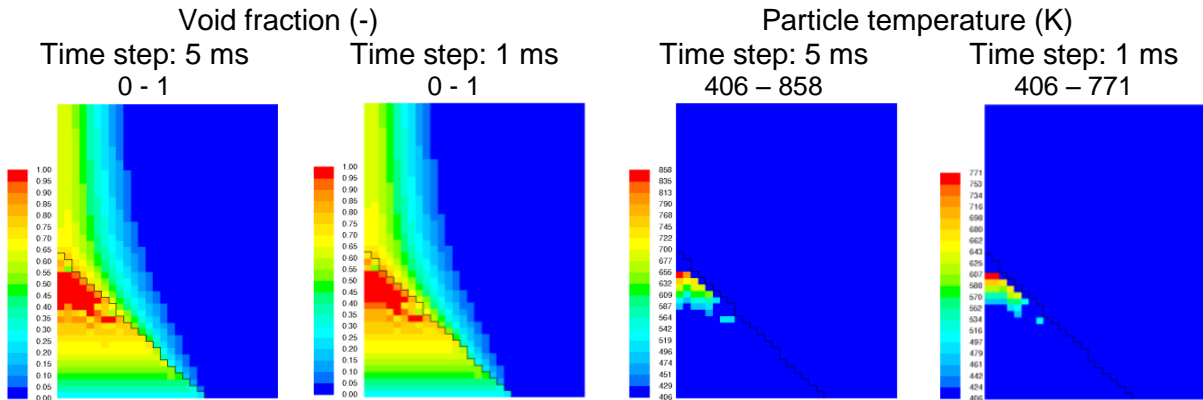


Figure 40. Void fraction (two left columns) and solid particle temperature (two right columns) at the time of 4000 s in the Fluent simulations with the time step equal to 5 ms and 1 ms for the conical bed of the 3 mm particles and specific power equal to 250 W/kg. The Reed friction model was applied.

4.3.3.2 Spatial discretization scheme

In general, the applied spatial discretization scheme of convection terms influences on the results. In the second-order upwind scheme, the face value ϕ_f is calculated as follows (Ansys, 2016a)

$$\phi_f = \phi_c + \nabla\phi_c \cdot \vec{r} \quad (37)$$

where ϕ_c and $\nabla\phi_c$ are the cell-centred value and its gradient, respectively, in the upstream cell and \vec{r} is the vector from the upstream cell to the face centroid. The second-order accuracy should be used especially for the momentum equation on triangular and tetrahedral cells. On the other hand, in the multiphase simulations, improving the numerical accuracy of the convection terms does not necessary improve the final computational results.

The influence of changing from the first-order accuracy to the second-order accuracy in the momentum equation is presented in Figure 38 and Figure 41 for the studied case. The dynamic pressure above the bed tip is higher with the second-order discretization scheme forcing water flow downward along the bed axis. As a result, the dry area is reduced significantly and the maximum particle temperature is lower than in the base simulation case.

With this limited study, it cannot be concluded whether the second-order accuracy improves results. In this case, the mesh is so coarse that the complicated flow field in the bed tip area obtained with the second-order accuracy cannot be predicted reliably. On the other hand, if the complicated flow field were a “correct” solution, the verification of the Fluent implementation by comparison with the MEWA results is not sensible, because MEWA cannot reproduce such a complex flow field.

Fluent, $d_p = 3$ mm, $P_m = 250$ W/kg, $t = 4\ 000$ s

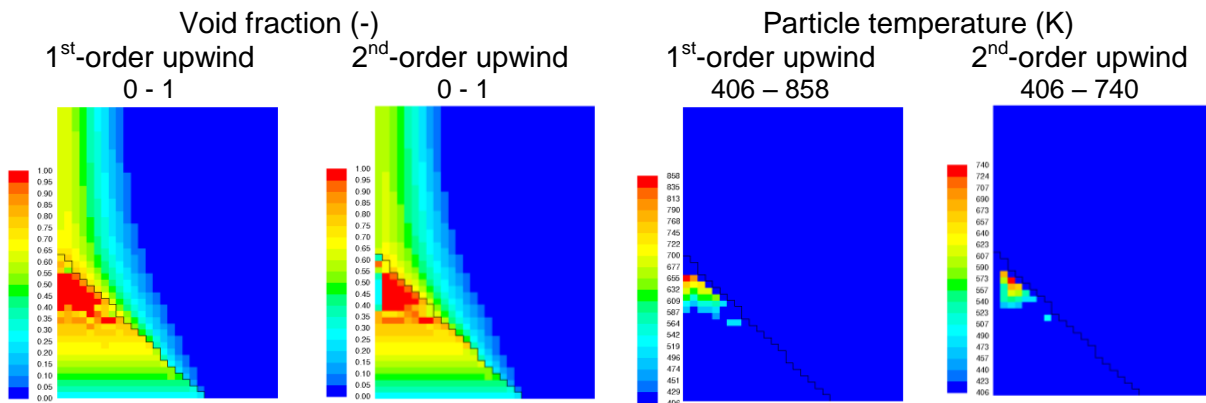


Figure 41. Void fraction (two left columns) and solid particle temperature (two right columns) at the time of 4000 s for the first- and second-order spatial discretization schemes in the momentum equations in the Fluent simulations for the conical bed of the 3 mm particles and specific power equal to 250 W/kg studied by Yakush & Kudinov (2014). The Reed friction model was applied.

4.3.3.3 Spatial discretization

The importance of the mesh density was studied by performing simulations also with meshes in which the bed area was split once and twice horizontally and vertically. The original mesh and the refined meshes with the bed area are depicted in Figure 42. With all meshes, the areas are identical. The time evolutions of the maximum particle temperature are plotted in Figure 39. Figure 42 shows distributions of the void fraction and particle temperature at the time 4000 s from the start of heating. When every cell in the particle bed and close to it is divided into 4 cells, the maximum particle temperature is significantly larger than in the base simulation case. The contour plots show that the dry zone continues up to the bed surface on the bed axis. The maximum particle temperature is even somewhat higher (1035 K) than in the MEWA simulations (1010 K) (c.f., Figure 30 and Figure 33). Further refinement of the mesh does not change the steady-state results significantly, but the time evolution is somewhat different (Figure 39).

4.3.4 Discussion

In the comparison to the MEWA results, large differences are obtained in almost all cases. However, the differences can be interpreted arise from a poor numerical accuracy in solving the full momentum equations with the convective and viscous terms in the coarse base mesh. As the original mesh is not suitable for CFD modelling, refined meshes were applied in Fluent simulations in one case. The results for the refined meshes indicate that the debris-bed models of MEWA are properly implemented in the Fluent implementation. On the other hand, comparing results of two codes with different spatial discretizations is questionable in a verification study.

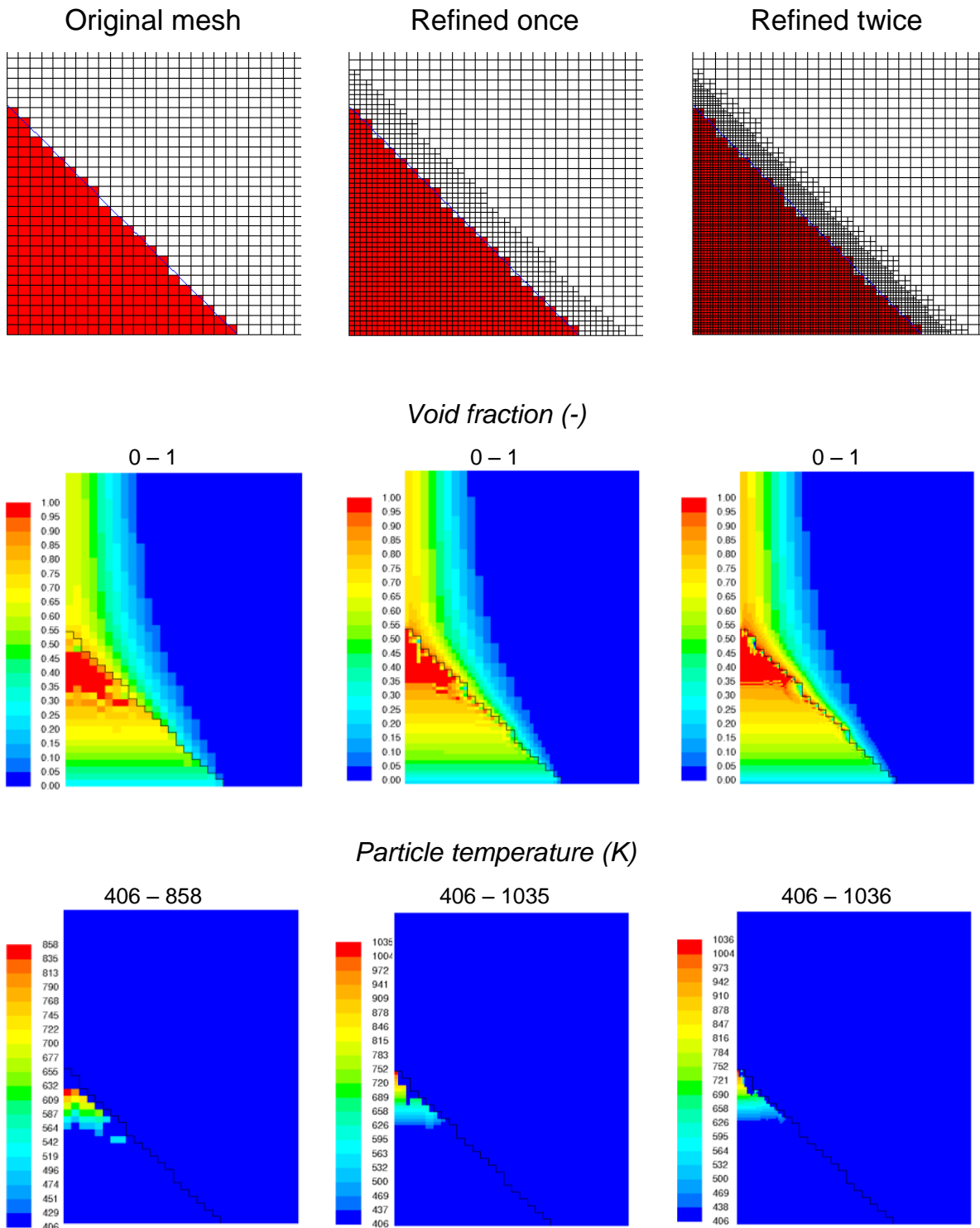


Figure 42. Mesh (top), void fraction (middle) and solid particle temperature (bottom) at the time of 4000 s in the Fluent simulations for the original mesh and for meshes with once and twice split cells in and close to the bed. The conical bed of the 3 mm particles and specific power equal to 250 W/kg studied by Yakush & Kudinov (2014). The Reed friction model was applied.

4.4 Application of the Schmidt model

The conical debris beds studied at KTH (Yakush & Kudinov, 2014) was computed with the CFD-based multiphase simulation framework implemented in Fluent. The objective of this sub-study is to compare the Fluent results to the DECOSIM results of Yakush & Kudinov (2014). Therefore, in addition of applying the same friction model, all the other models and parameters were chosen to be as similar as reasonably possible. The Fluent simulations mimicking the DECOSIM computations were performed for all the same six cases as studied at KTH (Yakush & Kudinov, 2014)

4.4.1 Computational cases

The computational domain, mesh and particle bed are shown in Figure 43. The mesh itself was used in the verification study in Section 4.3. However, the shape of the bed was modified from the one used in the verification study above (Figure 25). The DECOSIM results (Figure 3) indicate that there probably is not a vertical two-cell step in the shape of the bed used in the DECOSIM simulation and it was removed from the bed used in Fluent simulations. In practice, in the two columns next to the axis, the uppermost cells were moved to the pool zone from the bed zone.

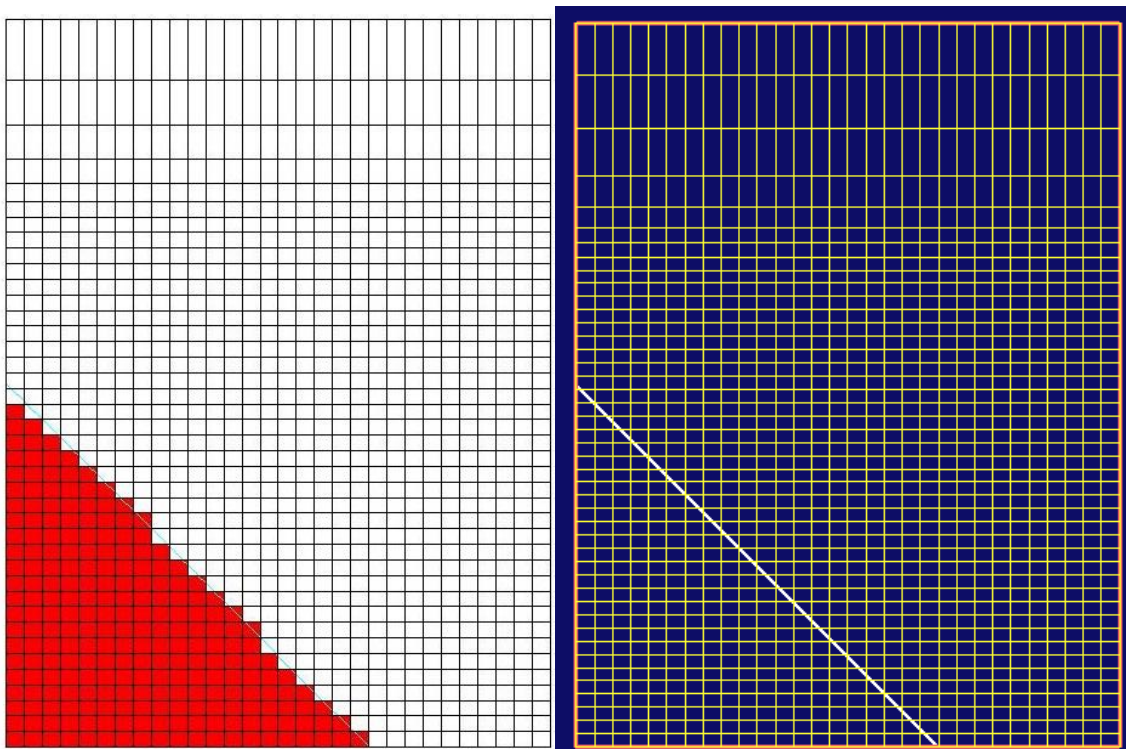


Figure 43. Computational domain, mesh and bed shape in the Fluent simulations (left) for the conical debris beds studied at KTH (Yakush & Kudinov, 2014) and in the DECOSIM simulations of Yakush & Kudinov (2014) (right). In the left-hand-side plot, the blue line shows the theoretical shape of the conical bed of KTH and red cells represent the bed.

The other models and material properties were also chosen to be as consistent as possible with the KTH simulations (Yakush & Kudinov, 2014). Especially, the same model was used for the effective thermal conductivity of the debris bed

$$\lambda_{s,eff} = (1 - \varepsilon)\lambda_s, \quad (38)$$

However, the other heat transfer and boiling models are similar as in MEWA. Numerical parameters are the same as in the verification study in Section 4.3.

4.4.2 Results

The maximum particle temperature is plotted Figure 44 as a function of the simulation time for all the cases studied by Yakush & Kudinov (2014). In the 3 mm cases and in the 2 mm case with the specific power of 150 W/kg, steady states are reached in Fluent simulations in about 2000 s with the case-specific maximum solid particle temperature. The 1 mm particle beds behave as in all simulations with MEWA and Fluent and the maximum particle temperature increases almost as without any cooling (c.f., Figure 34). The 2 mm case with the higher heating power does not fully stabilise in 5000 s and the maximum particle temperature is still increasing slowly.

Figure 45, Figure 46 and Figure 47 show distributions of the void fraction and particle temperature at the time of about 4000 s for 1, 2 and 3 mm particles, respectively. Compared to the results for the same type modified Tung and Dhir friction model in the verification study (Figure 35, Figure 36 and Figure 37), the water flow penetration into the bed is further reduced because of removal the vertical two-cell step from the bed description (c.f., Figure 25 and Figure 43) and possibly because of the differences of the friction models. Yet, because of the convection terms and the viscous forces included in the full multiphase equations, the surface cells and especially the topmost cell do not dry out totally.

As the spatial discretisation was found to influence the computational results in the verification study, the 3 mm particle cases were computed with the refined meshes. The 3 mm particle cases were chosen because steady states are achieved with the larger particle faster. Figure 48 and Figure 49 show the computational refined meshes and bed area as well as the distributions of the void fraction and particle temperature at the time of about 4000 s with the corresponding results for the original mesh. In all the cases the bed areas are identical. In case of the specific power of 200 W/kg, the refinement of the mesh by splitting each cell horizontally and vertically does not modify the steady-state fields strongly and the final maximum particle temperature is almost the same. With the higher heating power, the mesh was refined twice (Figure 49). A complicated steady-state flow field was obtained and the maximum particle temperature decreased to 668 K from the original mesh value of 757 K.

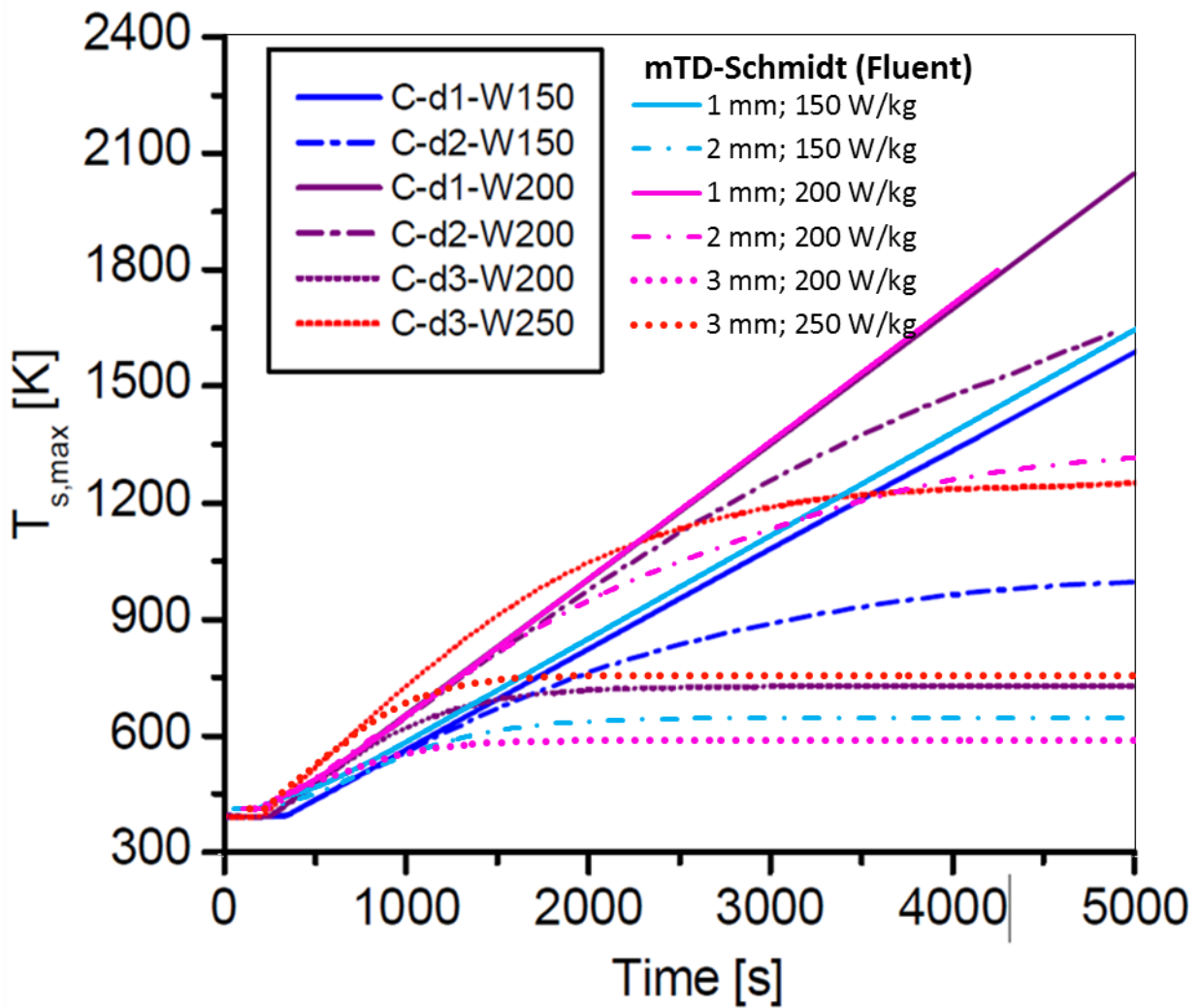


Figure 44. Comparison of the time evolution of the maximum solid particle temperature in the Fluent simulations of this study and in the DECOSIM simulations of Yakush & Kudinov (2014) (C-d1/2/3-W150/200/250 curves) for the same conical bed cases. The Schmidt (2007) version of the modified Tung and Dhir model is used.

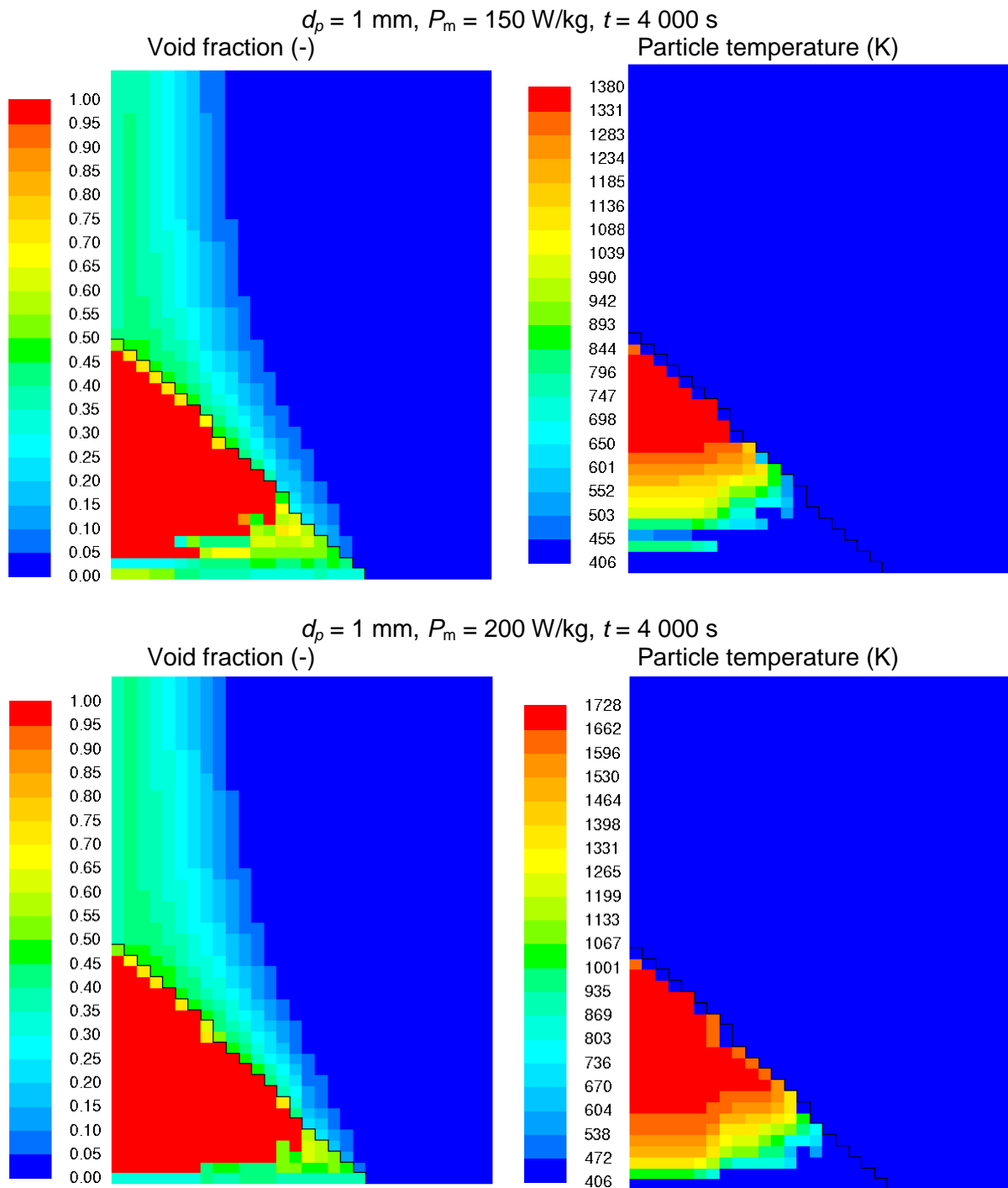


Figure 45. Void fraction (left) and solid particle temperature (right) at the time of 4000 s in the Fluent simulations for the 1 mm bed particles with the specific power P_m equal to 150 (top) and 200 (bottom) W/kg. The Schmidt (2007) version of the modified Tung and Dhir friction model is used.

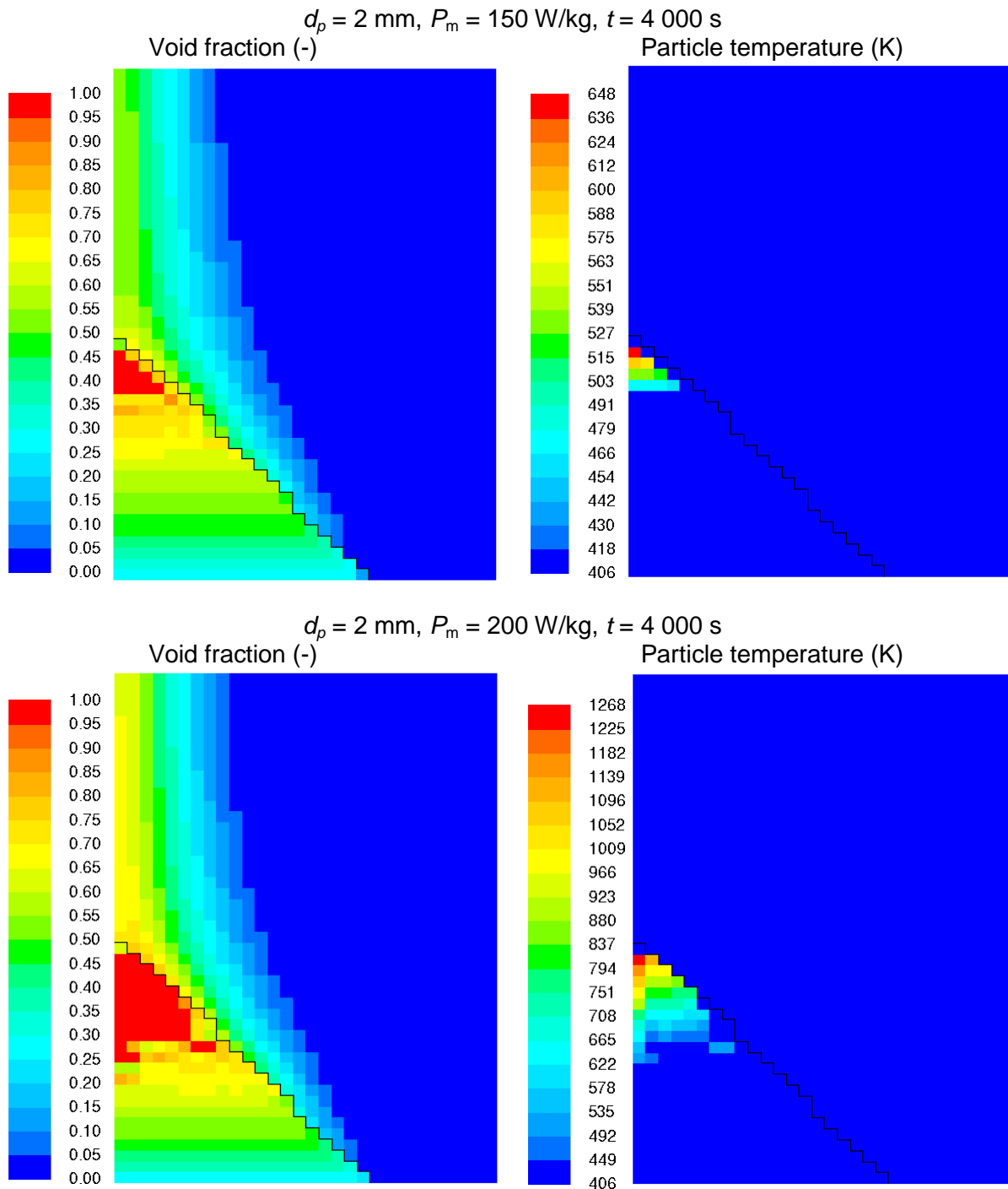


Figure 46. Void fraction (left) and solid particle temperature (right) at the time of 4000 s in the Fluent simulations for 2 mm bed particles with the specific power P_m equal to 150 (top) and 200 (bottom) W/kg. The Schmidt (2007) version of the modified Tung and Dhir friction model is used.

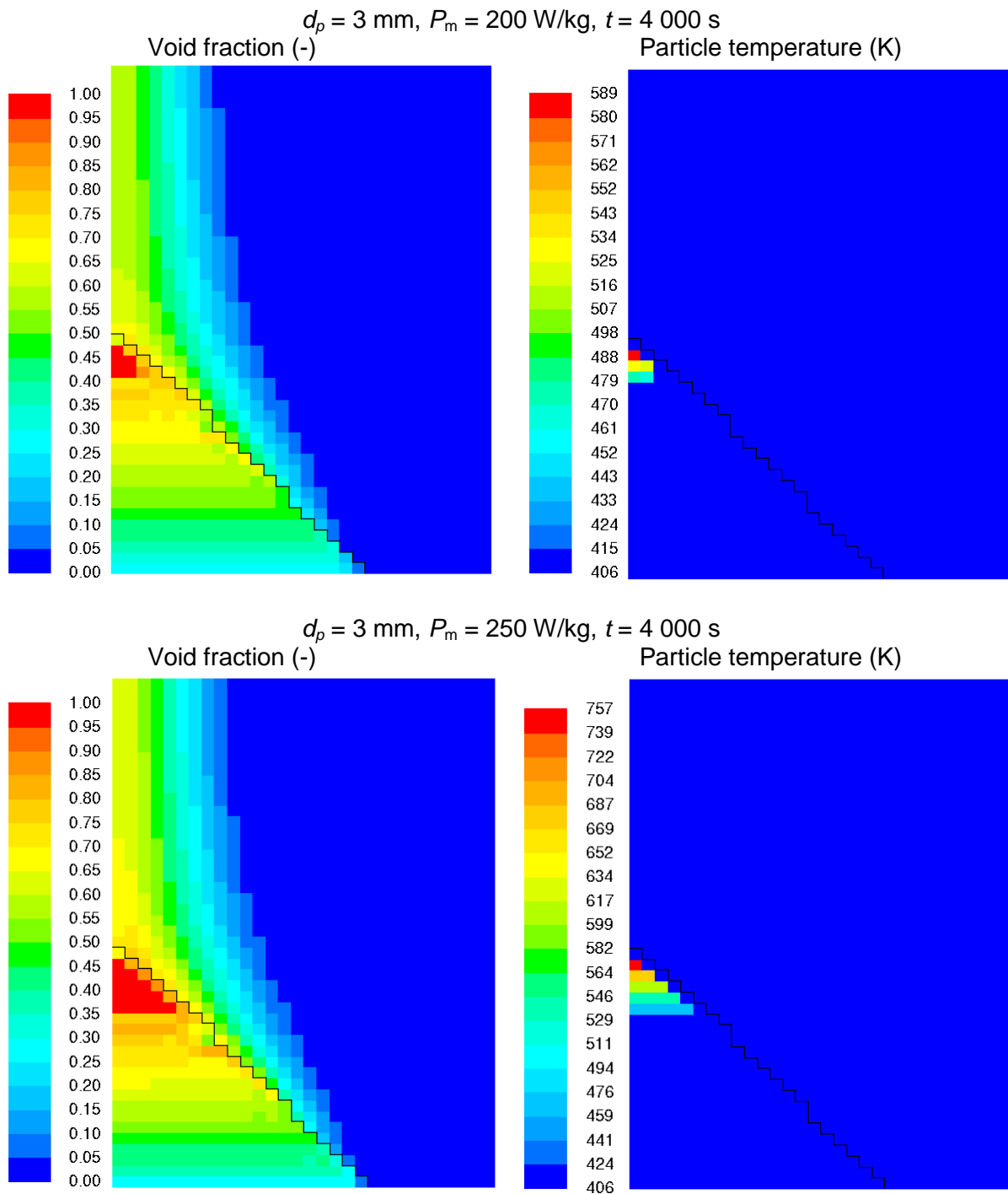


Figure 47. Void fraction (left) and solid particle temperature (right) at the time of 4000 s in the Fluent simulations for 3 mm bed particles with the specific power P_m equal to 200 (top) and 250 (bottom) W/kg. The Schmidt (2007) version of the modified Tung and Dhir friction model is used.

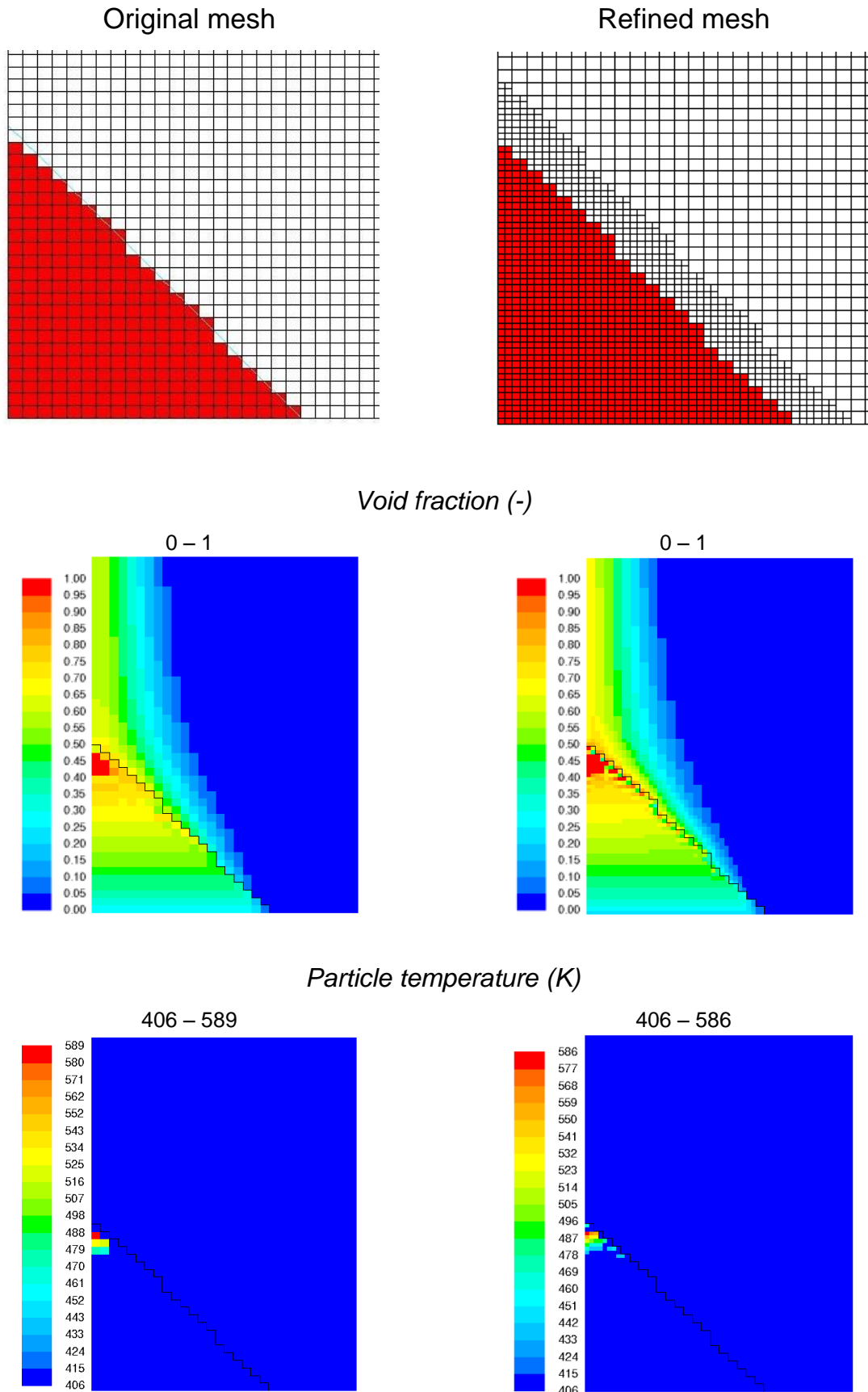


Figure 48. Mesh (top), void fraction (middle) and solid particle temperature (bottom) at the time of 4000 s in the Fluent simulations for the original mesh and for the mesh with once split cells in and close to the bed. The conical bed of the 3 mm particles and specific power equal to 200 W/kg studied by Yakush & Kudinov (2014). The Schmidt (2007) version of the modified Tung and Dhir friction model is used.

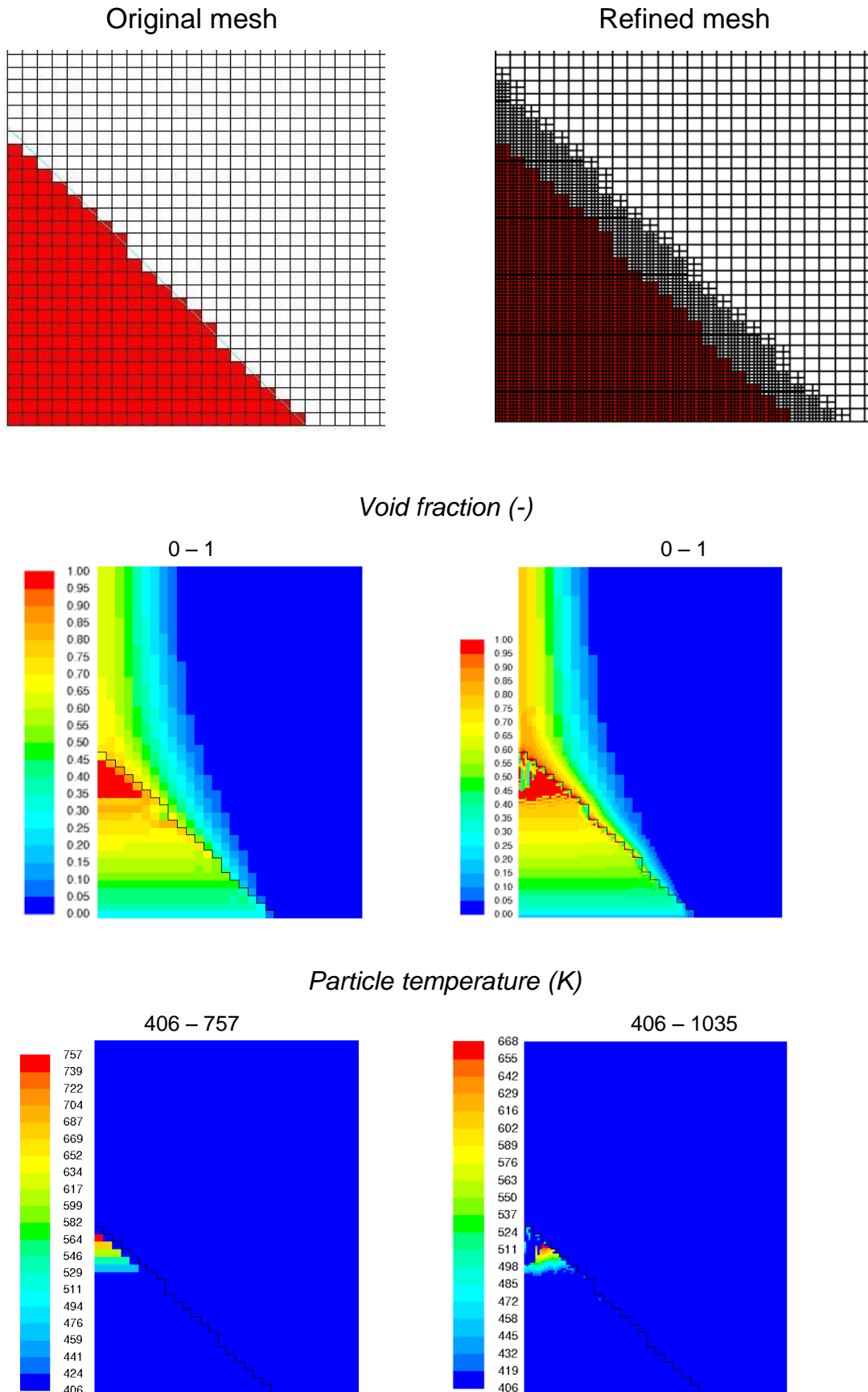


Figure 49. Mesh (top), void fraction (middle) and solid particle temperature (bottom) at the time of 4000 s in the Fluent simulations for the original mesh and for the mesh with twice split cells in and close to the bed. The conical bed of the 3 mm particles and specific power equal to 250 W/kg studied by Yakush & Kudinov (2014). The Schmidt (2007) version of the modified Tung and Dhir friction model is used.

4.4.3 Comparison of the CFD and DECOSIM results

The time evolutions of the maximum particle temperature in the Fluent simulations are compared in Figure 44 to the corresponding results from the DECOSIM simulations (Yakush & Kudinov, 2014). Table 6 summarizes the values of the maximum particle temperature at a time of 5000 s for both simulation tools. The void fraction and particle temperature fields are compared in Figure 50 in those cases for which distributions were given by Yakush & Kudinov (2014).

In the 1 mm cases, the influence of cooling is small and the agreement is again good at least for the first 5000 s. For 3 mm particles with the lower heating power, the CFD-based model ends up to a smaller dry zone and to a maximum particle temperature of about 100 degrees lower than obtained in the DECOSIM simulation.

In the two cases of the 2 mm particles with the specific power of 150 W/kg and the 3 mm particles with the specific power of 250 W/kg, the CFD-based simulation tool gives a much lower maximum steady-state particle temperature (Figure 44). In the Fluent simulations the water penetration flux into the bed is likely larger because of the vertical two-cell step lower in the bed (Figure 43) reducing the dry area and thus the maximum particle temperature (Figure 46 and Figure 47). The mesh refinement in the case of the 3 mm particles with the higher heating power actually increases the difference between the codes for the maximum particle temperature (Figure 44 and Figure 49).

For the 2 mm particles with the higher heating power, the steady-state conditions are not obtained. Mainly because of the convection and viscous terms included in the Fluent simulation and because of the two-cell step in the bed shape, more water penetrates into the bed reducing the dry area.

In all the cases compared in Figure 50, the void fraction distribution outside the particle bed is satisfactory. The DECOSIM results for the pool area are very different from the MEWA results but close to the CFD results computed solving the full multiphase flow equations.

Table 6. Comparison of the maximum solid particle temperature computed in the Fluent and DECOSIM simulations at the time of 5000 s for the conical bed cases studied by Yakush & Kudinov (2014).

Particle diameter (mm)	Specific power (W/kg)	Maximum particle temperature (K)	
		Fluent	DECOSIM (Yakush & Kudinov, 2014)
1	150	1622*	1587*
1	200	1728****	1699*, **
2	150	648	1008
2	200	1315*	1837*, ***
3	200	589	729
3	250	757	1250

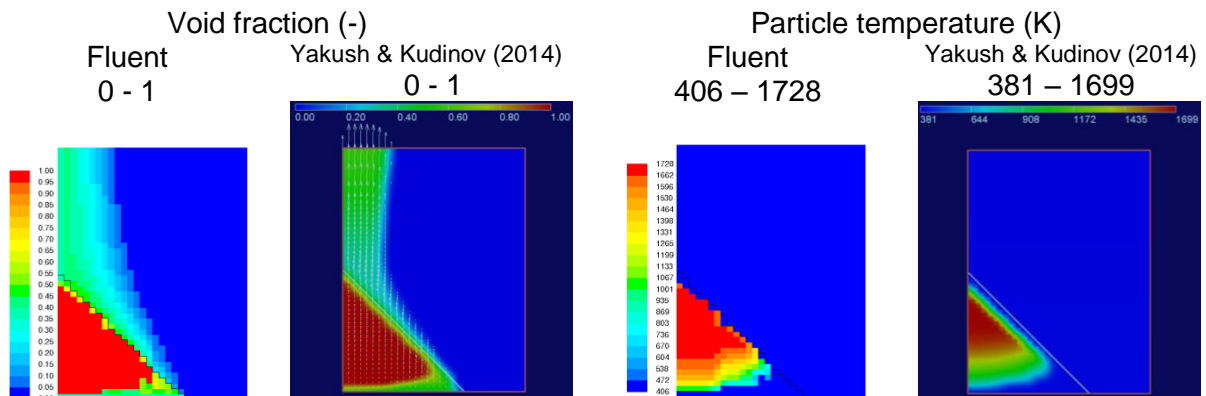
* No dryout. Values given for the time of 5000 s.

** Probably given for the time of 4000 s (cf., Figure 3). The correct value is about 2050 K (cf., Figure 2).

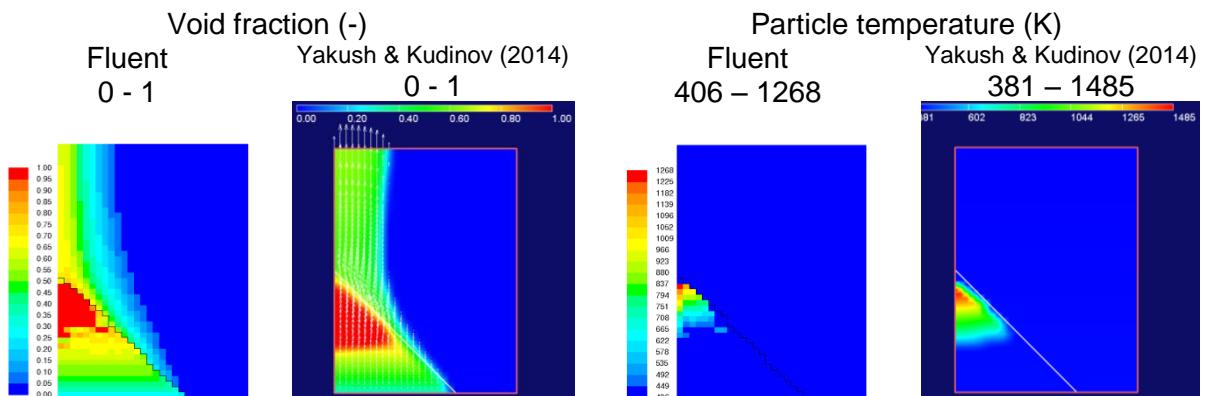
*** Probably a typing error in the table of Yakush & Kudinov (2014). The correct value is about 1650 K, cf., Figure 2).

**** At a time of 4000 s (simulation stopped at about 4200 s, cf., Figure 44).

$$d_p = 1 \text{ mm}, P_m = 200 \text{ W/kg}, t = 4\,000 \text{ s}$$



$$d_p = 2 \text{ mm}, P_m = 200 \text{ W/kg}, t = 4\,000 \text{ s}$$



$$d_p = 3 \text{ mm}, P_m = 200 \text{ W/kg}, t = 4\,000 \text{ s}$$

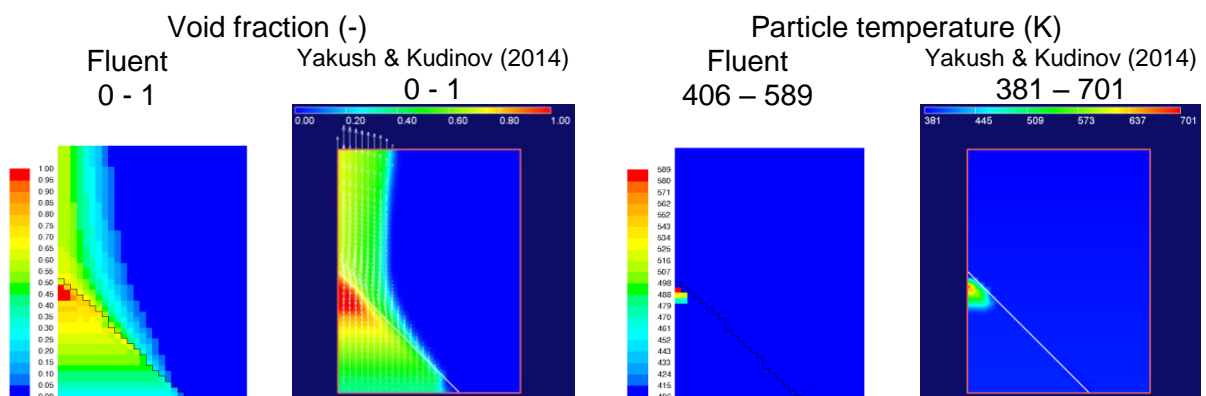


Figure 50. Void fraction (two left columns) and solid particle temperature (two right columns) at the time of 4000 s for 1, 2 and 3 mm particles with the specific power P_m of 200 W/kg in the Fluent simulations of this study and in the DECOSIM simulations according to Yakush & Kudinov (2014). The Schmidt (2007) version of the modified Tung and Dhir friction model is used in both of the simulations.

4.4.4 Discussion

Compared to the MEWA results in Section 3.5, the employment of the Schmidt friction model in the CFD-based simulation improves the agreement with the DECOSIM results. The modifications in the bed shape might have some influence, too. The horizontal penetration of water flow into the particle bed is still likely overestimated in the CFD results. The coarseness of the mesh and the vertical two-cell steps in the bed shape closer to the bottom strengthen the influence of the convection and viscous terms. The CFD simulations with denser meshes indicate that the real flow field close to the tip of the conical bed might be complicated. CFD simulations with an unstructured mesh fitted to the ideal shape of a conical bed would be informative but would still include significant uncertainties due to the friction modelling and limited accuracy in computing converging and possibly swirling bubble flows.

The verification study in Section 4.3 as well as the comparison of the CFD results with the DECOSIM results demonstrate the challenges in comparing results of two very different kind of codes. The coarse-mesh representation of the ideal conical bed does not influence significantly the MEWA results and presumably neither the DECOSIM results. However, when the complete multiphase momentum equations with the convective and viscous terms are solved applying the same coarse spatial discretization, the flow field is characterized by a significant horizontal water flux penetrating relatively deep into the bed.

5. Conclusion

Coolability of corium debris beds was studied computationally by performing numerical simulations with the MEWA code (Bürger et al., 2006; Rahman, 2013) and with a CFD-based multiphase coolability analysis tool developed and implemented into the Fluent code (Takasuo et al., 2015). Especially post-dryout conditions were studied for the hypothetical idealized conical particle beds studied at KTH by Yakush & Kudinov (2014). This study concentrated on the influence of the friction model on the bed behaviour after dryout.

In most beds examined computationally, the time evolution of the maximum particle temperature varies with the simulation tool and friction model. However, for the 1 mm particles, the results are very similar for all the codes and models. After reaching dryout in these cases, the influence of steam cooling is very small due to large friction leading to a small steam flow rate. As a result, the maximum particle temperature does not stabilize but increases with a heating-power dependent rate almost as without any cooling.

The MEWA simulations were performed by applying four different models for the friction force available in MEWA, the Lipinski model, the Reed model, the Tung and Dhir model as well as the modified Tung and Dhir model. In the cases with 2 and 3 mm particles, steady states are reached but the friction model affects strongly on the area of the dry zone and thus on the stabilised maximum particle temperature. Therefore, before trying to quantify a temperature-based coolability criterion, it would be essential to be able to select a friction model which is valid or at least conservative in post-dryout conditions.

The MEWA results the conical particle beds were compared to the DECOSIM results reported by Yakush & Kudinov (2014). As expected, the MEWA results for any friction model do not agree with the DECOSIM results. The disagreement of the MEWA results for the modified Tung and Dhir friction model is neither unexpected, since the Schmidt version of the modified Tung and Dhir model (Schmidt, 2007) used in the DECOSIM simulations is very different compared to the version of the modified Tung and Dhir model presently applied in MEWA (Rahman, 2013).

In order to be able to reproduce the DECOSIM results and thus to insure that the differences between the MEWA and DECOSIM results are arising from the different friction models, the Schmidt (2007) version of the modified Tung and Dhir friction model was added in the CFD-based modelling framework implemented in Fluent. The Fluent implementation was verified against the MEWA results in post-dryout conditions but the outcome is not conclusive. Fluent solves the full multiphase momentum equations including the convective and viscous terms, which with the same coarse spatial discretization used in the MEWA simulations results in a significant horizontal water flux into the bed. For a refined mesh, the Fluent results are closer to the MEWA results indicating a correct implementation of the MEWA models.

The Fluent results with the Schmidt (2007) version of the modified Tung and Dhir friction model for the conical particle bed cases studied at KTH by Yakush & Kudinov (2014) still differ from the DECOSIM results in the cases of the 2 and 3 mm particles. Compared to the MEWA results, the usage of the same friction model improves the agreement with the DECOSIM results. In the Fluent results, the horizontal penetration of water flow into the bed is larger due to the coarseness of the mesh and vertical two-cell steps in the shape of the bed surface. The coarse-mesh representation of ideal conical beds does not influence significantly the MEWA results and presumably neither the DECOSIM results. However, when the complete multiphase momentum equations with the convective and viscous terms are solved applying the same coarse spatial discretization, the flow field is characterized by significant water fluxes penetrating horizontally relatively deep into the bed. On the other hand, if the complex flow fields obtained in the CFD simulations in some cases for the cone-tip area are realistic, the simplified momentum equations do not predict bed behaviour correctly.

The full momentum equations in the Fluent simulations with the coarse-mesh approximation of the surface of the ideal conical beds lead to flow fields, which are significantly different compared to the MEWA and DECOSIM results. Although the source of the differences is thus likely known, they hamper the verification and comparison studies. Accordingly, comparisons should be done in geometries, for which possible differences in the spatial discretization do not change the computational case definition.

CFD-based simulations should also be performed for the truncated-cone cases studied by Yakush & Kudinov (2014). In the truncated-cone geometry, the influence of the additional terms in the full momentum equation is expected to be small. Furthermore, the influence of the uncertainties in the actual bed shape is likely smaller.

References

- Ansys, 2015a. ANSYS Fluent Customization Manual. Release 16.2. ANSYS, Inc., Canonsburg.
- Ansys, 2015b. ANSYS Fluent Theory Guide. Release 16.2. ANSYS, Inc., Canonsburg.
- Ansys, 2015c. ANSYS Fluent User's Guide. Release 16.2. ANSYS, Inc., Canonsburg.
- Atkhen, K. & Berthoud, G., 2006. SILFIDE experiment: Coolability in a volumetrically heated debris bed. *Nuclear Engineering and Design*, 236, pp.2126–2134.
- Bürger, M. et al., 2006. Validation and application of the WABE code: Investigations of constitutive laws and 2D effects on debris coolability. *Nuclear Engineering and Design*, 236, pp.2164–2188.
- Chikhi, N., Coindreau, O., Li, L.X., Ma, W.M., Taivassalo, V., Takasuo, E., Leininger, S., Kulenovic, R., Laurien, E., 2014. Evaluation of an effective diameter to study quenching and dry-out of complex debris bed. *Annals of Nuclear Energy*, 74, pp.24–41.
- Hu, K., Theofanous, T.G. 1991. On the measurement and mechanism of dryout in volumetrically heated coarse particle beds. *International Journal of Multiphase Flow*, 17 (No. 4).
- Huang, Z., & Ma, W., 2018. Validation and application of the MEWA code to analysis of debris bed coolability. *Nuclear Engineering and Design*, 327, pp.22–37.
- Imura, S. & Takegoshi, E., 1974. Effect of Gas Pressure on the Effective Thermal Conductivity of Pack Beds. *Heat Transfer Japanese Research*, 3(4).
- Lienhard, J.H. 2012. A Heat Transfer Textbook, 4th edition. Phlogiston Press, Cambridge, Massachusetts, USA.
- Lipinski, R.J., 1982. A Model for Boiling and Dryout in Particle Beds. US Nuclear Regulatory Committee, NUREG/CR-2646, SAND82-0765
- Lipinski, R.J. 1984. A coolability model for postaccident nuclear reactor debris. *Nuclear Technology*, 65, pp. 53-66Luikov, a. V. et al., 1968. Thermal conductivity of porous systems. *International Journal of Heat and Mass Transfer*, 11(2), pp.117–140.
- Luikov, a. V. et al., 1968. Thermal conductivity of porous systems. *International Journal of Heat and Mass Transfer*, 11(2), pp.117–140.
- Maxwell, J.C., 1873. *A treatise on electricity and magnetism | Vol. 1*,
- Rahman, S., 2013. *Coolability of Corium Debris under Severe Accident Conditions in Light Water Reactors*. Insitut für Kernenergetik und Energiesysteme, University of Stuttgart.
- Reed, A.W. 1982. The effect of channeling on the dryout of heated particulate beds immersed in a liquid pool. Doctoral Thesis, Department of Mechanical Engineering, Massachusetts Institute of Technology, 1982.
- Rohsenow, W. 1952. A method of correlating heat transfer data for surface boiling of liquids. *Trans. ASME*, 74, pp. 969–976.Schmidt, W., 2007. Interfacial Drag of Two-phase Flow in Porous Media. *Int. J. Multiphase Flow*, Vol. 33, pp. 638–657.
- Schmidt, W., 2007. Interfacial Drag of Two-phase Flow in Porous Media. *Int. J. Multiphase Flow*, Vol. 33, pp. 638–657.
- Song, J.H. et al., 2006. The effect of corium composition and interaction vessel geometry on the prototypic steam explosion. *Annals of Nuclear Energy*, 33(17-18), pp.1437–1451.
- Stephan, P., Martin, H., Kabelac, S., Mewes, D., Kind, M., & Schaber, K. ed., 2010. VDI Heat Atlas.
- Taivassalo, V., & Takasuo, E., 2017. Predicting debris bed behaviour in post-dryout conditions. RESEARCH REPORT VTT-R-00762-17. VTT, Espoo.
- Takasuo, E., Taivassalo, V., Kinnunen, T., Lehtikuusi, T., 2015, Coolability analyses of heap-shaped debris bed. RESEARCH REPORT VTT-R-00367-15. VTT, Espoo.
- Takasuo, E., 2016. An Experimental Study of the Coolability of Debris Beds with Geometry Variations. *Annals of Nuclear Energy*, 92, pp.251–261. Available at: <http://www.sciencedirect.com/science/article/pii/S0306454916300408>.
- Takasuo, E., 2015. *Coolability of porous core debris beds: Effects of bed geometry and multi-dimensional flooding*. VTT Technical Research Centre of Finland Ltd. D.Sc. thesis. <http://www.vtt.fi/inf/pdf/science/2015/S108.pdf>. Available at: <http://www.vtt.fi/inf/pdf/science/2015/S108.pdf>.

- Vortmeyer, D., 1978. Radiation in Packed Solids. In *6th International Heat Transfer Conference, Toronto, Canada*.
- Yagi, S. & Kunii, D., 1957. Studies on effective thermal conductivities in packed beds. *AIChE Journal*, 3(3), pp.373–381. Available at:
<http://onlinelibrary.wiley.com/doi/10.1002/aic.690030317/full>.
- Yakush, S. & Kudinov, P., 2014. A model for prediction of maximum post-dryout temperature in decay-heated debris bed. In *22nd International Conference on Nuclear Engineering. July 7-11, 2014, Prague, Czech Republic*.

ANNEX 2

Ex-vessel steam explosion with non-central break location



RESEARCH REPORT

VTT-R-05270-17

Ex-vessel steam explosion with non-central break location

Authors: Magnus Strandberg

Confidentiality: Public

Report's title Ex-vessel steam explosion with non-central break location	
Customer, contact person, address SAFIR2018 Research Program	Order reference SAFIR 6/2017
Project name Comprehensive Analysis of Severe Accidents	Project number/Short name 113414/CASA
Author(s) Magnus Strandberg	Pages 12
Keywords Steam explosion, MC3D, Full 3D model, Side break	Report identification code VTT-R-05270-17
<p>Summary</p> <p>The focus of this report was to continue examining the ex-vessel steam explosion phenomena in a Nordic boiling water reactor, and more specifically a steam explosion resulting from a non-central break of the reactor pressure vessel. This type of scenario was simulated with the MC3D code utilizing a full 3D model, as the side break scenario is not axisymmetric a simplified 2D model could not be used. In the previous work, the full 3D model had not been successful in producing a steam explosion, so one of the goals of this work was to examine if this was due to some implementation error in the model.</p> <p>The simulations proved quite unstable but it was possible to produce steam explosions, and the resulting steam explosions were quite strong in comparison to the previous 2D model results, about six times higher dynamic pressure peaks and two times larger impulse. As this was a different scenario with different geometry its difficult to conclude if the difference was due to the scenario being more likely to produce a stronger explosion or due to the different method involved.</p> <p>The instabilities were in the explosion part of the simulations and caused the simulations to stop before the defined end time. Which in turn makes analysing the pressure peaks at the wall difficult as it becomes uncertain if the maximum had been reached before the calculations ended.</p>	
Confidentiality	Public
Espoo, 27.09.2017	
Written by  Magnus Strandberg, Research Scientist	Reviewed by  Tuomo Sevón, Senior Scientist
Accepted by  Anitta Hämäläinen, Research Team Leader	
VTT's contact address P.O. Box 1000, FI-02044 VTT, Finland	
Distribution (customer and VTT) SAFIR2018 Reference Group 2 VTT	
<i>The use of the name of VTT Technical Research Centre of Finland Ltd in advertising or publishing of a part of this report is only permissible with written authorisation from VTT Technical Research Centre of Finland Ltd.</i>	

Contents

1. Introduction	4
2. Steam explosion theory in brief	4
3. MC3D	4
4. Input model	5
5. Results and analysis	6
6. Discussion	11
7. Conclusion	11
References	12

1. Introduction

As part of severe accident in a nuclear power plant, there might arise situations where steam explosions are possible. Therefore the phenomenon needs to be analysed in order to assess its effect on the containment structure. To study the phenomena a specialised fuel coolant interaction code, MC3D[1, 2] is being used. This report is a direct follow up on the work that was started in “Ex-Vessel Steam Explosion Analysis with MC3D” [3]. Where the full 3D models with side breaks gave very inconsistent results compared to the 2D central break scenarios.

As such the focus on this report is to study the side break scenarios and see if the inconsistencies was due to the input deck used in [3] or if there are larger problems with the code. This will be accomplished by studying a smaller sample of scenarios instead of a large sample for sensitivity analysis as was the case in the previous work.

The version of MC3D being used is still v3.8, but the input has been rewritten. The boundary conditions are still the same as in the previous work. that is the starting conditions are derived from a MELCOR[4] simulation of a station blackout in a Nordic BWR.

2. Steam explosion theory in brief

For a more in-depth analysis of the steam explosion phenomenon consult “Ex-Vessel Steam Explosion Analysis with MC3D” [3].

Steam explosions are a fast and violent Fuel Coolant Interaction(FCI) that usually is separated into three separate stages: Premixing, Triggering and Explosion phase. The separation is due to the different time scales of the three phases as well as different phenomena involved. In the premixing phase the first coarse fragmentation of the molten corium (melt) jet occurs over a time scale of a few seconds. At some point after the premixing has started there is a triggering event where the quasi stable system produced by the pre-mixing collapses in a small region of the system. This initiates the explosion phase, where the pressure wave propagates through the system further collapsing it and increasing the energy of the shock wave.

It should be noted that some phenomena involved in the steam explosions are not thoroughly understood at the moment, and that models and code are at least in part based on best estimates. In both the premixing and explosion stage the drop fragmentation is one phenomenon that still has some open questions. The triggering event is also highly stochastic and very hard to predict. Thus from a safety perspective it is conservative to assume it always occurs.

3. MC3D

The MC3D (Multi Component 3D) code is developed by IRSN and CEA in France, and is a multidimensional Eulerian code used to simulate multiphase and multi-constituent flows for nuclear safety applications. It is usable for both research and safety usage. MC3D utilises two different FCI applications that have a common numeric solver. One of the is for the premixing stage and the other for the explosion stage. The triggering stage is incorporated into the code used for the explosion stage. This splits the simulation into two parts. In the first part the fragmentation of the melt jet, the vapour build-up and the heat transfer is simulated. The second part, that can be started at a time chosen by the user, handles the rapid fragmentation of the melt drops and the heat transfer from the molten drops to the coolant. [5]

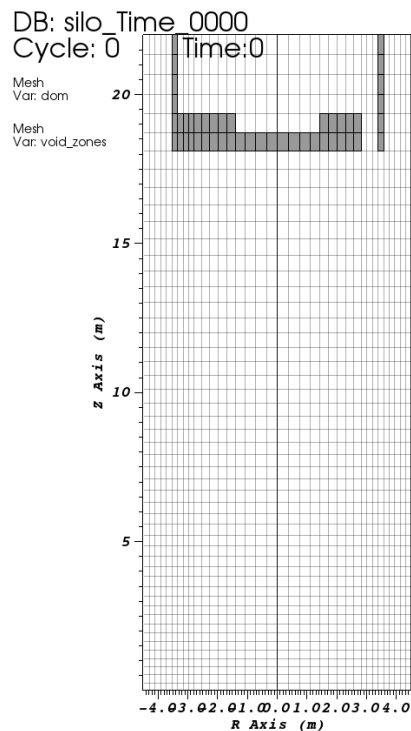


Figure 1. Slice of the simulation model, showing the break location in the RPV.

Table 1. Simulation parameters.

Parameter	Value
Melt temp	2900 K
Ambient pressure	246 kPa
Ambient overheating	0 K
Coolant subcooling	50 K
Water level	14 m

4. Input model

The input models geometries are based on a nordic BWR reactor cavity. It is simplified as an empty cylinder with the RPV at the top. The geometries have not changed from the model used in [3], but the input model was rewritten in whole to try to separate it from the previous input that produced inconsistent results.

The input model is done with a break very close to the side of the RPV, however as the premixing simulation takes a long time to complete, so only one break location was analysed. In Fig. 1 a slice of the 3D model along the Z axis shows the location of the break; the RPV is marked in grey. Figure 2 shows an isometric view of the model at the start of the simulation. The red represents the melt and the blue the water, lighter shades of blue indicate void build up. These figures have been produced with the VisIt tool[6].

Table 1 list the parameters used to define the start of the simulation. These are the same as in the previous work, except for the water level that was risen to 14 meters to increase the volume available for mixing. The drop diameter constant was set to 3 millimetres and the fragmentation model is the constant model.

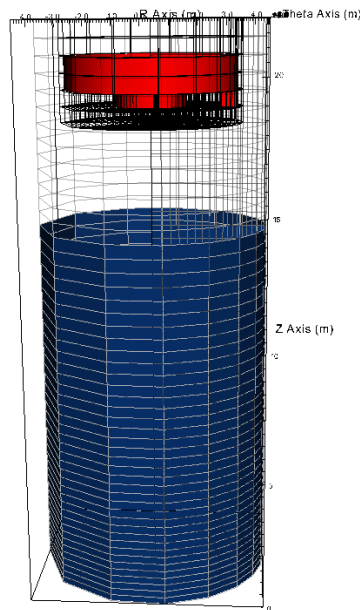


Figure 2. Simulation model at the beginning of the premixing, the Corium melt in red and the coolant in blue. The RPV parts are made transparent to better show the melt.

5. Results and analysis

From the premixing, one of the most important parameters is the internal parameter “explosivity”, which measures the amount of molten drops suspended in water. As it is only the molten drops suspended in water that are able to undergo the rapid fine fragmentation during the explosion stage, thus providing energy for the explosion. In Fig. 3, the explosivity of the premixture is presented. The explosivity quickly rises as the melt begins to fragment into the water. However due to void build-up some drops instead get suspended in vapour instead of water which makes the explosivity drop. As the thickness of the vapour film surrounding the jet is not stable, the explosivity varies over time.

This makes steam explosions very sensitive to changes in the triggering time, and as the triggering time is highly stochastic it becomes very complicated to predict the explosion strength in a given scenario. This has been studied by Grishchenko et al [7]. at KTH, Stockholm. Their work on statistically analysing steam explosions both with traditional methods and using neural networks. Their work showed that the impulse caused by a single premixture can vary in strength by up to 50 times by changing the time scale by only 110ms. Due to this triggering time is probably the largest cause of uncertainty in both simulating and experiments.

The explosion part of the simulation did not prove as stable as the premixing part. All simulation runs, but one, stopped before the defined end time even though different parameters and triggering times were tested. In table 2 is presented the triggering times simulated, the run time of the simulation and whether or not the shock-wave reached the wall in this scenario. The reason for the instability seems mostly to be due to some cell reaching the upper pressure boundary causing the calculations to terminate. As the parameters for the premixing are almost identical to the 2D cases performed in earlier SAFIR projects [3], this could be an indication that the full 3D model get more explosive. However as the break locations were different it is unfortunately

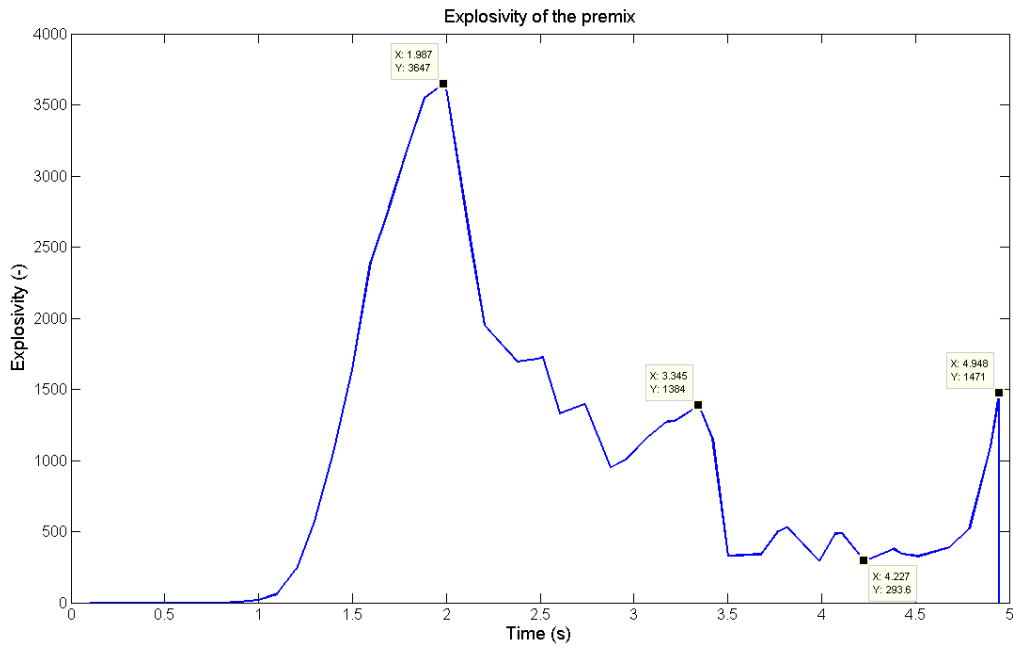


Figure 3. Explosivity of the premix.

DB: silo_Time_0094
Cycle: 94 Time:4.72245

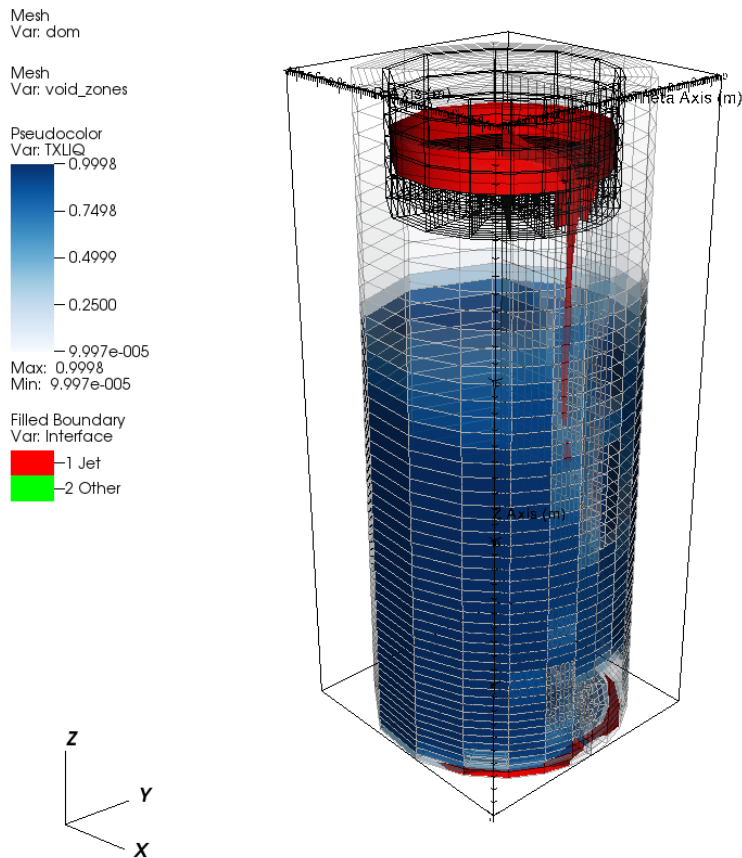


Figure 4. Visualization of the premixing. Showing the melt jet and the spread of at the bottom of the cavity. Lighter colours of blue indicate regions containing higher void build-up.

Table 2. Simulation results from the explosion stage.

Triggering time (s)	Stopped prematurely	Run time (s)	Shock-wave reached the wall the cavity wall
1.57	Yes	0.003	Uncertain
1.98	Yes	0.002	No
2.60	Yes	0.005	Uncertain
3.07	Yes	0.006	Yes
3.70	Yes	0.007	Yes
4.50	No	0.036	Yes
4.89	Yes	0.004	Yes

not possible to draw any conclusions. A way to verify could be to simulate a central break also in full 3D but unfortunately that was not possible to fit into the scope of this report.

In Fig. 5 the maximum dynamic pressure at the wall from the simulations is illustrated; X axis zero is set to the individual triggering times. The pressure is the maximum pressure in any any cell along the wall. Some of the datasets are noticeable shorter than other, due to the difference in run time. The line terminated by an “X” is for the simulation where the shock-wave did not reach the wall before the simulation stopped. This has been visually checked from the VisIt tool output files. The simulation with triggering time 4.50 seconds is not included in Fig 5, but instead presented in Fig. 6 to increase readability of the graphs. Triggering at 4.50 s produced a similar shaped pressure curve as the 2D cases in previous work.[3] However, the maximum pressure recorded is about six times higher, 250MPa compared to 40MPa. However it remains unclear if this is due to switching to the full 3D model or if the side break scenario actually produces much stronger explosions. With triggering time 4.50 s, the largest impulse received in any cell along the wall was 0.4935 MPas. Comparing this to the 2D results, the 3D results was two times larger.

Figure 7 shows a scatter plot of the maximum wall pressure recorded plotted against triggering time. In Fig. 8 is show a similar scatter plot, but instead plotted against run time of the different simulations. As the simulations ended prematurely the maximum pressure has to be analysed with this taken into account. The run time of the two first triggering times, 1.58s and 1.98s, are shorter compared to the others. This probably explains why they show the lowest maximum pressure compared to the other triggering times. However from the remaining data sets it would seem as the maximum pressure is increased if the trigger is delayed, which is to be expected as more corium then has time to fragment into the water. However the amount of triggering times simulated is probably too low to draw any statistically sound conclusions from the results. Especially as the simulations in all but one case ended before the specified time.

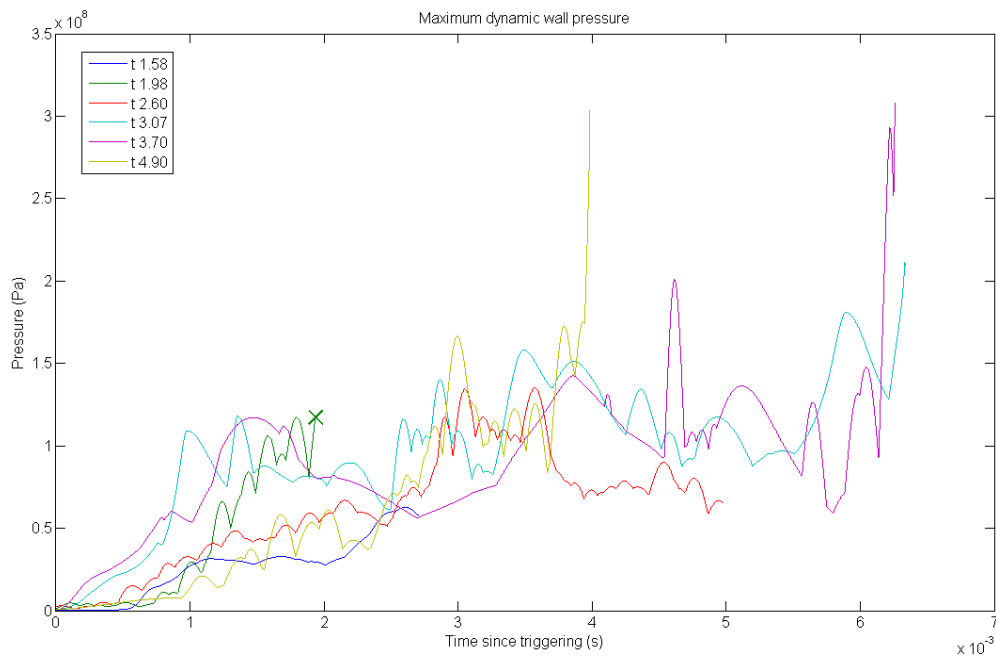


Figure 5. Maximum dynamic pressure, recorded in the wall area. Line terminated by "X"; the shock-wave did not reach the wall area before calculations terminated. Trigger time 4.50 s not shown in this figure due to readability.

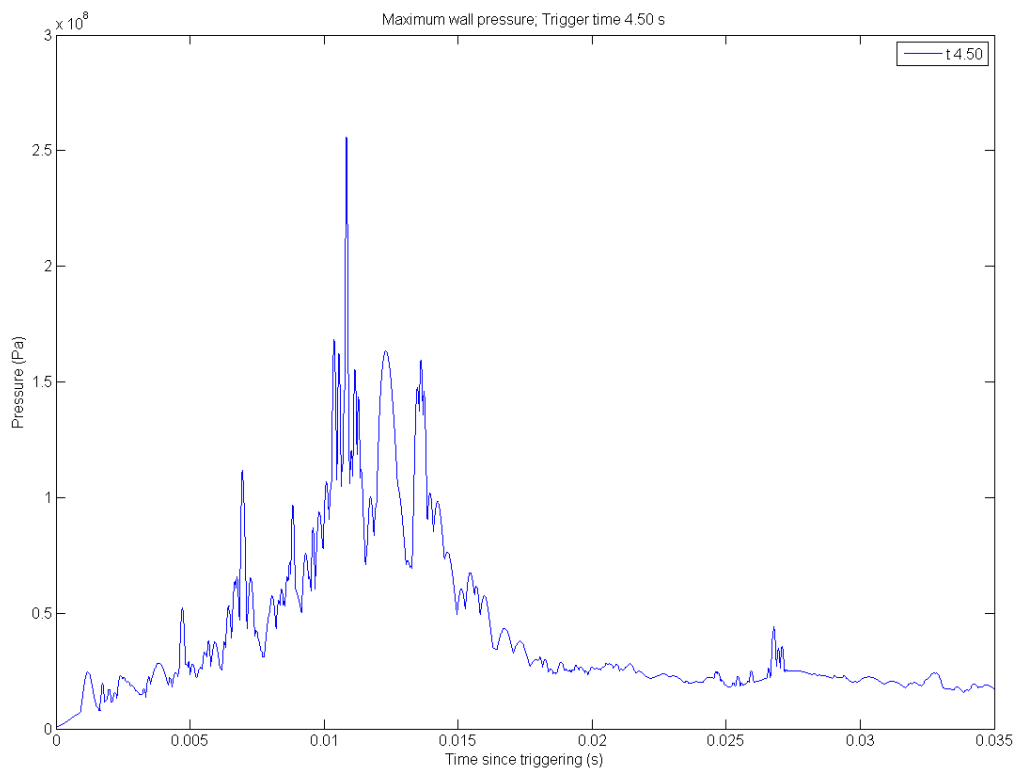


Figure 6. Maximum dynamic pressure, recorded in the wall area for trigger time 4.50 s.

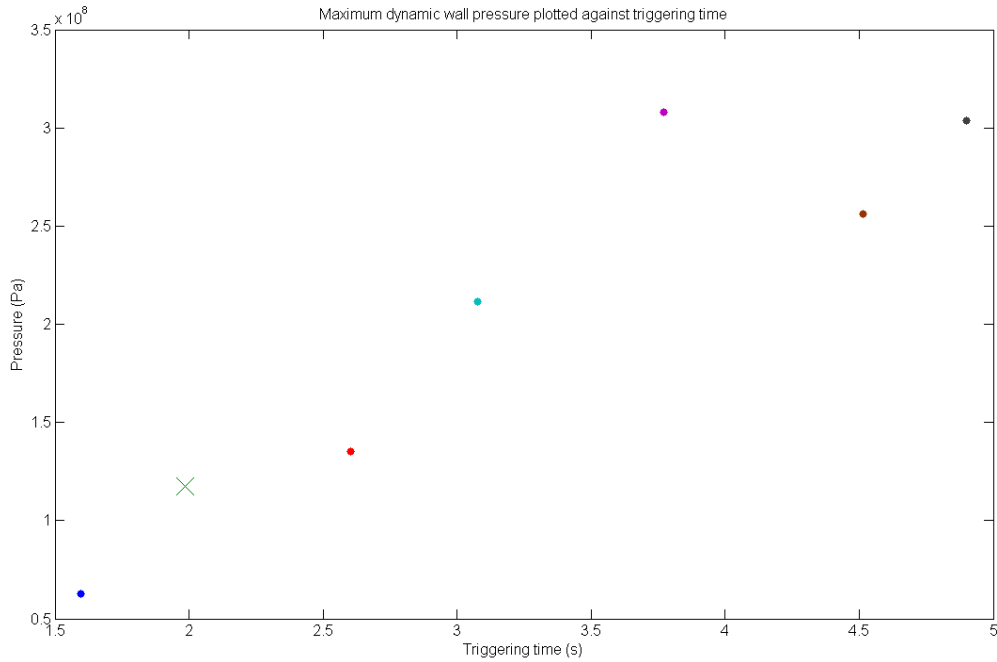


Figure 7. Maximum wall pressure recorded plotted against triggering time. Marker "X" indicates bulk of the shock-wave did not reach the wall area.

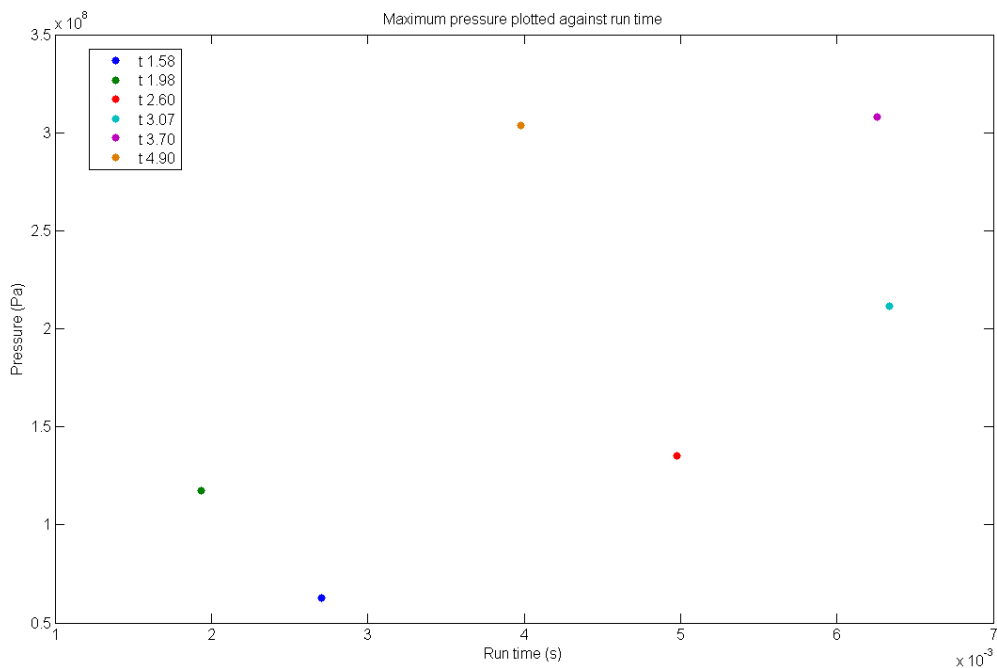


Figure 8. Maximum dynamic wall pressure plotted against run time of the different simulations. Triggering time 4.50 excluded due to readability.

6. Discussion

The goal here was to further study the steam explosion phenomena by utilizing MC3D and more specifically see if the 3D model needed for the side break scenario could produce similar results as the 2D model used in the central break scenario. In that regard the simulations were a success. The rewritten model did produce steam explosions of quite considerable strength. Whether this difference between the previous results from the 2D central break model and this result, is due to the switch to a full 3D model or if the scenario actually produces much stronger steam explosions is unclear. Similar pressure results have been achieved in other MC3D models[8], so the pressure peaks are at least not unprecedented.

However, the move from 2D to 3D does bring with it lots of negative side effects. The largest is that the computational times grow with the cell count making the simulations very time consuming, especially the premixing stage. This scenario used a model with 14 400 cells and the premixing took roughly 3 weeks. This would make a sensitivity analysis of any parameter that affects the premixing very resources demanding.

Another problem was the stability of the explosion part of the simulation. Both due to traceable shut-downs, i.e. cell pressure too high, as well as unknown errors. This makes accurately analysing the pressure at the wall, and thus also the impulse received, very difficult.

Its also good to keep in mind that the premixing parameters, in the tested scenario, e.g. melt temperature, are set so that they defiantly satisfy the conditions required for a premixture that can produce a steam explosion. Thus, the fact that the resulting steam explosion is strong is to be expected.

7. Conclusion

Rewriting the 3D model did have the intended results and it was possible to achieve a steam explosion also with the 3D model. There were however stability issues with the explosion part of the simulation. Which in turn adds uncertainty to analysis of the results. The triggering time that managed to run its course produced an explosion that showed dynamic pressure peaks six times higher than the previously simulated 2D cases with two times stronger impulses revived at the wall. The triggering times that did not finish would probably have produced similar if not slightly stronger explosions, as they mostly stopped due to the internal pressure limit being reached.

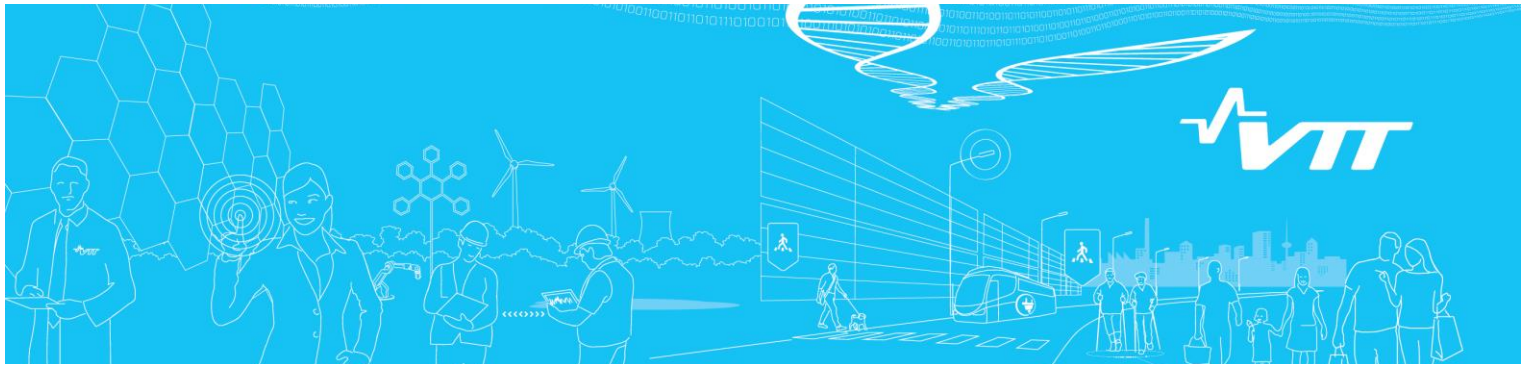
Also from the results it would seem as if later triggering times result in stronger explosions, which is logical as more melt would have had time to fragment into water at that point. This is hard to verify due to the instability problems.

With all the uncertainties already involved in steam explosion research, going to full 3D models might not at this stage be worth the extra hassle. Effort might be better spent on studying e.g. the effect different starting conditions have on the simulation outcome, at least for the time being.

References

- [1] Renaud Meignen, Stephane Picchi, Julien Lamome, Bruno Raverdy, Sebastian Castrillon Escobar, and Gregory Nicaise. The challenge of modeling fuel-coolant interaction: Part i - premixing. *Nuclear Engineering and Design*, 280(0):511 – 527, 2014.
- [2] Renaud Meignen, Bruno Raverdy, Stephane Picchi, and Julien Lamome. The challenge of modeling fuel-coolant interaction: Part II - steam explosion. *Nuclear Engineering and Design*, 280(0):528 – 541, 2014.
- [3] Magnus Strandberg. Ex-vessel steam explosion analysis with mc3d. G2 pro gradu, 2016-10-25.
- [4] RO Gauntt, JE Cash, RK Cole, CM Erickson, LL Humphries, SB Rodriguez, and MF Young. Melcor code manuals—version 1.8. 6. *USNRC NUREG/CR*, 6119, 2005.
- [5] R. Meignen and S. Picchi. MC3D user guide v3.8. *PSN-RES/SAG/2012-00063*, 2012.
- [6] Hank Childs, Eric Brugger, Brad Whitlock, Jeremy Meredith, Sean Ahern, David Pugmire, Kathleen Biagas, Mark Miller, Cyrus Harrison, Gunther H. Weber, Hari Krishnan, Thomas Fogal, Allen Sanderson, Christoph Garth, E. Wes Bethel, David Camp, Oliver Rübél, Marc Durant, Jean M. Favre, and Paul Navrátil. VisIt: An End-User Tool For Visualizing and Analyzing Very Large Data. In *High Performance Visualization—Enabling Extreme-Scale Scientific Insight*, pages 357–372. Oct 2012.
- [7] Dmitry Grishchenko, Simone Basso, and Pavel Kudinov. Development of a surrogate model for analysis of ex-vessel steam explosion in nordic type bwrs. *Nuclear Engineering and Design*, 310:311–327, 2016.
- [8] Matjaž Leskovar and Mitja Uršič. Estimation of ex-vessel steam explosion pressure loads. *Nuclear Engineering and Design*, 239(11):2444–2458, 2009.

ANNEX 3
Level 2 PRA studies – Steam explosions
and integration of PRA levels 1 and 2



RESEARCH REPORT

VTT-R-00191-18

Level 2 PRA studies – Steam explosions and integration of PRA levels 1 and 2

Authors: Tero Tyrväinen, Ilkka Karanta

Confidentiality: Public

Report's title	
Level 2 PRA studies – Steam explosions and integration of PRA levels 1 and 2	
Customer, contact person, address	Order reference
VYR	SAFIR 4/2017
Project name	Project number/Short name
Probabilistic risk assessment method development and applications	114491/PRAMEA
Author(s)	Pages
Tero Tyrväinen, Ilkka Karanta	26/
Keywords	Report identification code
Probabilistic risk analysis, severe accident, steam explosion	VTT-R-00191-18
Summary	
<p>This report continues the development of simplified probabilistic risk analysis models of a boiling water reactor plant. Previously developed level 1 and level 2 models are extended and integrated so that it is possible to list most important event tree sequences, initiating events and basic events with regard to radioactive releases. A special focus is on the computation of emergency core cooling system recovery probability based on level 1 results. Some possibilities for the improvement of FinPSA level 2 software tool are identified concerning tight integration of PRA levels 1 and 2. The example model can later be utilised in further studies, demonstrations, training and FinPSA testing.</p> <p>To handle separately different types of uncertainties in dynamic containment event trees, a method with two-phase uncertainty analysis has been outlined. The method would enable explicit modelling of dynamic dependencies and production of proper uncertainty distributions as a result at the same time, whereas with normal one-phase uncertainty analysis it is difficult to do both.</p> <p>Ex-vessel steam explosions are also discussed in the report. Probabilistic modelling of steam explosions is very challenging because uncertainties related to the phenomenon are very high. Pressure impulses of explosions can be calculated quite well using deterministic software tools, but the probability that an explosion occurs in the first place cannot be properly estimated based on current knowledge. Currently, it is a good idea to use conservative probabilities in PRA. It could be studied if explosion triggering probabilities could be estimated based on some physical parameters calculated by deterministic software tools.</p>	
Confidentiality	Public
Espoo 16.1.2018	
Written by	Reviewed by
Tero Tyrväinen Research Scientist	Kim Björkman Research Scientist
	Accepted by
	Eila Lehmus Research Team Leader
VTT's contact address	
Distribution (customer and VTT)	
SAFIR reference group 2	
<p><i>The use of the name of VTT Technical Research Centre of Finland Ltd in advertising or publishing of a part of this report is only permissible with written authorisation from VTT Technical Research Centre of Finland Ltd.</i></p>	

Contents

1. Introduction.....	3
2. Ex-vessel steam explosions.....	3
2.1 Previous studies	3
2.2 Possibilities to improve probabilistic modelling	5
3. Dynamic containment event trees.....	7
4. Boiling water reactor plant model.....	8
4.1 Level 1.....	8
4.2 Plant damage states	10
4.3 Level 2.....	11
4.4 Emergency core cooling recovery.....	11
4.5 Results	15
4.6 Sensitivity analysis.....	17
4.6.1 Ex-vessel steam explosions.....	17
4.6.2 Basemat melt-through.....	18
4.7 Basic event contributions.....	18
5. Outline for two-phase uncertainty analysis.....	22
6. Conclusions	23
References.....	24

1. Introduction

Level 2 probabilistic risk analysis (PRA) studies nuclear power plant accident progression after core damage, and frequency, size and composition of radioactive releases [1]. Severe accident phenomena, e.g. hydrogen explosions, and timings of events, such as cooling system recovery, play an important role in such analyses. Information on severe accident progression provided by deterministic analyses is crucial to the construction of proper level 2 PRA. Integrated deterministic and probabilistic safety analysis (IDPSA) aims to bring the two types of analysis closer and improve their co-operation.

This report continues the development of simplified boiling water reactor (BWR) plant PRA models [2-4]. Level 1 PRA model from [3] is integrated with the level 2 model from [2]. The level 2 model is extended to cover five plant damage states. The integration of the PRA levels is made tight so that level 1 information is used in level 2 modelling, and the contributions of level 1 events are seen in level 2 results [5]. Special focus is on modelling the recovery of an emergence core cooling system.

Steam explosions [6] are one severe accident phenomenon that can lead to the rupture of the reactor containment. Steam explosions can occur when core melt gets in contact with water, for example when core melt spills from the pressure vessel to the lower part of a flooded containment. A steam explosion is a very complex phenomenon which is difficult to model realistically in deterministic and probabilistic analyses. Some attempts have been made, such as [7-10]. This report discusses the probabilistic modelling and what would be needed to make it more realistic.

2. Ex-vessel steam explosions

A steam explosion [6] can occur when core melt gets in contact with water and vaporizes it rapidly. It may occur inside or outside the pressure vessel. Explosions outside the vessel (ex-vessel explosions) are considered more likely and dangerous. Therefore, only ex-vessel explosions are discussed in this report. An ex-vessel steam explosion may occur when the pressure vessel is broken and core melt spills to the lower part of the containment which is flooded with water.

A steam explosion is a very complex physical phenomenon involving several different phases including premixing, triggering, propagation, and expansion and energy release. The details of the phenomenon are presented for example in [8]. They are not repeated in this report.

2.1 Previous studies

Probabilistic modelling of an ex-vessel steam explosion requires the estimation of the probability that an explosion occurs and the probability that the explosion breaks the containment if it occurs. In [8], the modelling for BWR was performed in the following way:

- It was conservatively assumed that steam explosion is triggered with certainty in high pressure, and with probability 0.5 in low pressure, assuming that core melt spills to the lower drywell (LDW) that contains enough water.
- An uncertainty distribution was given for the pressure impulse of the explosion. The distribution was varied depending on the pressure (high or low) and how much core melt was ejected to the LDW (more than 50% of the core inventory or less than 50% of the core inventory). The distributions are presented in Figure 1. In the figure, LP refers to low pressure, HP refers to high pressure, 1 means that much melt is ejected to the LDW and 2 means that little melt is ejected to the LDW. The distributions were loosely based on pressure impulses presented in literature [11].

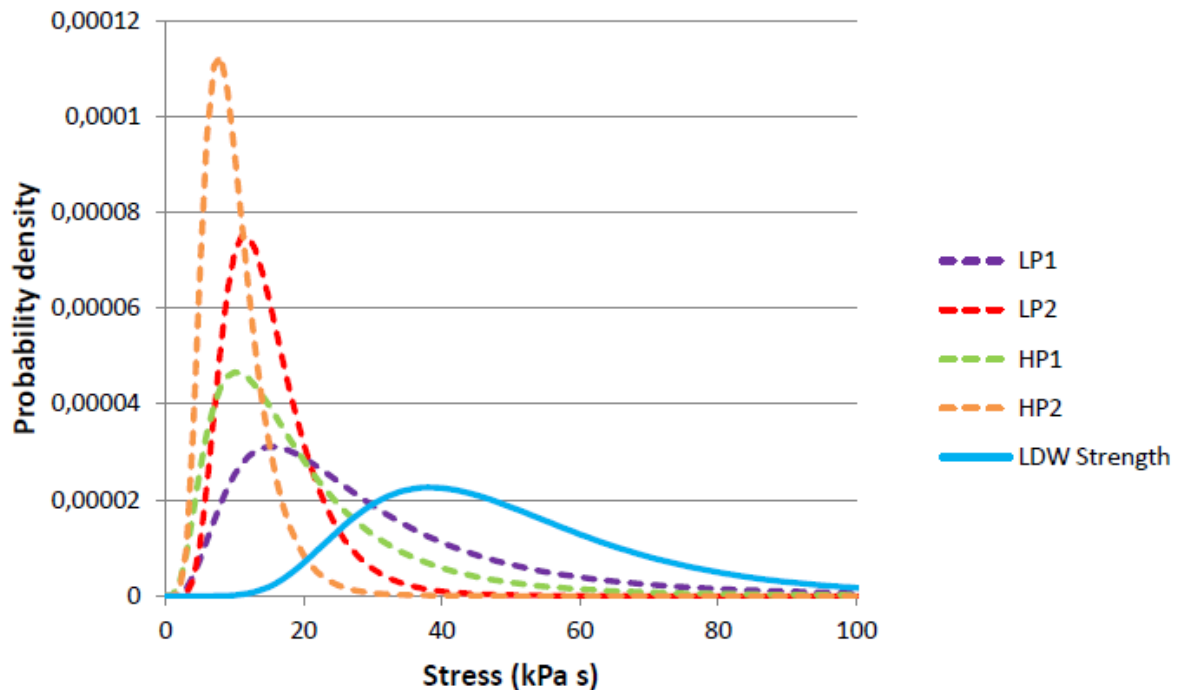


Figure 1: Distributions used to determine whether LDW fails due to pressure impulse caused by ex-vessel steam explosion.

- An uncertainty distribution was also given for the LDW strength and it is also presented in Figure 1.
- The probability of containment failure was calculated based on the distributions of the pressure impulse and the LDW strength. The probabilities are presented in Table 1.

Table 1: Conditional probability of explosion impulse exceeding strength of LDW walls given vessel failure, explosion trigger and enough water in LDW.

	Much melt ejected (case 1, late or no ECCS recovery)	Little melt ejected (case 2, early ECCS recovery)
RCS depressurized (case LP)	0.207	0.021
RCS not depressurized (case HP)	0.091	0.003

- Steam explosion was considered possible only if the LDW contained enough water, which depended on the success of the flooding function and the time of the vessel breach.
- The amount of core melt ejected to the LDW depended on the core meltdown and several factors affecting it.

Steam explosions have also been studied by deterministic MC3D computer code in [8-9]. MC3D is primarily used to estimate the pressure impulses of ex-vessel steam explosions. In the studies, calculated pressure impulses were significantly larger than those used in the previously presented study [8] and generally found in literature [11]. On the other hand, in the studies, there were difficulties to find scenarios where explosion is actually triggered. This could imply that the conservative explosion triggering probabilities used in the previously presented study [8] could be much too conservative. However, it is not known how reliably the

explosion triggering probability can be judged based on MC3D analyses. Based on the analyses, it also seems to make difference how the pressure vessel is ruptured, i.e. explosions were triggered only for cases where the pressure vessel leaks from the centre. It was however suspected that the model could be incorrect for the side breaks of the vessel.

In [12], a probability distribution was calculated for steam explosion pressure impulses in a pressurized water reactor (PWR) plant. Steam explosions were simulated using deterministic JASMINE software. Uncertainty distributions were specified for input parameters including melt jet inlet diameter, velocity, initial melt temperature, water pool depth and melt droplet diameter during premixing. Latin hypercube sampling was used to generate computation cases based on the uncertainty distributions. That way uncertainties were propagated through deterministic calculations to produce the uncertainty distribution for the pressure impulses. It was assumed that an explosion is triggered at the time of the first peak of the premixed mass, but the timing was also varied in alternative computation cases. It was claimed that the triggering probability is included in the resulting pressure impulse distribution. We assume that explosion was not triggered in some computation cases, and the probability that an explosion is not triggered comes from the portion of those cases.

Grishchenko et al. have performed extensive steam explosion analyses using TEXAS-V software and a surrogate model [13, 14]. The surrogate model is a simplified model that is based on artificial neural networks and a database of TEXAS-V results. The surrogate model produces approximately same results as TEXAS-V and enables a large number of simulations to perform comprehensive sensitivity and uncertainty analyses. Grishchenko et al. studied the effects of explosion triggering times, and they found that the behaviour of pressure impulses as a function of the triggering time is chaotic. The produced pressure impulses changed a lot even with a tiny change in the triggering time.

2.2 Possibilities to improve probabilistic modelling

Based on the previous steam explosion studies, it is evident that there is room for improvement in both deterministic and probabilistic modelling of steam explosions. Concerning probabilistic modelling, uncertainties are high for most of the parameters involved.

The explosion triggering probabilities are the most questionable parameters in the previous studies. It seems that triggering probabilities cannot be estimated realistically currently because deterministic computer codes are not reliable enough, sensitivity of triggering to parameter changes is great, and uncertainties related to the triggering phenomena are high. Plenty of development work and analyses are needed before well-justified probabilities can be estimated. Currently, it is better to use conservative values in the PRA models. However, the conservativeness of the values has to be acknowledged.

To estimate more realistic explosion triggering probability, a comprehensive and realistic set of calculation cases should be analysed using a deterministic computer code, like in [12]. However, since there is significant uncertainty on the correctness of the computer code itself, for each computation case, a triggering probability should be estimated instead of only examining whether explosion was triggered in the deterministic calculation. Possibly, the triggering probability of a case could be judged based on physical variables, e.g. explosivity curve produced by MC3D. The overall triggering probability could then be calculated as the average of the triggering probabilities of different cases. A method to estimate the triggering probability based on the explosivity curve should however be developed first. It can be difficult because the triggering time is highly uncertain, and even with high explosivity an explosion does not occur without a trigger.

Estimation of pressure impulse distributions would require many more deterministic analyses than performed in the previous studies [8-9]. Those previous studies also focused mainly on the maximum values whereas complete distributions would be needed. With a sufficiently reliable computer code and a comprehensive and realistic set of calculation cases, the

pressure impulse distribution could be approximated in a straightforward manner. Reference [12] provides a good example for the selection of computation cases and propagation of uncertainties through deterministic analyses. The use of a surrogate model, like in [13], can be beneficial when a large number of cases needs to be calculated. If deterministic analyses cannot be performed reliably enough, an alternative is to use an uncertainty distribution that covers different values found in the literature and gives more weight on larger values.

To estimate the actual containment failure probability in the case of a steam explosion, the best option would be to apply structural reliability analysis. The classical approach is to somehow estimate two probability distributions: the explosion load (pressure impulse) and the resistance of the structure to loads of different sizes. The probability that the structure fails is then the probability that the load exceeds the resistance. In the general case, resistance may depend on the load, there may be several failure modes, failure probability may be time-dependent (taking into account the ageing of structures, corrosion, etc.), and there may be several (or an infinite number of) positions where the structure may fail. In this case, the probability density function is multidimensional: each component of the random vector involved represents a resistance random variable or a load random variable acting on the system. Integration is usually then carried out by numerical approximation methods, of which Monte Carlo simulation is the most popular. Structural reliability analysis in general is explained in [15] and [16], and the impact of explosive loads on structures is treated in [17].

In the light of previous analyses [9-10], it also seems to make a difference how the core melt spills from the pressure vessel to the containment, which depends on how the pressure vessel leaks. Pressure vessel failures could be divided into different cases for which separate steam explosion analyses could be performed, such as in [10]. However, probabilities should then also be estimated for different vessel leak cases. Structural reliability analysis methods could be used for that. If it would not be possible to do this, the worst leak case could be assumed to simplify the analysis.

In [10], it was concluded that loss of coolant accident (LOCA) and station blackout scenarios were quite similar from the steam explosion analysis point of view. In general, severe accident progression, at least on containment event tree level, is very similar for several different plant damage states. Therefore, it seems that there is no reason to put much effort on the analysis of multiple plant damage states, since probabilistic steam explosion modelling can be assumed to be similar for different plant damage states. The focus should be more on the analysis of different cases with regard to pressure conditions, vessel failure, flooding time and amount of core melt.

Probability estimation of steam explosions could be improved upon in several ways, given sufficiently reliable steam explosion analysis computer code and time to perform enough computations. One is based on calculating numerical probabilities in hypercubes, motivated by the wish to reduce uncertainties surrounding the probability of steam explosions and explosion strength. In it, we consider a range of initial condition variables, most notably related to melt ejection mode [14] and pool characteristics; call the space formed by these variables the parameter space. This parameter space is divided into hypercubes by partitioning the possible range of each initial condition variable to a suitable number of intervals. For each such hypercube, a number of Monte Carlo experiments is conducted by selecting the initial condition variables randomly within the hypercube, and then performing a simulation with a steam explosion code (such as MC3D) to determine whether a steam explosion takes place, and if it does, what is its strength. The (numerical) probability of a steam explosion in the hypercube is the number of cases when the explosion occurred divided by all trials in that hypercube. The probability distribution of explosion load in the hypercube is formed based on the explosion loads in the positive cases. The conditional containment failure probability can be calculated based on the explosion load distribution, e.g. using load vs. strength approach. The steam explosion probability and the conditional containment failure probability would then be tabulated in a table, indexed by the intervals of the individual variables in the hypercube.

When assessing an accident sequence in a level 2 analysis, probability distribution over the hypercubes of the parameter space is determined, e.g. with help of deterministic analyses. Then, the steam explosion probability and the conditional containment failure probability can be calculated based on the probability table and the distribution of hypercubes.

Modelling of steam explosions in level 2 PRA can be performed in several ways:

1. Containment failure probability in a containment event tree sequence can be estimated outside the PRA model based on the deterministic analyses, and a single probability (with uncertainty distribution) can be brought to the PRA model. This probability may have been estimated, for example, by the “hypercube method” introduced in the previous paragraphs.
2. Containment failure probability in a containment event tree sequence can be calculated in the PRA model. The results of deterministic analyses could be incorporated in the model as a table representing different input parameter cases and corresponding containment failure probabilities (or triggering probabilities and pressure impulses); also here the “hypercube method” presented in the previous paragraphs could be used. The input parameters would have probability distributions, and values for them could be drawn on each simulation cycle of Monte Carlo simulation. The containment failure probability would be obtained from the table based on the drawn input parameter values. This approach requires a suitable PRA tool, like FinPSA level 2 [18], and it was used in a simplified manner with only four input parameter cases in [8].
3. Separate containment event tree sequences can be created for different steam explosion cases, e.g. based on melt ejection mode and pool characteristic as presented in [14]. Containment failure probabilities in different sequences can be estimated in the PRA model or outside the PRA model as described in the previous alternatives.

The best alternative for modelling is not obvious. Alternatives 2 and 3 can make the model complicated. On the other hand, they enable modelling of dependencies between phenomena, such as that the LDW pool characteristics affect also ex-vessel debris coolability. Alternative 2 enables modelling of input parameters as continuous variables, and more detailed modelling of dependencies than alternative 3. Alternative 3 could easily be used to calculate importance values for different scenarios related to input parameters. However, with alternative 3, the event tree could grow very large.

3. Dynamic containment event trees

The level 2 modelling in FinPSA software tool [18] is based on dynamic containment event trees (CETs) and containment event tree programming language (CETL). The CETL language is used to define functions to calculate conditional probabilities of event tree branches, timings of the accident progression and amounts of releases. A CETL function is defined for each branch of a dynamic containment event tree, and a CET also contains an initial conditions section, where the plant damage state, source term computation routine, and some probability and process variable values are defined. In addition, the model contains a global “common section”, where some global variables and functions can be defined. CETL programming is very flexible. At any branch, new value can be set or calculated for any global variable, and that way accident progression can be modelled dynamically. Binning rules can also be defined to divide the end points of the CET into release categories.

To account for uncertainties related to variable values, it is possible to specify probability distributions for parameters and perform Monte Carlo simulations. At each simulation cycle, a value is sampled from each specified distribution, and based on that, numerical conditional probabilities are calculated for all the branches, and values are calculated for all variables at each end point of the CET. After the simulations, statistical analyses are performed to calculate

frequency and variable value distributions for each end point and release category among other statistical results and correlation analyses. It is also possible to just calculate point values of the CET based on the mean values of distributions.

4. Boiling water reactor plant model

This chapter continues the development of simplified boiling water reactor (BWR) plant PRA models [2-4]. Level 1 PRA model from [3] is integrated with the level 2 model from [2]. The level 2 model is extended to cover five plant damage states. The integration of the PRA levels is made tight so that level 1 information is used in level 2 modelling, and the contributions of level 1 events are seen in level 2 results [5]. Specifically, level 1 minimal cut set information is used to determine the probability of emergency core cooling recovery in different cases in level 2.

4.1 Level 1

The level 1 part of the model contains four event trees:

- Large LOCA (Figure 2)
- Loss of main feedwater (Figure 3)
- Loss of offsite power (Figure 4)
- General transient (Figure 5)

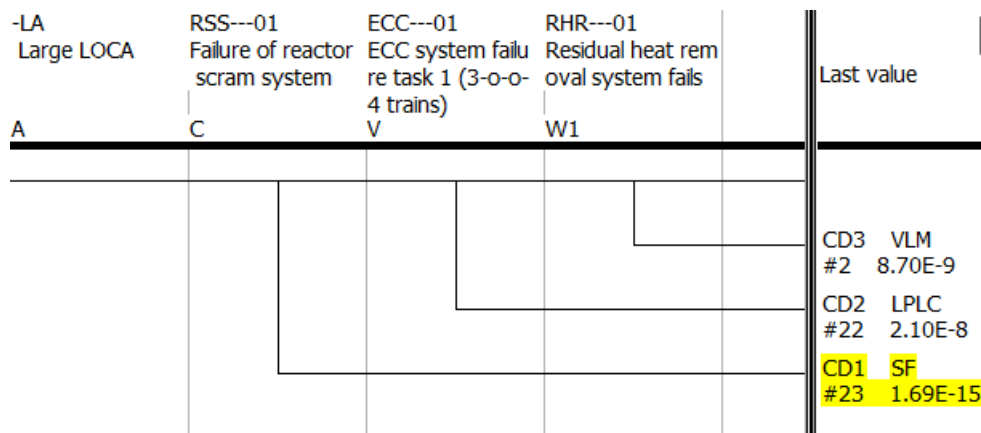


Figure 2: Event tree for large LOCA.

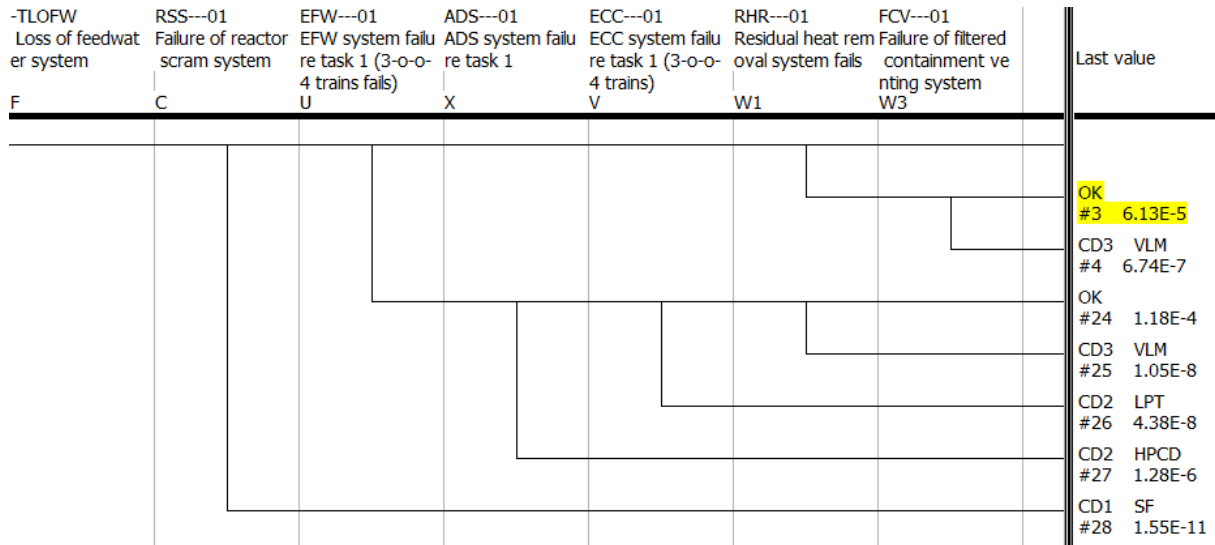


Figure 3: Event tree for loss of main feedwater.

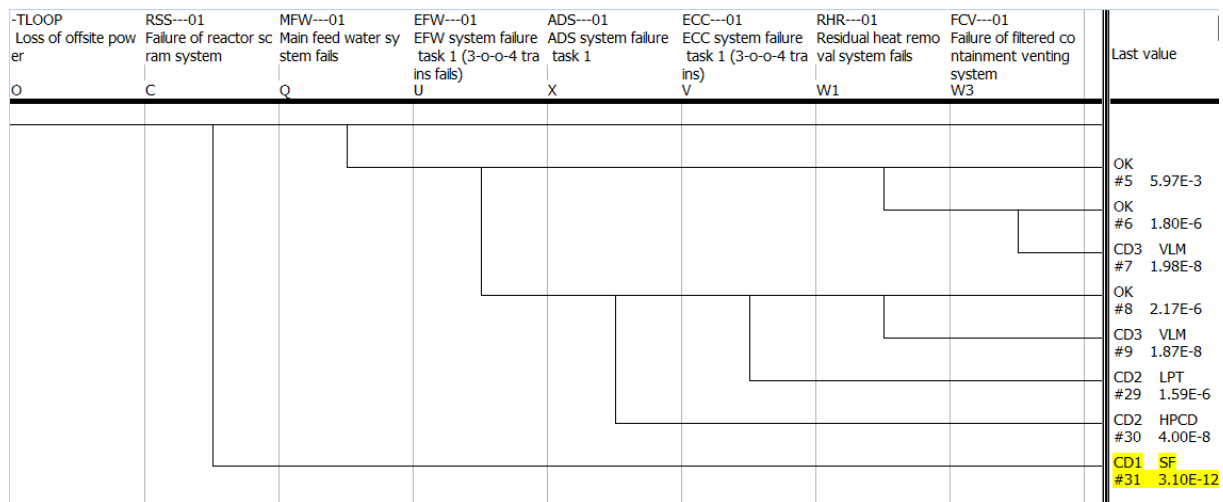


Figure 4: Event tree for loss of offsite power.

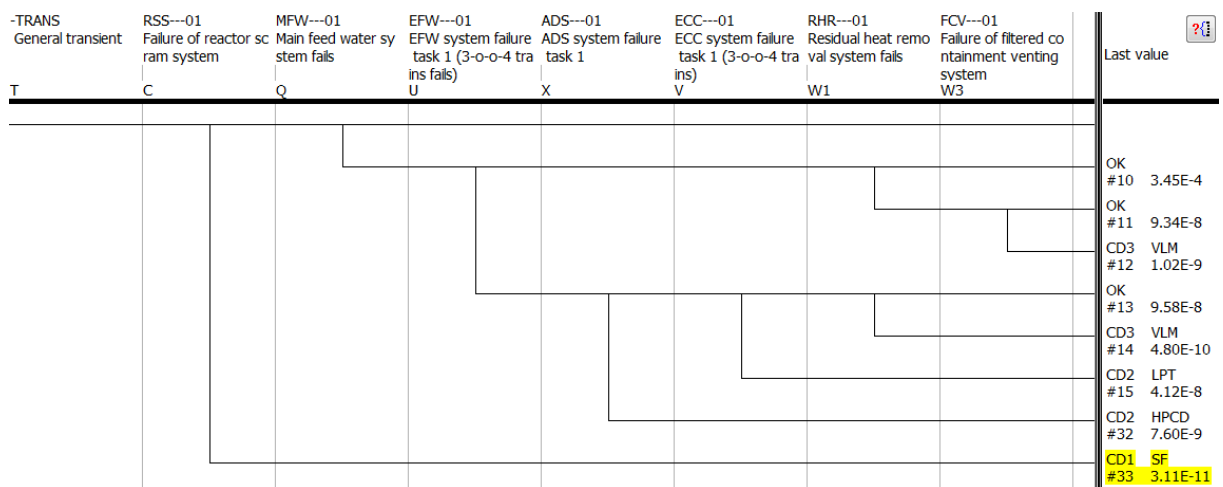


Figure 5: Event tree for general transient.

The main safety systems modelled are:

- Reactor scram system

- Main feedwater system
- Emergency feedwater system
- Depressurization system
- Emergency core cooling system (ECCS)
- Residual heat removal system
- Filtered containment venting system

The emergency feedwater system operates in high pressure, and the emergency core cooling system operates in low pressure. Support systems for the main safety systems include AC power system, DC power system, component cooling system, heating, ventilation and conditioning system, service water system, and two reactor protection systems (RPSs) serving different safety systems. Everything except reactor protection systems have been modelled in a simplified manner, because the model was originally developed for I&C system analysis [3].

For this study, uncertainty distributions were assigned to the frequencies of initiating events, the probabilities of most basic events, and the probabilities of common cause failures. All the distributions were lognormal, and error factors ranged between 2 and 200. Error factor is defined here as the 95th percentile value divided by the median. The parameter values were completely made up for this study. Generally, larger error factors were assigned to basic events with smaller probabilities and especially to I&C component failures. Similar basic events were placed into the same population, which means that their probabilities are same in uncertainty analysis.

4.2 Plant damage states

The model contains five plant damage states (PDSs):

- High pressure melting
- Low pressure melting due to LOCA
- Low pressure melting due to transient
- Melting due to scram failure
- Very late melting

Level 1 sequences are linked to PDSs via interface trees that directly correspond to the PDSs:

- High pressure core damage (HPCD)
- Low pressure LOCA (LPLC)
- Low pressure transient (LPT)
- Scram failure (SF)
- Very late melting (VLM)

The interface trees can be seen at the end points of the event trees presented in Figures 2-5. Each interface tree contains only one sequence which means that the level 1 sequences are practically directly linked to the PDSs.

4.3 Level 2

The model presented in [2], originating from [8], was the basis for the development of the level 2 part. The model in [2] contained one containment event tree which covered both high pressure and low pressure melting scenarios. In this report, high and low pressure cases are separated on PDS level. Hence, separate CETs are developed for low and high pressure. The structure of the high pressure melting CET is the same as in [2]. For low pressure melting due to LOCA, low pressure melting due to transient, and very late melting, the CET structure is similar except that the depressurization section is not included because the pressure is assumed to be low already. The CETs for high pressure melting and low pressure melting due to transient are presented in Figures 6-7.

The CETL modelling behind the CET sections has been discussed in [4] and is not repeated here.

For low pressure melting due to LOCA, it is assumed that the containment is not inert with much smaller probability. Lognormal distribution with mean value 0.01 and error factor 5 is used in this case, whereas mean probability 0.3 is used for transient. This means that the risk of hydrogen explosion is significantly smaller in the LOCA case.

For very late melting, the accident modelling is similar to the low pressure cases, which was also the case in [19]. However, timings were changed so that core melting starts around 100000 seconds (\approx 28 hours) after the initiating event, and other events occur correspondingly after that. The timings were set quite roughly without in-depth consideration, because the modelling of very late melting accident was not the main focus of the study. All containment failures in the very late melting CET lead to release category 'very late containment failure'.

The CET for melting due to scram failure contains only one sequence which assumes failure of containment isolation. The modelling decision is based on the model presented in [19]. The CET is presented in Figure 8.

Table 2 presents the release categories and containment failure modes of the model.

4.4 Emergency core cooling recovery

Emergency core cooling system recovery was modelled based on level 1 results. It was identified that core cooling failure can be caused by

- cooling system component (e.g. pump or valve) failures,
- power supply failures,
- heating, ventilation and conditioning (HVAC) system failures,
- demineralized water tank failure,
- reactor protection system failures,
- component cooling water system component failures,
- service water system component failures,
- condensation pool failure.

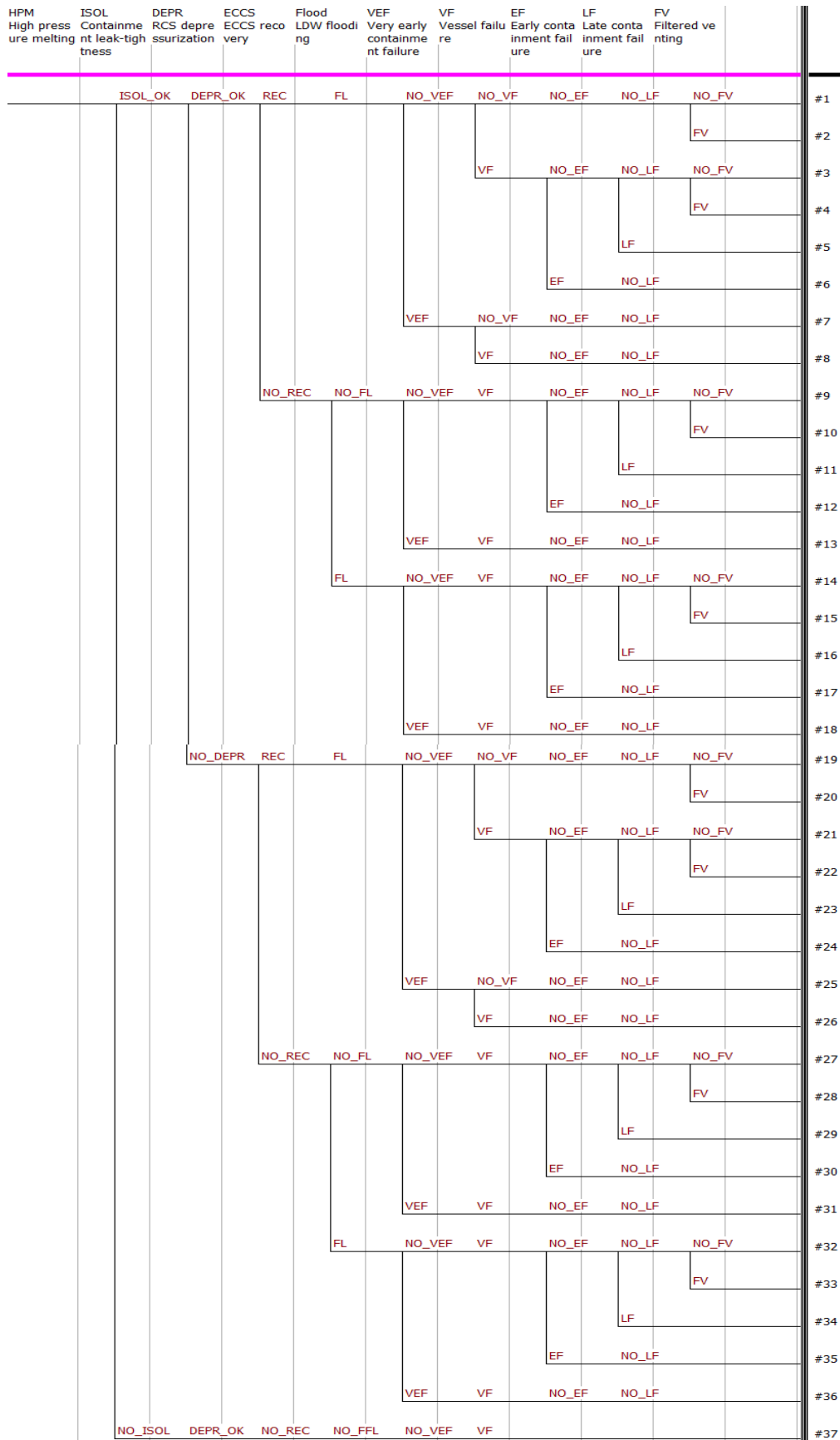


Figure 6: Containment event tree for high pressure melting.

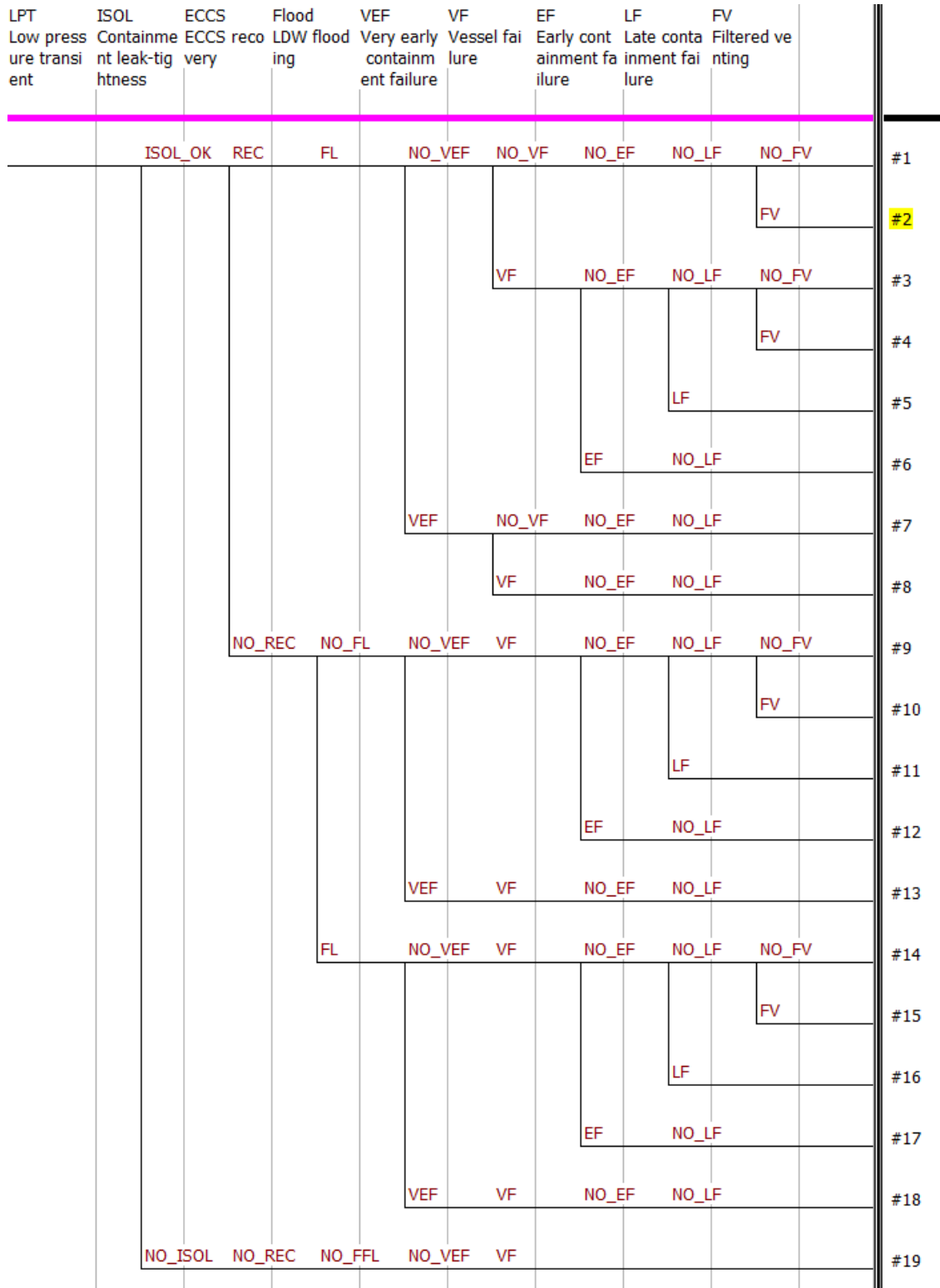


Figure 7: Containment event tree for low pressure melting due to transient.

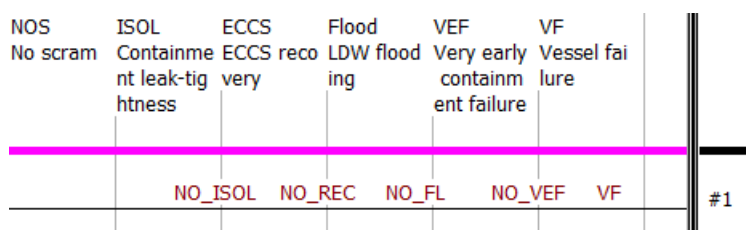


Figure 8: Containment event tree for melting due to scram failure.

Table 2: Containment failure categories and the corresponding failure modes used in the CET model.

Release category	Containment failure/vent mode
No containment failure of filtered venting (OK)	-
Isolation failure (ISOL)	1. Containment not leak-tight (ISOL)
Very early containment failure (VEF)	1. Containment over-pressurization (COP) 2. Hydrogen deflagration/detonation (H2) 3. Alpha-mode failure (ALPHA)
Early containment failure (EF)	1. Ex-vessel steam explosion (STEAM) 2. Failure of containment penetrations (PENE)
Late containment failure (LF)	1. Non-coolable ex-vessel debris causes basemat melt-through (BASE)
Very late containment failure (VLF)	1. All above containment failure modes combined with very late release time
Filtered venting (FV)	1. Very early venting (VEFV) 2. Early venting (EFV) 3. Late venting (LFV) 4. Very late venting (VLFV)

The recovery time depends on which components have failed. In the original model, power supply failure was assumed, and a recovery time distribution was specified for power supply [8]. The new model considers recovery times of different component types. However, since no repair time data was available, recovery probability distributions were assigned directly to different component types. Table 3 presents the mean recovery probabilities in different cases. The recovery probability distributions were lognormal and error factor 2 was used for each probability distribution. The probabilities vary depending on the pressure and time of the core melting. The probabilities were totally made up for this study except for power supply recovery failure probabilities which came from the previous studies [2, 8]. According to [8], there is less time for recovery in low pressure case. Therefore, smaller recovery probabilities were used in low pressure case. For very late melting, larger recovery probabilities were assumed than for normal low pressure case. Symbol '-' in the table means that no recovery probability was needed for the case, because the probability of the case was small or 0.

The recovery probability modelling was performed using CETL function BE_FV. BE_FV calculates Fussell-Vesely importance measure of a basic event, using the minimal cut sets of the PDS. The minimal cut sets of different PDSs were examined to identify which basic events or common cause failures caused the failure of the core cooling, and the basic events were categorised into the groups listed above. Only 100 most important minimal cut sets were examined in each case to find the most significant basic events. In the REC function (see Figures 6-7), BE_FV function is called for each basic event, and the probability of each group is calculated by summing the Fussell-Vesely values of the basic events belonging to the group. The recovery probability is calculated as a weighted sum of the probabilities presented in Table 3, where the weights are the probabilities calculated using BE_FV function.

In the case that depressurization is successful after high pressure melting, the emergency core cooling system recovery probability was assumed to be 0.99, even though the low pressure emergency core cooling system is not even used before core melting in that scenario.

Table 3: Mean probabilities of emergency core cooling system recovery depending on the failed components.

Components	High pressure	Low pressure	Very late melting
Cooling system components	0.2	0.05	0.1
Power supply	0.976	0.922	-
HVAC system	0.5	-	-
Demineralized water tank failure	0.1	-	-
Reactor protection system	0.999	0.99	0.995
Component cooling water system components	-	0.05	-
Service water system components	-	0.05	0.1
Condensation pool	-	-	0.05

The resulting mean recovery probabilities in different cases are presented in Table 4. The recovery fails most likely in the LOCA case, because pumps or valves of the emergency core cooling system are failed in a large portion of LOCA scenarios and their recovery in time was assumed unlikely. In other cases, power supply failures and reactor protection system failures dominate more and their repair in time is assumed likely.

Table 4: Mean probabilities for emergency core cooling system recovery for CET branches.

Case	Recovery probability
High pressure melting and depressurization	0.99
High pressure melting and no depressurization	0.828
Low pressure melting due to LOCA	0.352
Low pressure melting due to transient	0.922
Very late melting	0.938

4.5 Results

Table 5 presents main results calculated over all CETs including the frequencies and release fractions for all release categories. The four values in the cells of the table are mean, 5th percentile, median and 95th percentile. Weighted total release fractions are weighted by the frequencies of different release categories.

Table 5: Summary of results.

Bin	Freq.	S_Xe	S_Cs	S_Ru
OK	8.32E-07	7.76E-11	0.00E+00	0.00E+00
	1.02E-07	3.35E-11	0.00E+00	0.00E+00
	4.16E-07	8.41E-11	0.00E+00	0.00E+00
	2.74E-06	1.00E-10	0.00E+00	0.00E+00
ISOL	2.93E-08	8.49E-01	2.55E-01	8.82E-03
	2.19E-09	5.27E-01	1.02E-01	1.57E-04
	1.24E-08	9.15E-01	2.43E-01	5.56E-03
	1.03E-07	1.00E+00	4.37E-01	2.86E-02
VEF	5.40E-07	7.72E-01	1.19E-01	4.00E-03
	4.36E-08	3.01E-01	1.89E-02	4.47E-05
	2.38E-07	8.63E-01	9.79E-02	1.43E-03
	1.98E-06	1.00E+00	2.97E-01	1.61E-02
EF	8.48E-08	7.90E-01	1.55E-01	5.58E-03
	5.70E-09	3.60E-01	3.46E-02	1.04E-04
	3.31E-08	8.84E-01	1.38E-01	2.51E-03
	3.15E-07	1.00E+00	3.38E-01	2.10E-02
LF	5.99E-08	8.02E-01	1.56E-01	4.54E-03
	4.12E-09	3.87E-01	3.87E-02	3.18E-05
	2.31E-08	8.89E-01	1.40E-01	1.85E-03
	2.24E-07	1.00E+00	3.16E-01	1.85E-02
FV	1.99E-06	7.75E-01	9.84E-04	2.89E-05
	2.51E-07	3.24E-01	1.48E-05	1.60E-08
	1.02E-06	8.45E-01	1.27E-04	1.71E-06
	6.81E-06	1.00E+00	3.97E-03	9.24E-05
VLF	1.95E-07	7.72E-01	1.29E-01	4.31E-03
	1.14E-08	1.93E-01	1.75E-02	1.02E-06
	6.84E-08	1.00E+00	1.07E-01	1.20E-03
	6.93E-07	1.00E+00	3.28E-01	1.95E-02
Weighted Total	3.73E-06	6.05E-01	3.31E-02	1.10E-03
	5.14E-07	2.63E-01	8.58E-03	3.52E-05
	1.93E-06	6.50E-01	2.73E-02	5.47E-04
	1.22E-05	8.18E-01	7.73E-02	4.10E-03

FinPSA calculates also contributions of level 1 sequences to different level 2 results. For example, the most important event tree sequences contributing to total Cesium releases are listed in Table 6 and the sequences can be found in the event trees presented in Figures 2-5. It can be seen that most of the Cesium release risk comes from the three level 1 sequences with the largest frequencies. The contribution of sequence i is calculated with the following formula:

$$C^{Cs}(i) = \frac{\sum_{k=1}^n \sum_{j=1}^m F_{i,j}(k) f_j(k) Cs_j(k)}{\sum_{k=1}^n \sum_{j=1}^m f_j(k) Cs_j(k)},$$

where n is the number of simulation cycles, m is the number of level 2 sequences, $F_{i,j}(k)$ is the conditional probability of level 1 sequence i given level 2 sequence j in k :th simulation cycle, $f_j(k)$ is the frequency of level 2 sequence j in k :th simulation cycle, and $Cs_j(k)$ is the amount of Cesium releases in level 2 sequence j in k :th simulation cycle.

Table 6: The most important level 1 sequences contributing to total Cesium releases.

Nr.	Sequence	Contribution (%)
1	29	51.56
2	27	26.02
3	4	17.87
4	26	2.04
5	15	0.87

Table 7 presents the most important basic events and initiating events contributing to total Cesium releases. Loss of main feedwater and loss of offsite power are the dominating initiating events. The contribution of event E is calculated with the following formula:

$$C^{Cs}(E) = \sum_{i=1}^l FV_i(E) \cdot C^{Cs}(i),$$

where l is the number of level 1 sequences, $FV_i(E)$ is Fussell-Vesely of event E in sequence i , and $C^{Cs}(i)$ is the contribution of sequence i to the Cesium releases.

Table 7: The most important level 1 events contributing to total Cesium releases.

Nr.	Event	Contribution (%)
1	Loss of offsite power (IE)	51.90
2	Loss of main feedwater (IE)	46.24
3	Gas turbine failure to start	36.73
4	Diesel generators CCF (all DGs fail to operate)	28.83
5	Failure of manual depressurization	24.16
6	Filtered containment venting failure	18.03
7	Gas turbine under maintenance	16.92

4.6 Sensitivity analysis

4.6.1 Ex-vessel steam explosions

As discussed in Section 2, uncertainties related to ex-vessel steam explosions are high. The explosion triggering probabilities used in the model are likely conservative:

- mean triggering probability is 0.99 in high pressure case,
- mean triggering probability is 0.5 in low pressure case.

However, containment failure probabilities that are conditional on the occurrence of steam explosion impulse exceeding the strength of LDW walls might not be conservative. They are based on pressure impulse curves presented in Figure 1. In some studies [8-9], significantly larger pressure impulses have been calculated. To study the sensitivity of the results to steam explosions, alternative analysis is performed using higher conditional containment failure probabilities presented in Table 8 (see Table 1 for comparison).

Table 8: Alternative conditional probabilities of explosion impulse exceeding strength of LDW walls.

	Much melt ejected (case 1, late or no ECCS recovery)	Little melt ejected (case 2, early ECCS recovery)
RCS depressurized (case LP)	1.0	0.2
RCS not depressurized (case HP)	0.5	0.1

The change in conditional containment failure probabilities increased significantly the frequency of an early containment failure (release category EF). The mean frequency increased from $8.48E-8$ to $4.06E-7$. This new frequency forms 42.6% of the large early release frequency (which is the sum of the frequencies of release categories VEF, EF and ISOL). This indicates that ex-vessel steam explosions have potential to be a major contributor to early release risk.

4.6.2 Basemat melt-through

The mean probability for basemat melt-through given that the ex-vessel debris is not coolable is 0.1 in the model. In some other models [14], this probability is assumed to be 1. Therefore, to study to sensitivity of the results to this assumption, the probability is set to 1 for alternative analysis. By this change, the frequency of late containment failure becomes ten times higher. Then 36% of the large release frequency comes from basemat melt-through.

4.7 Basic event contributions

A drawback in the use of BE_FV function to estimate the ECCS recovery probability (see Section 4.4) is currently that the contributions of level 1 basic events to level 2 results are not calculated correctly. For example, the failure of the emergency core cooling system in the case of 'low pressure melting due to LOCA' is caused by RPS failures with probability 0.32 and by failures of pumps and valves with probability 0.68. However, the recovery of the emergency core cooling is assumed much more likely if RPS failure has caused the failure of the ECCS. Computation of basic event contributions does not take this into account. Therefore, contributions of pump and valve failures to radioactive releases should be larger than what is calculated. At its root, this problem is one of model parsimony: we could solve it by inserting a new layer to the event tree (see below), but to keep the tree more compact we want instead to handle RPS failures and other component failures in the same event tree sequence. It would not be a problem to separate these two types of failures in different event tree branches, but when there are more failure categories, like in the high pressure melting case, the CETs would become too large.

An alternative version of the model where RPS failures were separated to different accident sequence was created. Modified event tree for large LOCA is presented in Figure 9. Minimal cut sets with RPS failures go to sequence 2 and minimal cut sets with other component failures go to sequence 1.

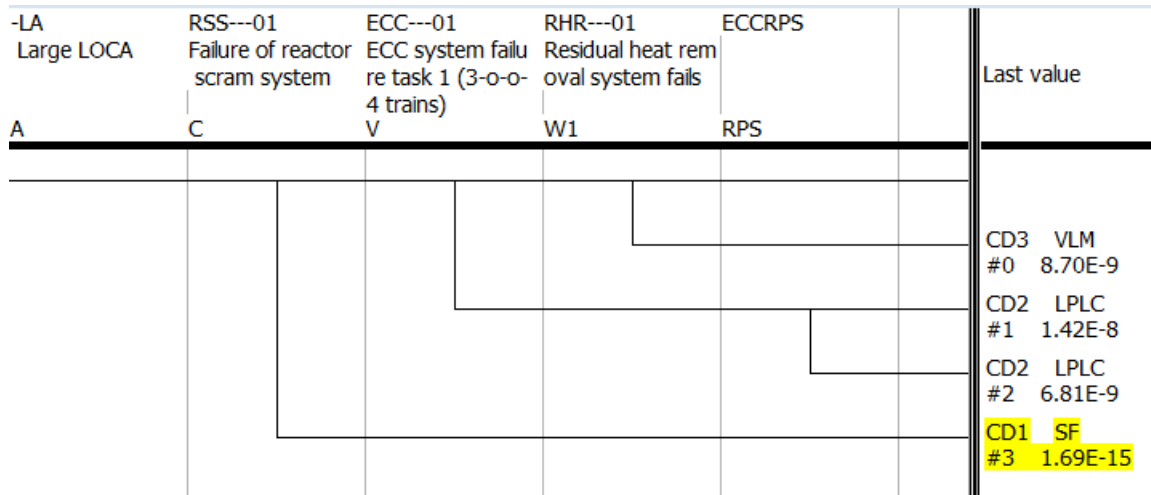


Figure 9: Modified event tree for large LOCA.

New section called RPSF was added to the CET for low pressure melting due to LOCA (Figure 10). In this section, it is asked whether the emergency core cooling system has failed due to RPS failure or other failures. Function SC_INCL [5] is used to calculate the probabilities of the branches in section RPSF (the function is called in branch functions COMF and RPSF). The probabilities are the portions (conditional probabilities) of event tree sequences 1 and 2. Due to SC_INCL function, only event tree sequence 1 is seen in the results of CET sequences 1-18, and only event tree sequence 2 is seen in the results of CET sequences 19-36. The emergency core cooling system recovery probability is also calculated as dependent on the result of RPSF section instead of using BE_FV function. When the modelling is performed this way, basic event contributions are calculated correctly.

Table 9 presents the most important basic events contributing to Cesium releases in the LOCA CET. Both contributions from the original model and contributions from the modified model are presented. The modified model gives the correct contribution values. It can be seen that the importance of software CCFs is overestimated significantly in the original model.

The modified model produced correct results because RPS failures were separated into different event tree sequence than other failures. Similar modelling style could also be applied to other PDSs. However, for example, for high pressure melting, four new event tree (or interface tree) sequences would be needed, because there are five different failure categories with different recovery probabilities. The CET would correspondingly grow four times larger so that it would include 181 sequences. The model would become very large.

It would be possible to fix the issue with BE_FV function by scaling the basic event contributions according to corresponding recovery probabilities. In the sequences where the ECC recovery is successful in the LOCA CET, RPS failure contributions would be scaled by

$$\frac{r_p}{p_p \cdot r_p + p_c \cdot r_c}$$

where r_p is recovery probability in case of RPS failure, p_p is the probability that ECCS failure was caused by RPS failure, p_c is the probability that ECCS failure was caused by other component failures and r_c is the recovery probability in case of other component failures. Respectively, in the sequences where the ECCS recovery fails, RPS failure contributions would be scaled by

$$\frac{1 - r_p}{p_p \cdot (1 - r_p) + p_c \cdot (1 - r_c)}$$

LPLC Low pressure LOCA	ISOL Containment leakage	RPSF RPS failed?	ECCS ECCS recovery	Flood LDW flooding	VEF Very early containment failure	VF Vessel failure	EF Early containment failure	LF Late containment failure	FV Filtered venting	
	ISOL_OK	COMF	REC	FL	NO_VEF	NO_VF	NO_EF	NO_LF	NO_FV	#1
									FV	#2
						VF	NO_EF	NO_LF	NO_FV	#3
									FV	#4
								LF		#5
							EF	NO_LF		#6
					VEF	NO_VF	NO_EF	NO_LF		#7
						VF	NO_EF	NO_LF		#8
			NO_REC	NO_FL	NO_VEF	VF	NO_EF	NO_LF	NO_FV	#9
									FV	#10
								LF		#11
							EF	NO_LF		#12
					VEF	VF	NO_EF	NO_LF		#13
				FL	NO_VEF	VF	NO_EF	NO_LF	NO_FV	#14
									FV	#15
								LF		#16
							EF	NO_LF		#17
					VEF	VF	NO_EF	NO_LF		#18
	RPSF	REC	FL	NO_VEF	NO_VF	NO_EF	NO_LF	NO_FV		#19
									FV	#20
						VF	NO_EF	NO_LF	NO_FV	#21
									FV	#22
								LF		#23
							EF	NO_LF		#24
					VEF	NO_VF	NO_EF	NO_LF		#25
						VF	NO_EF	NO_LF		#26
			NO_REC	NO_FL	NO_VEF	VF	NO_EF	NO_LF	NO_FV	#27
									FV	#28
								LF		#29
							EF	NO_LF		#30
					VEF	VF	NO_EF	NO_LF		#31
				FL	NO_VEF	VF	NO_EF	NO_LF	NO_FV	#32
									FV	#33
								LF		#34
							EF	NO_LF		#35
					VEF	VF	NO_EF	NO_LF		#36
NO_ISOL	NO_REC	NO_REC	NO_FFL	NO_VEF	VF					#37

Figure 10: Modified CET for low pressure melting due to LOCA.

Table 9: The most important basic events contributing to Cesium releases in the LOCA case.

Event	Contribution (%) in original model	Contribution (%) in modified model
ECCS pumps CCF (all pumps stop operating)	30.78	39.39
Software CCF: spurious actuation of ECC2 (same results for 5 other software CCF events)	4.75	1.97
ECCS pumps CCF (pumps A, B and C stop operating) (same results for 3 other similar CCF events)	3.60	4.61
ECCS pump A stops operating (same results for 3 other pumps)	3.16	4.05
ECCS train A under maintenance (same results for 3 other trains)	2.75	3.52
ECCS pumps CCF (all pumps fail to start)	2.44	3.12
ECCS valves CCF (all valves fail to open)	2.43	3.10
SWS pumps CCF (all pumps fail to start)	2.14	2.74
CCW pumps CCF (all pumps fail to start)	2.14	2.74
SWS pumps CCF (all pumps stop operating)	1.79	2.28

The contributions of other component failures would be scaled correspondingly. This type of scaling function could possibly be implemented in CETL.

When there are many basic events in the results, it is also not practical to call BE_FV function for all of them. In this study, only basic events appearing in the 100 most important minimal cut sets were considered, which excluded quite many basic events and caused small errors in the emergency core cooling system recovery probability calculation. Use of BE_FV function many times also increases computation times significantly. It would be more practical if BE_FV type of function could be called for a group of basic events instead of one at a time. For example, computation of Fussell-Vesely for a particular system could be useful in level 2.

5. Outline for two-phase uncertainty analysis

The level 2 modelling in the BWR model has been performed using ‘probabilities first’ approach, which means that the occurrence of each branch in a CET on a given simulation round is determined based on a probability parameter (or multiple probability parameters). The benefit of this approach is that it enables proper uncertainty analysis resulting in nice uncertainty curves that are easy to interpret. In the model, values for physical parameters used in source term calculations are determined based on the accident sequence. One could however argue that this modelling approach does not take very well into account the dynamic nature of severe accidents and does not fully utilise the capabilities of dynamic CETs of FinPSA.

An alternative modelling approach is ‘physical parameters first’ approach in which values for physical parameters are determined first (e.g. from uncertainty distribution) and the CET branch probabilities are determined based on the physical parameters, like in [8]. A drawback of that approach is that it is difficult to calculate proper uncertainty distributions for release frequencies, i.e. the resulting distributions can be difficult to interpret or they might not be sensible at all [20]. On the other hand, the ‘physical parameters first’ approach gives better possibilities to model how accident scenarios vary depending on physical parameter values and to model dynamic dependencies related to severe accident phenomena. For better use of the ‘physical parameters first’ approach, it might be necessary to develop the FinPSA dynamic containment event tree modelling tool to take into account different types of uncertainties.

Uncertainties can be divided into aleatoric and epistemic uncertainties [21-23]. Aleatoric uncertainty is the uncertainty that is known, e.g. it is known that the toss of a coin can result in heads or tails based on a chance. In a level 2 model, branches and accident sequences of a CET represent possible realisations of aleatoric uncertainties, i.e. it is known that one sequence occurs given the PDS, but it is a matter of luck which one it is. The realisation of a specific value of a physical parameter, such as core meltdown fraction, is also subject to aleatoric uncertainty. Epistemic uncertainty is the uncertainty related to the knowledge about a phenomenon. For example, the probability of successful depressurisation is not known exactly; there is epistemic uncertainty about it. Other epistemic uncertainties appearing in level 2 are related to the probability distributions of physical parameters, such as core meltdown fraction; the mean values, levels of deviation and shapes of distributions are not known exactly, there can be significant uncertainties about them.

When aleatoric and epistemic uncertainties are handled in the same way, the resulting uncertainty distributions are difficult to interpret. For example, the frequency of an accident sequence is not subject to aleatoric uncertainty. Instead the occurrence of the accident sequence is subject to aleatoric uncertainty according to the frequency. If realisations of aleatoric uncertainties are used in the calculation the frequency on a simulation cycle, the resulting uncertainty distribution of the frequency is incorrect. The uncertainty distribution of the frequency should reflect only epistemic uncertainties of model parameters.

One solution to improve the handling of uncertainties would be to perform the uncertainty analysis in two phases [21, 22], as outlined in Figure 11. In this method, there would be N simulation cycle blocks containing M simulation cycles. For the simulation results of one simulation cycle block, statistical analysis would be performed to calculate average frequency and average release fractions for each accident sequence (along with some other results). Then, statistical analyses would be performed over the simulation cycle blocks based on their average results to produce uncertainty distributions for release frequencies, source variables and other collected variables. These distributions would show the effects of epistemic uncertainties only. Statistical analysis could also be performed over both simulation loops to calculate uncertainty distributions that would show the combined effects of both epistemic and aleatoric uncertainties. However, these distributions should not be calculated for frequencies.

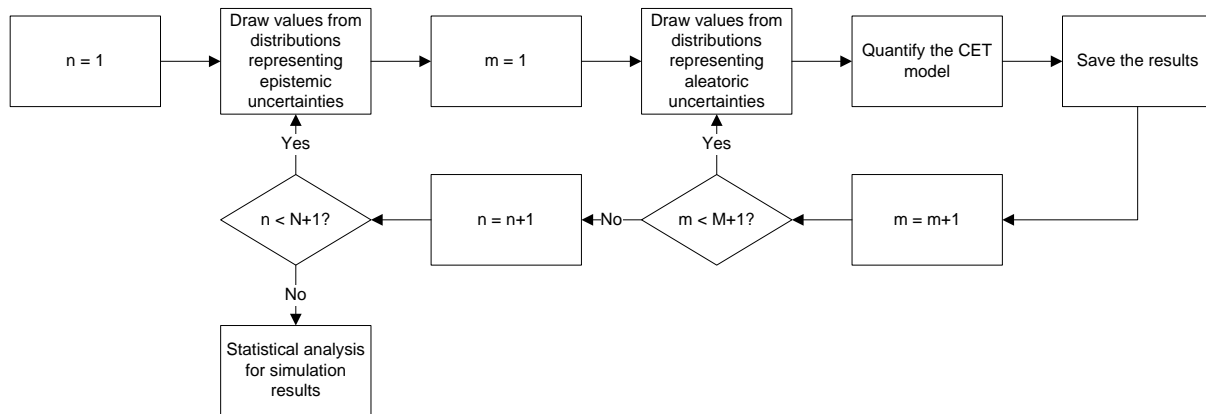


Figure 11: An outline for the progression of two-phase uncertainty analysis.

The two-phase uncertainty analysis would result in uncertainty distributions that would reflect only epistemic uncertainties related to the input parameters. Aleatoric uncertainties would be completely evaluated inside simulation cycle blocks and the results of one simulation block would be based on full range of possible occurrences of events and physical parameter values given specific values from distributions representing epistemic uncertainties.

The two-phase uncertainty analysis would be computationally more demanding than normal one-phase uncertainty analysis. The analysis would contain NM simulation cycles in total. The number of simulation cycles inside one block (M) should be sufficiently large so that results could be produced for each accident sequence. Suitable number of simulations would depend significantly on the model. If the model would contain some rare event sequences that would occur e.g. once in 1000 simulation cycles, then the number of simulations inside one block should be of that magnitude. The needed number of simulations can be affected by modelling decisions. Some special treatment for rare event sequences could be considered. The number of simulation cycle blocks should also be sufficiently large so that proper uncertainty distributions could be produced (at least hundreds). Some approximate methods have been developed to reduce the required number of simulation cycles [22, 23]. Their applicability to FinPSA level 2 could be studied.

In current models, such as the BWR model, no division to epistemic and aleatoric uncertainties has been made. For example, there is only one uncertainty distribution for core meltdown fraction in specific scenario. This uncertainty distribution covers both epistemic and aleatoric uncertainties. To make the analysis more correct, there should be separate uncertainty distributions for the mean core meltdown fraction and deviation parameter that would represent epistemic uncertainty on the core meltdown fraction. The separation of the uncertainties would make the modelling more complicated and challenging. In some cases, simplifications could be sufficient, such as treating all the uncertainty of a variable as epistemic, but only for variables that do not affect significantly the probabilities of CET branches.

6. Conclusions

This report has continued the development of simplified BWR plant PRA models. Previously developed level 1 and level 2 models were integrated and extended. The new model contains four level 1 event trees and five level 2 CETs. Uncertainty data was added to level 1, but otherwise the focus was on the extension of the level 2 part. Levels 1 and 2 were integrated so that it was possible to list most important event tree sequences, initiating events and basic events with regard to radioactive releases. The example model can later be utilised in further studies, demonstrations, training and FinPSA testing.

The computation of emergency core cooling system recovery probability based on level 1 results was studied. CETL function BE_FV (calculation of the Fussell-Vesely importance measure from minimal cut sets) was used for that. The resulting recovery probabilities varied significantly between PDSs. The probability parameters were however completely made up for this study, which means that the results might not be realistic. The purpose was just to demonstrate the modelling approach using BE_FV function. Some possibilities for the improvement of FinPSA level 2 were also identified. Contributions of level 1 basic events to level 2 results were not calculated correctly when BE_FV function was used. This problem could be solved by a suitable basic event contribution scaling function.

Ex-vessel steam explosions were also discussed in the report. Probabilistic modelling of steam explosions is very challenging because uncertainties related to the phenomenon, especially triggering of explosions, are very high. Pressure impulses of explosions can be calculated quite well using deterministic software tools, but the probability that an explosion occurs in the first place cannot be properly estimated based on current knowledge. Currently, it is a good idea to use conservative probabilities in PRA. It could be studied if explosion triggering probabilities could be estimated based on some physical parameters calculated by deterministic software tools, but plenty of development work and analyses are needed before well-justified probabilities can be estimated.

Sensitivity analysis results indicate that ex-vessel steam explosions have potential to be a major risk contributor. Therefore, more research activities should be dedicated to them. The same applies to basemat melt-through.

To handle separately different types of uncertainties in dynamic containment event trees, a method with two-phase uncertainty analysis was outlined. The method would enable explicit modelling of dynamic dependencies and production of proper uncertainty distributions as a result at the same time, whereas with normal one-phase uncertainty analysis it is difficult to do both. The study could be continued by developing software implementation of the two-phase uncertainty analysis and improving the modelling of dynamic dependencies related to physical parameters in the BWR model.

References

- [1] International Atomic Energy Agency, IAEA. Development and application of level 2 probabilistic safety assessment for nuclear power plants: Specific safety guide No: SSG-4. Vienna, 2010.
- [2] Tyrväinen, T, Karanta, I. Level 2 studies – Source term characteristics and hydrogen explosions. VTT Technical Research Centre of Finland Ltd, Espoo, 2017. VTT-R-00354-17.
- [3] Authén, S, Holmberg, J-E, Tyrväinen, T, Zamani, L. Guidelines for reliability analysis of digital systems in PSA context – Final Report, NKS-330. Nordic nuclear safety research (NKS), Roskilde, 2015.
- [4] Tyrväinen, T, Silvonen, T, Mätäsniemi, T. Computing source terms with dynamic containment event trees. 13th International conference on probabilistic safety assessment and management (PSAM13), Seoul, Korea, 2-7 October, 2016.
- [5] Tyrväinen, T. FinPSA - User guide - Tight integration of PRA levels 1 and 2, VTT Technical Research Centre of Finland Ltd, Espoo, 2016. VTT-R-03893-16.

- [6] OECD Nuclear Energy Agency. SERENA Phase 1, Task 1 final report of research programme on fuel-coolant interaction, NEA/CSNI/R(2004)7. Paris, 2004.
- [7] ASAMPSA 2. Best-practices guidelines for L2PSA development and applications, Volume 2, Technical report ASAMPSA2/WP2-3/D3.3/2013-35. 2013.
- [8] Silvonon, T. Steam explosion case study using IDPSA methodology. VTT Technical Research Centre of Finland, Espoo, 2013. VTT-R-05974-13.
- [9] Silvonon, T. MC3D simulations of ex-vessel steam explosions in IDPSA framework. VTT Technical Research Centre of Finland, Espoo, 2014. VTT-R-02944-14.
- [10] Strandberg, M. Ex-vessel steam explosion analysis with MC3D [Master's thesis]. Aalto University, Espoo, 2016.
- [11] OECD Nuclear Energy Agency. Steam Explosion Resolution for Nuclear Applications – SERENA, Final Report, NEA/CSNI/R(2007)11. Paris, 2007.
- [12] Moriyama, K, Park, HS. Probability distribution of ex-vessel steam explosion loads considering influences of water level and trigger timing. Nuclear Engineering and Design, 293, 292-303, 2015.
- [13] Grishchenko, D, Basso, S, Kudinov, P. Development of a surrogate model for analysis of ex-vessel steam explosion in Nordic type BWRs. Nuclear Engineering and Design, 310, 311-327, 2016.
- [14] Kudinov, P, Galushin, S, Grishchenko, D, Yakush, S, Adolfsson, Y, Ranlöf, L, Bäckström, O, Enerholm, A. Scenarios and phenomena affecting risk of containment failure and release characteristics. Nordic nuclear safety research, Roskilde, 2017. NKS-395.
- [15] Nowak, AS, Collins, KR. Reliability of structures. McGraw-Hill, 2000.
- [16] Ditlevsen, O, Madsen, HO. Structural reliability methods. Internet edition (original: John Wiley & Sons, 1996), June-September 2007. [http://chodor-projekt.net/wp-content/uploads/BiNSK/Literatura/Dilevsen,Madsen,%20Structural%20Reliability%20Methods%20\(2007\).pdf](http://chodor-projekt.net/wp-content/uploads/BiNSK/Literatura/Dilevsen,Madsen,%20Structural%20Reliability%20Methods%20(2007).pdf) (link accessed 22.12.2017)
- [17] Jones, N. Structural impact, second edition. Cambridge University Press, 2012.
- [18] VTT Technical Research Centre of Finland Ltd. FinPSA – Tool for promoting safety and reliability. 2018. <https://www.simulationstore.com/finpsa> (link accessed 8.1.2018)
- [19] Okkonen, T. Development of a parametric containment event tree model for a severe BWR accident. Finish centre for radiation and nuclear safety, Helsinki, 1995. STUK-YTO-TR81.
- [20] Tyrväinen, T, Silvonon, T. Summary on integrated deterministic and probabilistic safety assessment development and case studies. VTT Technical Research Centre of Finland, Espoo, 2015. VTT-R-04473-15.

- [21] Jyrkama, MI, Pandey, MD. On the separation of aleatory and epistemic uncertainties in probabilistic assessments. *Nuclear Engineering and Design*, 303, 68-74, 2016.
- [22] Karanki, DR, Rahman, S, Dang, VN, Zerkak, O. Epistemic and aleatory uncertainties in integrated deterministic and probabilistic safety assessment: Tradeoff between accuracy and accident simulations. *Reliability Engineering and System Safety*, 162, 91-102, 2017.
- [23] Hofer, E, Kloos, M, Krzykacz-Hausmann, B, Peschke, J, Woltereck, M. An approximate epistemic uncertainty analysis approach in the presence of epistemic and aleatory uncertainties. *Reliability Engineering and System Safety*, 77, 229-238, 2002.

Title	Phenomena Threatening Containment Integrity in Deterministic and Probabilistic analyses and integration of PRA levels 1 and 2
Author(s)	Anna Nieminen ¹ (ed.), Veikko Taivassalo ¹ , Magnus Strandberg ¹ , Tero Tyrväinen ¹ , Ilkka Karanta ¹
Affiliation(s)	¹ VTT Technical Research Centre of Finland Ltd
ISBN	978-87-7893-500-7
Date	October 2018
Project	NKS-R / SPARC
No. of pages	8 + 106
No. of tables	0
No. of illustrations	3
No. of references	5
Abstract max. 2000 characters	<p>Phenomena threatening the BWR containment integrity were assessed both deterministically and probabilistically. Studies related to establishing a temperature-based dryout criteria for a debris bed were continued evaluating the influence of friction models. Agreement between the VTT and KTH results was improved after implementing the same friction model as in DECOSIM into Fluent. Deterministic steam explosion analysis was performed to study the effect of RPV breaking location on dynamic pressure load on lower drywell wall. The resulting explosions were stronger in comparison to the previous central break cases.</p> <p>Probabilistic modelling of steam explosions is very challenging because uncertainties related to the phenomenon, especially triggering of explosions, are very high. Currently, it is a good idea to use conservative probabilities in PRA. It could be studied if explosion triggering probabilities could be estimated based on some physical parameters calculated by deterministic software tools, but plenty of development work and analyses are needed before well-justified probabilities can be estimated.</p> <p>The development of simplified PRA models of a BWR plant was also continued by extending previously developed level 1 and level 2 models were extended and integrated so that it is possible to list most important event tree sequences, initiating events and basic events with regard to radioactive releases.</p>
Key words	Debris bed coolability, Fluent, steam explosions, MC3D, PRA